A Method of Designing Circularly Symmetric Shaped Dual Reflector Antenna Using UTD/PO Analysis and Differential Evolution Algorithm

by

Mohammad Asif Zaman

MASTER OF SCIENCE IN ELECTRICAL AND ELECTRONIC ENGINEERING

Department of Electrical and Electronic Engineering
BANGLADESH UNIVERSITY OF ENGINEERING AND TECHNOLOGY
September 2011

The thesis titled **“A Method of Designing Circularly Symmetric Shaped Dual Reflector Antenna Using UTD/PO Analysis and Differential Evolution Algorithm”** submitted by Mohammad Asif Zaman, Student No.: 1009062069, Session: October, 2009, has been accepted as satisfactory in partial fulfillment of the requirement for the degree of MASTER OF SCIENCE IN ELECTRICAL AND ELECTRONIC ENGINEERING on September 24, 2011.

BOARD OF EXAMINERS

1. ____

Dr. Md. Abdul Matin
Professor
Department of Electrical and Electronic Engineering,
Bangladesh University of Engineering and Technology,
Dhaka – 1000, Bangladesh.

Chairman
(Supervisor)

2. ____

Dr. Md. Saifur Rahman
Professor and Head
Department of Electrical and Electronic Engineering,
Bangladesh University of Engineering and Technology,
Dhaka – 1000, Bangladesh.

Member
(Ex-officio)

3. ____

Dr. Pran Kanai Saha
Professor
Department of Electrical and Electronic Engineering,
Bangladesh University of Engineering and Technology,
Dhaka – 1000, Bangladesh.

Member

4. ____

Dr. A B M Siddique Hossain
Professor and Dean
Faculty of Engineering,
American International University-Bangladesh,
Dhaka, Bangladesh.

Member
(External)

CANDIDATE'S DECLARATION

It is hereby declared that this thesis or any part of it has not been submitted elsewhere for the award of any degree or diploma and that all sources are acknowledged.

Signature of the Candidate

Mohammad Asif Zaman

Dedication

To my parents.

Acknowledgement

First of all, I would like to thank Allah for giving me the ability to complete this thesis work.

I would like to express my sincere gratitude to my supervisor, Dr. Md. Abdul Matin. This thesis would not have been completed without his support and guidance. His constant encouragement gave me the confidence to carry out my work.

I would like to thank all my teachers. They gave the knowledge and directions that have helped me throughout my life. I express my gratitude to my teachers from Bangladesh University of Engineering and Technology. The knowledge I learned from the classes in my B.Sc. and M.Sc. levels were essential for this thesis.

I would like to specially thank my first physics teacher, Suresh Chandra Majumder. I learned many of the fundamental concepts of science and engineering from him. His insightful lectures made me interested in science and technology.

I want to thank my friends for providing my support and encouragement. Their suggestions helped me in countless ways.

Last but not the least, I would like to thank by parents and my family. Their unconditional support made it possible for me to finish this thesis.

ABSTRACT

A method of designing circularly symmetric shaped dual reflector antennas is presented in this thesis. The method is used to design shaped Cassegrain and shaped Gregorian reflector antennas. The two step design procedure includes a proposed method to define shaped dual reflector surfaces, and an optimization algorithm that determines the optimum shaped surfaces. The proposed method successfully describes practical shaped reflector surface using a small number of parameters compared to other commonly used methods found in literature. The reduction of design parameters reduces computational complexities. Differential evolution optimization algorithm is used to optimize the parameters that define the shaped geometry. Two separate sets of optimizations have been performed for each of the dual reflector geometries (Cassegrain and Gregorian). The first optimization concentrates on reducing beamwidth by creating uniform illumination of the main reflector while keeping main reflector size constant and spillover losses to a minimum. The second optimization concentrates on maintaining a small beamwidth by creating a uniform illumination over a smaller main reflector while keeping spillover losses to a minimum. The design requirements are incorporated into the definition of the cost function of the optimization algorithm.

As the optimization requires evaluation of the radiation characteristics of the shaped dual reflectors, field analysis is inherent in the design procedure. Field characteristics of the feed, the subreflector, and the main reflector are formulated. A corrugated horn antenna is designed as the feed antenna and its field characteristics are evaluated using standard equations. Uniform theory of diffraction is used for analysis of the field scattered from the subreflector on to the main reflector. The field radiated from the main reflector is calculated using physical optics method. The beamwidth is computed for the shaped and unshaped dual reflectors from corresponding far-field patterns. It is found that the shaped reflectors outperform the unshaped reflectors in terms of beamwidth. Other performance characteristics of the designed shaped dual reflectors are also found to be within satisfactory limits. The obtained values are found to be in good agreement with numerical and experimental values reported in literature.

CONTENTS

LIST OF TABLES

LIST OF FIGURES

LIST OF ABBREVIATIONS

AF	:	Aperture Field
DE	:	Differential Evolution
ECM	:	Equivalent Current Method
GO	:	Geometrical Optics
GTD	:	Geometrical Theory of Diffraction
HPBW	:	Half Power Beamwidth
ISB	:	Incident Shadow Boundary
PO	:	Physical Optics
PTD	:	Physical Theory of Diffraction
RSB	:	Reflection Shadow Boundary
UTD	:	Uniform Theory of Diffraction

LIST OF SYMBOLS

f_p : Focal distance of the primary/main reflector

d_p : Diameter of the primary reflector

e : Eccentricity of the subreflector

d_s : Diameter of the subreflector

Δ_p : Depth of the primary reflector

l_p : Distance of the feed from main reflector vertex

f : Frequency

k : Free space wave number

E_{cp} : Co-polarized field component of the feed antenna

E_{xp} : Cross polarized field component of the feed antenna

τ_n : n^{th} amplitude distortion parameter

ζ_n : n^{th} exponent distortion parameter

$\delta(.)$: Distortion function

(ρ_s, ϕ_s) : Polar coordinates of a subreflector point projected on the *xy* plane

(ρ_m, ϕ_m) : Polar coordinates of a main reflector point projected on the *xy* plane

$\mathbf{E_i}$: Incident electric field on the subreflector surface

$\mathbf{E_d}$: Diffracted electric field from the subreflector

$\mathbf{E_r}$: Reflected electric field from the subreflector

$\mathbf{E_s}$: Total scattered electric field from the subreflector

$\mathbf{H_{inc}}$: Magnetic field incident on the main reflector surface

$\mathbf{J_{PO}}$: PO surface current density on the main reflector surface

$\mathbf{A}$: Vector magnetic potential

$\mathbf{E_{rad}}$: Radiated electric field from the main reflector

$\hat{\mathbf{n}}_\mathbf{s}$: Unit normal vector on the subreflector surface

$\hat{\mathbf{n}}_\mathbf{m}$: Unit normal vector on the main reflector surface

$\hat{\mathbf{s}}_\mathbf{i}$: Unit vector denoting the direction of incident ray

$\hat{\mathbf{s}}_\mathbf{r}$: Unit vector denoting the direction of reflected ray

$\hat{\mathbf{s}}_\mathbf{d}$: Unit vector denoting the direction of diffracted ray

D_s : Soft diffraction coefficient

D_h : Hard diffraction coefficient

a_e : Radius of curvature of the subreflector surface

N_p : Population size used by the DE algorithm

$G_{\max}$: Maximum generation size set for the DE algorithm

F_m : Mutation scale factor of the DE algorithm

C_r : Crossover constant of the DE algorithm

$f_{\cos t}$: Cost function of the DE algorithm

D_o : Maximum directivity of the dual reflector antenna

η_{ill} : Main reflector illumination efficiency

η_{block} : Blockage efficiency

$\eta_{splill,f}$: Spillover efficiency of the feed

$\eta_{splill,s}$: Spillover efficiency of the subreflector

T_p : Field taper at the edge of the main reflector

T_s : Field taper at the edge of the subreflector

χ : Elevation angle measured from main reflector axis (–z axis)

CHAPTER 1
INTRODUCTION

1.1 Reflector Antennas

Antennas are key components of wireless communication systems. An antenna transforms an electrical signal to electromagnetic waves that propagate through space and can be received by another antenna [1]. For point to point communication, the radiated power of the antenna must be concentrated within a narrow angular region. Reflector antennas are suitable for such applications [2].

Reflector antennas are widely used in radars, radio astronomy, satellite communication and tracking, remote sensing, deep space communication, microwave and millimeter wave communications etc. [1], [3]. The rapid developments in these fields have created demands for development of sophisticate reflector antenna configurations. There is also a corresponding demand for analytical, numerical and experimental methods of design and analysis techniques of such antennas.

The configuration of the reflectors depends heavily on the application. The dual reflector antennas are preferred in many applications because they allow convenient positioning of the feed antenna near the vertex of the main reflector and positioning of other bulky equipments behind the main reflector [3]. Also the feed waveguide length is reduced [4]. They also have some significant electromagnetic advantage over single reflector systems [5]. Although many dual reflector configurations exist, the circularly symmetric dual reflector antennas remain one of the most popular choices for numerous applications [1].

The most common circularly symmetric dual reflector antennas are the Cassegrain antenna and the Gregorian antenna. The Cassegrain antenna composes of a hyperboloidal subreflector and a paraboloidal main reflector. The Gregorian antenna composes of an ellipsoidal subreflector and a paraboloidal main reflector. In both cases, a feed antenna (usually a horn antenna) illuminates the subreflector which in turn illuminates the main reflector. The main reflector produces the radiated electric field that propagates into space. The radiation performance of the dual reflector antennas depend on the radiation characteristics of the feed and the geometrical shapes of the main reflector and the subreflector. Modern wireless communication and RADAR applications enforce stringent requirements on the far-field characteristics of the antenna. For example, satellite communications imposes limitations on maximum beamwidth and maximum sidelobe levels of the antenna to avoid interference with adjacent satellites [2]. The traditional Cassegrain and Gregorian geometry have fixed geometries and offer limited flexibilities to antenna designers. As a result, the maximum performance that can be extracted from these antennas is limited by geometrical constraints.

1.2 Reflector Shaping

For high performance applications, the traditional hyperboloid/paraboloidal or ellipsoidal/paraboloidal geometry must be changed. *Reflector shaping* is the method of changing the shape of the reflecting surfaces to improve the performance of the antenna. Shaped reflector antennas outperform conventional unshaped reflector antennas. Reflector shaping allows the designers additional flexibility. The antenna designers have independent control over relative position of the reflectors, diameter of the reflectors and the curvature of the reflectors when shaped reflectors are used instead of conventional reflectors. This makes reflector shaping an essential tool for designing high performance reflector antennas.

1.3 Literature Review

Many methods of designing shaped reflectors are present in literature. One of the first major articles related to reflector shaping was published by Galindo in 1964 [6]. Galindo’s method required solution of multiple non-linear differential equations. Recent work has concentrated on approximating parts the reflector surfaces as conventional conic surfaces [7], [8]. These methods simplify the design procedure. Such methods are used to design shaped reflectors for many applications where high performance is required [1], [9]. The surface expansion based methods for designing shaped reflectors is one of the most popular design methods [10]. Rahmat-Samii has published multiple research papers on this area [8], [10]. A more detailed literature review on the design and analysis methods of shaped reflectors is given in Chapter 2.

The existing design methods give satisfactory performance for most cases. However, each method has its own limitations. The limitations are highlighted in Chapter 2. Moreover, most of the methods are computationally demanding. Creating a fast, accurate design method of shaped dual reflector antennas that is not computationally demanding, remains a challenging problem for antenna engineers.

1.4 Objectives of the Thesis

The thesis work concentrates on the design methods of circularly symmetric shaped dual reflector antennas. Design methods for both shaped Cassegrain and shaped Gregorian geometries are covered here. The work consists of derivation of analytical expressions and numerical simulations. The numerical simulations are performed using computer coding. The obtained results are verified by comparing the results with numerical and experimental results found in literature.

The objectives of the thesis are:

i. To propose a method of defining shaped reflector surfaces. The proposed method defines the shaped subreflector surfaces as distorted forms of conventional hyperboloidal/ellipsoidal subreflector surfaces. The distortion is controlled by small number of parameters. So, only a few parameters define the shaped subreflector surface. For verification, the method is used to define surfaces that represent practical shaped subreflector. The corresponding shaped main reflector surface is synthesized from the subreflector surface using geometrical optics (GO) method.

ii. To find optimum shaped dual reflector surfaces that satisfy predetermined design goals. The optimization process involves finding the optimum value of the parameters that define the shaped surfaces. The optimization is performed using differential evolution (DE) algorithm. The optimization procedure requires formulation of the fields on the subreflector and main reflector surfaces. The corrugated horn feed antenna is designed and its radiated field is calculated using standard equations. The fields scattered from the subreflector is computed using uniform theory of diffraction (UTD). The field radiated from the main reflector is evaluated using physical optics (PO).

iii. To evaluate the performance of the designed antennas. Performance parameters are calculated to quantify the performance of the designed antennas. They results are compared with performance of conventional unshaped antennas.

1.5 Organization of the Thesis

The thesis consists of eight chapters. The chapters cover the design procedure and numeric results.

Chapter 1 contains introductory discussion on the reflector antennas and reflector shaping. The objectives and outlining of the thesis are presented here.

Chapter 2 gives a brief literature review of existing methods of designing dual reflector antennas. The proposed design method is also discussed here.

Chapter 3 contains comprehensive description of defining the shaped geometries using the proposed design method. The co-ordinate system, and differential geometry based description of the reflectors are provided in this chapter.

Chapter 4 contains the design and characterization of the feed antenna.

Chapter 5 presents the UTD analyses of the fields scattered by the subreflectors.

Chapter 6 includes a brief introduction of differential evolution optimization algorithm. The algorithm is used to optimize the shape of the reflectors. Two different sets of optimizations are performed with different design goals to design two sets of shaped dual reflectors.

Chapter 7 presents the formulation of the radiated field from the main reflector using PO method. The PO surface currents are defined and evaluated. The PO radiation integral is defined in this chapter.

Chapter 8 contains the numerical results and discussion. The far-field radiation patterns of the designed antennas are calculated. The Performance parameters are defined and calculated. Comparisons of the far-field performance of the unshaped and shaped dual reflector antennas are presented in this chapter.

Chapter 9 is the concluding chapter. It contains the summary of the work. The chapter also highlights scopes for future work.

CHAPTER 2

EXISTING METHODS AND PROPOSED METHODS OF DESIGN AND ANALYSIS OF SHAPED REFLECTORS

2.1 Introduction

Reflector surface shaping is an essential part of designing high performance reflector antennas. Efficient designing of such shaped reflector surfaces have been a popular field of research work for antenna engineers. The design procedure depends heavily on the method of defining the shaped surfaces. The shapes of the surfaces depend on the pre-determined requirements imposed on the radiated field. These requirements depend on the applications of the antenna. A design method takes these requirements as input parameters and produces the shaped surface that satisfies these requirements.

To evaluate the performance of a designed antenna, the radiation characteristics of the antenna must be analyzed. Accurate evaluation of the radiated field characteristics of the antenna is necessary before practical implementation can be done. Exact solutions of field values are almost never possible due to the complex geometry of the reflector surfaces. However, many numerical methods exist for such calculations. Each method has its own advantages and disadvantages.

This chapter starts with brief descriptions of design methods of shaped reflector antennas. A short description of the proposed design method is presented next. After that, commonly used numerical methods of field analysis of reflector antennas are discussed. The chapter concludes with a brief description of the analysis method that will be used in this thesis.

2.2 Existing Methods of Designing Shaped Reflectors

There are several well known general methods of designing shaped reflectors. Most of these methods are applicable to both single reflector antennas and dual reflector antennas. They also apply to axially symmetric reflectors and offset configuration reflectors. In most cases, the general methods are simplified for specific geometric configurations. For example, the geometry of circularly symmetric dual reflector antennas allows some simplifications of calculations due to symmetry. So, specialized methods have been developed efficient designing of circularly symmetric dual reflectors. Some of the widely used methods of shaped reflector design are described next, paying special attention to circularly symmetric shaped reflectors.

2.2.1 Differential equation based design methods

One of the first design methods that was capable of synthesizing shaped reflectors for an arbitrary phase and amplitude distribution over the aperture plane was proposed by Galindo in 1964 [6]. The method is based on geometrical optics (GO). For an arbitrary feed pattern and a required arbitrary aperture distribution, the method formulates a pair of non-linear ordinary differential equations. The solutions of these equations give the co-ordinate of the points on the reflector surfaces. The method has been successfully used to design shaped reflectors [11].

The solutions of the non-linear differential equations are often computationally demanding. A computationally less demanding simplified method was presented by Lee in 1988 [12]. This method is very similar to Galindo’s method [6]. The difference is that, Lee divided the reflector surfaces into small sections and assumed the sections to be locally planar. This assumption converted the differential equations to algebraic equations, which are much easier to solve.

Other variations of the differential equation based design procedure can be found in literature. Although the method gives satisfactory results in many cases, it suffers from some limitations. As the method is GO based, and GO algorithm is characterized by discrete set of points, it may render a surface that has discontinuities and irregular boundary [10]. Also, the GO method gives errors for small sized reflectors. The solutions of the differential equations require complex computations. Lee’s method [12] introduces errors unless a large number of sections are selected. The overall computational complexity is not significantly reduced in that case. For these reasons, this method is not commonly used any more.

2.2.2 Surface expansion based design methods

In surface expansion based methods, the reflector surfaces are represented by an expansion set of orthogonal basis functions [13]. The expansion coefficients determine the shape of the surface. A small number of terms of the expansion set are sufficient to accurately describe a shaped surface. So, only a few expansion coefficients must be determined to define the surface. The differential equation based methods determines the co-ordinates of the points on the reflector surfaces, where as, the surface expansion based method only determines the expansion coefficients. Due to the decrease in number of unknowns, the surface expansion method is computationally less demanding. The surface expansion method can be incorporated with geometrical theory of diffraction (GTD) or its uniform version: uniform theory of diffraction (UTD) to produce an accurate design algorithm [10]. These design procedures are known as diffraction synthesis [10], [13].

Diffraction synthesis can be implemented using variety of expansion functions. One of the most popular is the Fourier-Jacobi expansion function [13], [14]. It has been widely used for reflector antenna design for various applications [9].

This method is more efficient than the differential equation based approach. One of the advantages of this method is that different optimization algorithms can easily be incorporated in it [9]. The numerical analysis methods like physical optics (PO) can also be evaluated efficiently when the surface is expanded by orthogonal functions [14]. However, the method has some limitations. For large number of expansion coefficients, the optimization process is slow to converge. If the method is used with PO, the computational time can be very high due to the radiation integral which must be evaluated many times for a single iteration. Despite these drawbacks, the method is very popular and successful in most cases.

2.2.3 Local surface approximation methods

Recently, a few new efficient methods for designing circularly symmetric shaped dual reflector design have been developed. One of the first significant works on this method was reported by Kim and Lee in 2009 [7]. This method divides the shaped reflector surfaces into electrically small sections. Each section is assumed to be a conventional unshaped dual reflector system. Since well established methods for analyzing conventional dual reflector system exist, the radiation characteristics of each section can easily be evaluated. The shaped surface is defined by combining all the local conventional surfaces. The method is GO based and requires solutions of several non-linear algebraic equations. So, it is computationally convenient.

Another method based on the same principle was proposed by Moreira and Bergmann in 2011 [8]. This method also divides the shaped surface into small local sections. The local sections are represented by unshaped conics. Each conic section is optimized to produce a desired aperture distribution, which is formulated by GO method.

As these methods have recently appeared in literature, most of the advantages and drawbacks of the method have not been investigated. Reduction in computational complexity is an obvious advantage. However, as the local sections are formulated independently, when the entire surface is formed by concatenating these sections, it may result in an irregular or discontinuous surface.

2.3 Proposed Design Method

The method proposed in this work, is applicable for only circularly symmetric reflectors. The design procedure for dual reflector antennas are presented in this thesis, but the method can easily be used for single reflector antennas.

In this method, the shaped surfaces are assumed to be distorted forms of unshaped surfaces. As most shaped reflectors resemble their unshaped counterparts [8], [11], the assumption is logical. So, it is expected that the shaped surfaces can be represented by modified versions of the equations that represent the conventional unshaped surfaces.

An unshaped reflector surface which is circularly symmetric around the z axis can be represented by the equation:

$$z = f_{surf}(x, y) \ . \tag{2.1}$$

Here, $f_{surf}(.)$ is a function that depends on the surface shape. The unshaped reflecting surface can be a hyperboloid/ellipsoid (subreflector) or paraboloid (main reflector). The proposed method modified (2.1) to represent the shaped surface:

$$z = f_{surf}(x, y) \cdot \delta(x, y) \ . \tag{2.2}$$

Here, *δ(.)* is defined as the *distortion function*. The distortion function has multiple parameters that determine the nature of the function. By adjusting these parameters, any required shape surface can be synthesized. The form of the distortion function depends on the nature of the surface. A general expression of *δ(.)* for circularly symmetric reflectors is given in Chapter 3.

The proposed design method defines the subreflector surface with (2.2). The main reflector is synthesized using GO method. Differential evolution (DE) optimization algorithm [15] is used to find the optimum parameters of *δ(.)* for desired results. The scattered fields are numerically evaluated using methods that will be discussed in the following Sections.

The method is used to synthesize shaped hyperboloidal and shaped ellipsoidal surfaces. It is shown in Chapter 3 that the method successfully defined practical shaped surfaces. The performances of the shaped surfaces defined by this method are evaluated in the following chapters.

Although the work is limited to circularly symmetric cases, by choosing appropriate distortion function, the proposed method is expected to applicable for other cases as well.

2.4 Common Numerical Methods of Reflector Antenna Analysis

Most electromagnetic problems are complex in nature and closed form solutions of fields are rarely possible. So, numerical methods are necessary. There are many accurate numerical methods for antenna analysis. But not all these methods can be efficiently used for reflector antenna analysis. For example, finite element (FEM) method and finite difference time domain (FDTD) method are not suitable for reflector antenna analysis due to the large size of the reflecting surfaces compared to the wavelength of radiation. Method of moments (MoM) is another method which is impossible to use economically for reflectors larger than a few wavelengths [1]. The commonly used methods are geometrical optics (GO), geometrical theory of diffraction (GTD) and uniform theory of diffraction (UTD), physical optics (PO), equivalent current method (ECM) and aperture field (AF) method. These methods are more suitable for analysis of reflector antennas. Short descriptions of these methods are provided next.

2.4.1 GO method

GO method is the most commonly used methods for reflector analysis. The method is easy to implement and it is computationally convenient. The reflected field at an observation point is assumed to be dominantly depended on the incident field on a small area of the reflecting surface [16]. So, field values over the entire reflecting surface are not necessary for the calculation of reflected field at an observation region. The assumption that reflection is a local phenomenon dramatically reduces computational complexity. This makes it one of the most popular methods for reflector analysis [12], [16]. However, the method has some limitations. It ignores the fields diffracted from the edge of the reflecting surfaces. As a result, the method predicts zero field values at shadow regions, which is inaccurate. This results in discontinuous fields. It also reduces the accuracy of the results in other regions. GO also fails in caustic regions [16]. It still remains a popular choice analysis of single or dual reflector antennas.

2.4.2 GTD and UTD methods

The inability of GO method to account for the diffracted fields led to the development of GTD. The first GTD method was developed by Keller in the 1950s. A list of earlier works on GTD can be found in [16]. The method added diffracted field terms along with the reflected field terms of GO. The earlier GTD methods suffered from the problem that the fields became singular in shadow regions. UTD is the uniform version of GTD. It solved the singular field problem by introducing a transition function [16]. GTD and UTD are much more accurate compared to GO and it has been widely used in various types of reflector analysis [11], [17]. However, UTD fails in caustic regions like GO. The diffraction coefficient calculations increase computational complexity. The method remains popular because it gives more accurate results compared to GO, and requires less computation compared to PO and other methods which involve the radiation integral [18].

2.4.3 PO method

The PO method formulates radiated field by performing integration of the currents over entire reflecting surface. The exact integral (without approximations) is used to formulate the fields. But the currents used in the integral are not exact. The currents are approximated from the field incident on the reflecting surface. These currents are often referred to as *PO currents* [1]. Although these currents do not accurately describe the actual currents on the reflecting surfaces, they represent the actual currents closely. Therefore, the results from the integral are sufficiently accurate for many applications. One of the main problems of the PO method is that the radiation integration must be performed for every observation point [4]. The integration is carried out over the entire reflecting surface. As the integration must be repeated for every observation point, the PO method becomes extremely computationally demanding. Some works have been done to for finding efficient way to evaluate the radiation integral and make the method faster [14]. Despite the complexities, PO is used in many cases where accurate results are needed [19].

2.4.4 ECM, AF and other methods

ECM method uses the concept of fictitious current over the reflecting surface to formulate scattered fields [16]. The method has been successfully used to formulate fields near the caustic regions where UTD fails [18]. Another useful method is the AF method. It calculates the tangential field component at hypothetical aperture plane in front of the reflecting surface using GO/UTD techniques. The far-field at an arbitrary observation point is obtained using equivalence theorem [1].

There are a few other methods that are sometimes used for reflector antenna analysis. Physical theory of diffraction (PTD) is a modified version of PO that is more accurate. All of these methods have their own advantages and disadvantages. A summary of the relative performance of the methods can be found in [18].

2.5 Numerical Methods Used

In this thesis, a combination of the methods described in the previous section will be used. Any many cases, using a combination of two methods is more computationally efficient than using a single method [19]. For the dual reflector systems discussed in this thesis, the fields from the feed are first reflected by the subreflector and then those fields are reflected by the main reflector. For calculation of fields scattered by the subreflector, UTD method is used. For calculations of field from the main reflector, PO method is used. The combination of the two methods is termed as UTD/PO method.

A common method of dual reflector analysis is GO/PO [19]. The UTD/PO method used in this work is expected to be more accurate as UTD is more accurate than GO. The fields scattered by the subreflector cover a large angular region. Applying PO method over this large region is not efficient. For this reason, PO is rarely used on subreflectors. GO or UTD methods are more suitable for these cases. During the optimization process, GO is used to approximate the subreflector scattered field as it requires less processing time compared to UTD. But for final subreflector scattered field calculations, UTD is used. On the other hand, the field reflected by the main reflector usually spans a small angular region near the axis of the reflector. PO is very suitable for such cases as it gives very accurate for small angular regions near the axis. This region covers the main lobe of the antenna along with the significant sidelobes. The small observation region of interest also implies that the PO radiation integral will have to be evaluated at a relatively small number of points. For these reasons, UTD/PO method is selected as the analysis method for this thesis.

2.6 Conclusion

Brief discussions of several design and analysis methods of reflector antennas have been discussed in this chapter. A method of designing shaped reflector surfaces has been proposed. An efficient hybrid UTD/PO method is chosen for numerical analysis of scattered fields. The design method along with the numerical analysis will be covered in the following chapters.

CHAPTER 3

GEOMETRY OF THE SHAPED REFLECTORS

3.1 Introduction

The radiation characteristics of a shaped dual reflector antenna system depend on the geometrical shape and position of the reflecting surfaces. The size of the reflectors and the relative position of the reflectors and the feed antenna are important design parameters. The design of the feed antenna is dependent on the geometry. The geometry also significantly affects the radiation characteristics of the antenna. The shape of the reflector surfaces can be modified from the standard hyperboloid-paraboloid (for Cassegrain geometry) or ellipsoid-paraboloid (for Gregorian geometry) to improve the radiation performance of the antenna. Optimum shaped dual reflector can outperform traditional dual reflector systems in terms of beamwidth, gain, compactness and size reduction, aperture efficiency etc.

This chapter starts with a description of dual reflector geometries and the dimension parameters used for analysis. After that, a method of defining shaped hyperboloidal and shaped ellipsoidal subreflector surfaces is described. Next, verification of the capability of this method to accurately describe practical shaped reflector surfaces is presented. It is followed by representation of the shaped subreflector surfaces using differential geometry. The surface and the normal vector at each point of the surface are defined in this section. The co-ordinate system used throughout this thesis is also covered in this section. The chapter concludes with the GO based synthesis of the main reflector surface and highlighting the difference between the shaped and unshaped surfaces.

3.2 Geometry of the Dual Reflector Systems

This section presents the geometry of the traditional Cassegrain and Gregorian dual reflector systems. The geometry of the shaped dual reflector systems will be very similar to these geometries. The position of the feed antenna the reflectors will be unchanged. The focus points of the traditional dual reflector geometries are constant, but for shaped reflector systems, the focus points can not be defined easily. Each point on the reflector surfaces correspond to different focus points. The shift in focus point of the shaped subreflector is compensated by corresponding shift of the focus of the shaped main reflector. So, the focus point positions are not very important for analysis. Therefore, the basic dual reflector geometry presented here will provide sufficient description of both shaped and unshaped reflector systems.

3.2.1 Cassegrain geometry

The geometry of a Cassegrain dual reflector system is shown in Fig. 3.1.

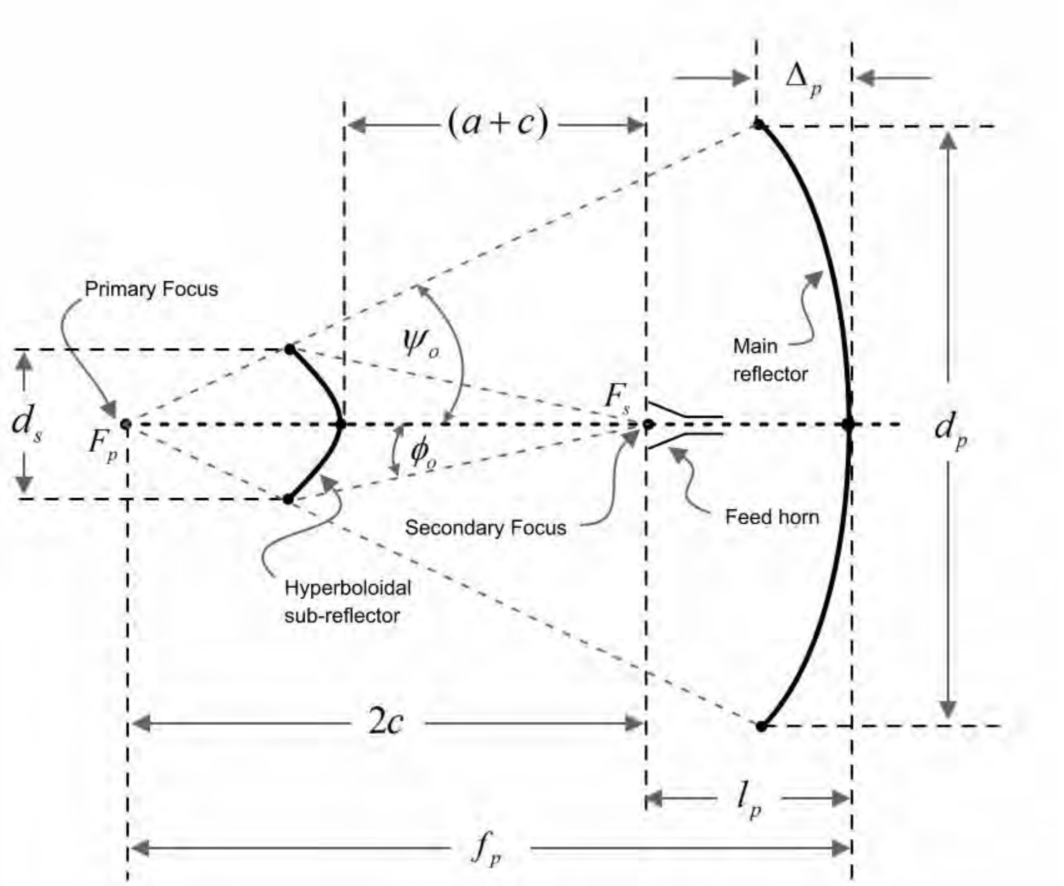

Fig. 3.1: Geometry of a Cassegrain dual reflector antenna.

The antenna system consists of a feed antenna, a hyperboloidal subreflector and a paraboloidal main reflector. The main reflector is often termed as the *primary reflector*. In most cases, a horn is sued as the feed antenna. For this reason, a horn is shown as a feed antenna in Fig. 3.1. The hyperboloid has two focus points [20]. One of these focus points coincide with the focus of the paraboloid [4], [21]. This point is known as the primary focus, F_p [3]. The other focus point coincides with the phase center of the feed antenna [1]. This is known as the secondary focus, F_s [3]. The positioning of the reflectors and feeds at these points ensure that an incoming plane wave will be focused in phase at the secondary focus (for receiving case). Also, spherical wave front generated by the feed antenna will be transformed to a plane wave front (for transmitting case).

The following parameters describe the geometry of the Cassegrain system:

d_p = diameter of the main reflector,
f_p = focal length of the main reflector,
d_s = diameter of the subreflector,
2c = distance between the foci,
$e = c/a$ = subreflector eccentricity,
Δ_p = depth of the paraboloid,
l_p = distance from feed to paraboloid vertex, and,
ψ_o, ϕ_o = opening half angle of the main reflector and subreflector respectively.

3.2.2 Gregorian geometry

The Gregorian dual reflector geometry is shown in Fig. 3.2.

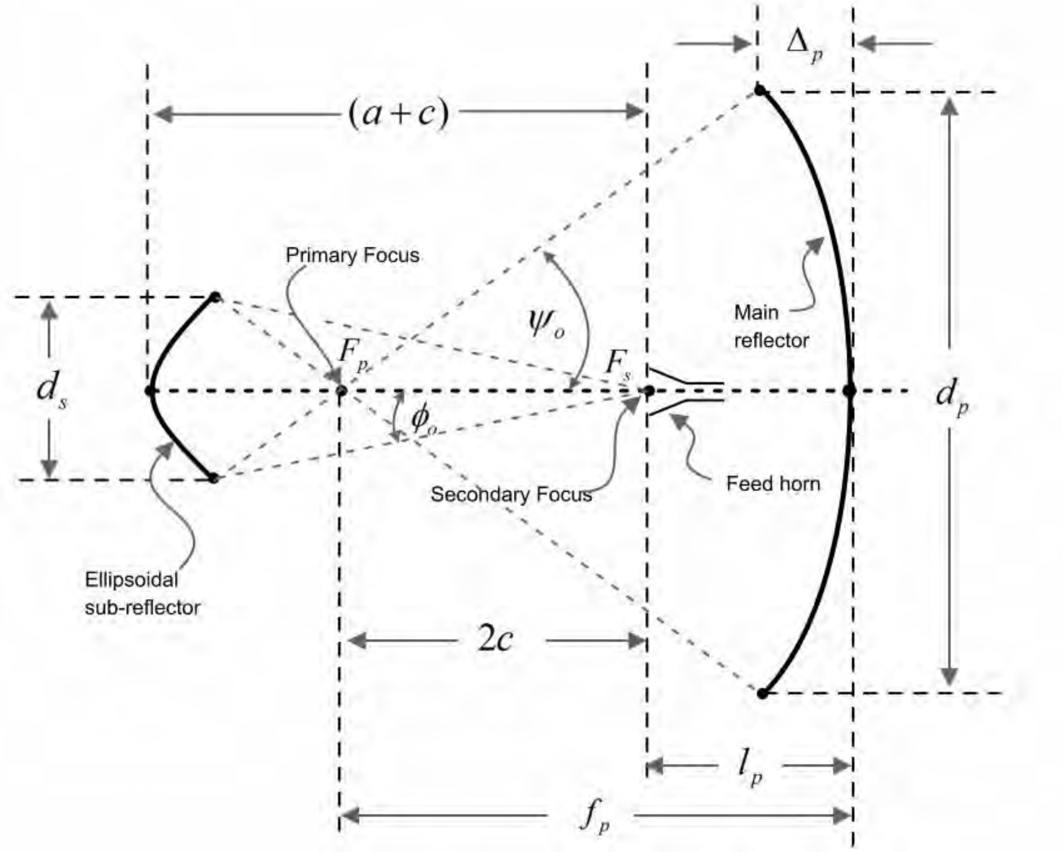

Fig. 3.2: Geometry of a Gregorian dual reflector antenna.

The antenna system consists of a feed antenna, an ellipsoidal subreflector and a paraboloidal main reflector. The only difference between the Cassegrain and Gregorian geometry is the subreflector shape. The two focus points of the ellipsoid fall on the same side of the subreflector surface. In the Cassegrain system, the hyperboloid focus points are at opposite sides of the subreflector surface. So, the ellipsoidal subreflector has ray caustic at real space compared to the ray caustic of the hyperboloidal subreflector which is at virtual space [16]. The geometrical parameters in Fig. 3.2 are identical to the ones described in Fig. 3.1 and Section 3.2.1. Therefore, the description is not repeated. The eccentricity of the ellipsoid is less than unity, where as it was larger than unity for the hyperboloid.

3.3 Dimension Parameters

The geometries described in Fig. 3.1 and Fig. 3.2 has numerous dimension parameters. However, only four independent dimensional parameters are required to be defined [22]. The other parameters can be found using geometrical relations found in literature [3], [22].

Table 3.1: Dimensional parameters of the dual reflector geometries.

Dimensional parameter	Cassegrain geometry	Gregorian geometry
Main reflector diameter, d_p	10 m	10 m
Main reflector focal length, f_p	5 m	5 m
Subreflector diameter, d_s	1.25 m	0.78 m
Distance of the feed from main reflector vertex, l_p	1 m	2.9072 m
Distance between the foci, $2c$	4 m	2.0928 m
Depth of the main reflector, Δ_p	1.25 m	1.25 m
Eccentricity, e	1.4261	0.7199
Opening half angle of the main reflector, ψ_o	53.13°	53.13°
Opening half angle of the sub-reflector ϕ_o	10.037°	9.31°

For numerical analysis, a set of typical dimensional parameters are selected. The parameters are listed in Table 3.1. The numerical values are taken from Granet's paper [22]. For a main reflector diameter of 10 m, the geometrical parameter values selected are standard values used by antenna designers. The operating frequency is taken to be 14 GHz through out the thesis.

3.4 Defining Shaped Subreflector Surfaces

A shaped subreflector is no longer hyperboloidal or ellipsoidal. The focus points of such shaped subreflectors are not well defined. However, the geometrical features of these shaped surfaces are very similar to the geometrical features of unshaped hyperboloidal/ellipsoidal surfaces. Due to these similarities, the shaped surfaces can be considered as a distorted form of the unshaped surfaces. The method presented in this thesis is based on the modifications of the unshaped surface equations to define the shaped surfaces. The method of visualizing the shaped surface as perturbed/distorted form of unshaped surface has not been reported in literature yet.

The shaping of the subreflector surfaces is significant to extract the best performance from the dual reflectors. The shape of main reflector is directly depended on the shape of the subreflector. Shaped subreflector surfaces for both shaped Cassegrain and shaped Gregorian geometries are discussed in the following sub-sections.

3.4.1 Shaped hyperboloidal subreflector surface

The Cassegrain geometry uses a hyperboloidal subreflector. The unshaped hyperboloid must be defined before the shaped surface can be defined. It is assumed that the feed antenna is located at the origin and direction of feed radiation is towards the negative z axis. So, the hyperboloid must be located at the negative side of the z axis. One of the focuses of the hyperboloid must be at origin so that it coincides with the feed. The equation of such a hyperboloidal surface symmetric around the z axis is given by the following equation [20]:

$$\frac{(z+c)^2}{a^2}-\frac{x^2+y^2}{b^2}=1 \quad . \tag{3.1}$$

Where,

$$b^2=c^2-a^2 \, . \tag{3.2}$$

The parameters a and c are related to the position of the vertex and focus of the hyperboloid as shown in Fig. 3.1 [20]. The parameter ρ_s is defined as the radius of surface point projected on the xy plane. It is related to x and y by:

$$\rho_s^2 = x^2 + y^2 \quad . \tag{3.3}$$

Equation (3.1) can be modified as:

$$\frac{(z+c)^2}{a^2} - \frac{\rho_s^2}{b^2} = 1, \tag{3.4}$$

$$z = -c - \frac{a}{b}\sqrt{b^2 + \rho_s^2} \quad . \tag{3.5}$$

For a circularly symmetric shaped subreflector, (3.4) and correspondingly (3.5), needs to be modified. A *distortion function*, *δ(.)* is introduced in the equations to get the shaped surface:

$$\frac{(z+c)^2}{a^2} - \frac{\rho_s^2}{b^2}\delta\left(\rho_s\right) = 1 \ , \tag{3.6}$$

$$z = -c - \frac{a}{b}\sqrt{b^2 + \rho_s^2\delta\left(\rho_s\right)} \quad . \tag{3.7}$$

The distortion function, *δ(.)* must be a function of ρ_s to maintain circular symmetry. The shape of the surface depends on the expression of *δ(.)*. Through literature review, it is found that shaped hyperboloidal subreflectors are usually different from unshaped hyperboloids near the edges [11]. The shaped surface curves towards the vertex at the edges. An exponential function with arguments containing even powers of ρ_s can give the desired shaped. The following generalized expression of the distortion function is developed:

$$\delta(\rho_s) = \exp\left(\sum_{n=1}^{N} \tau_n \rho_s^{2n\zeta_n}\right) \quad . \tag{3.8}$$

The function contains 2N number of parameters denoted by τ_n and ζ_n. Here, τ_n is denoted to as the n^{th} amplitude distortion parameter and ζ_n is denoted to as the n^{th} exponent distortion parameter. The parameters together are termed as *distortion parameters*. For high values of N, the control over the curvature of the surface is more precise. But it increase the number of parameters required to define the surface. It is found that for practical subreflector surfaces, $N = 2$ is sufficient and only 4 parameters are required to define the surface. $N = 2$ is used through out this thesis.

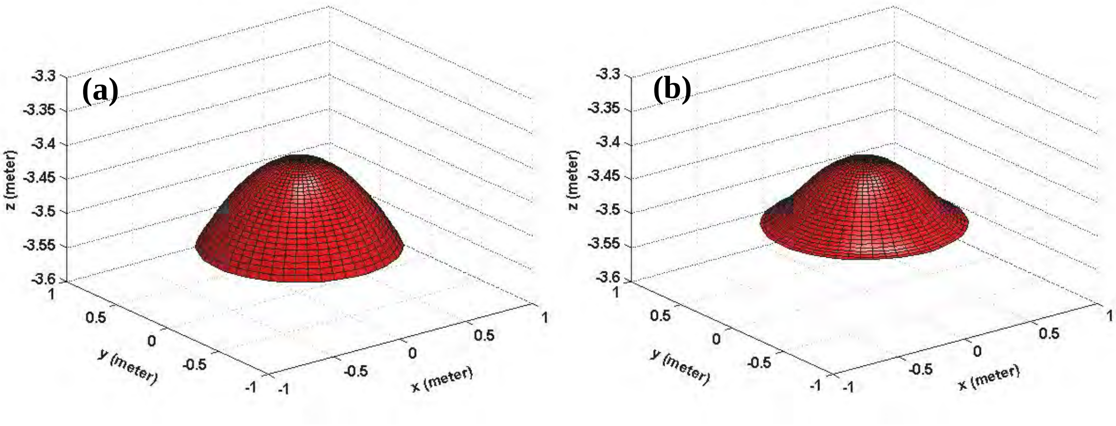

Fig. 3.3: Three dimensional representation of the subreflector surface for (a) unshaped hyperboloid, (b) shaped hyperboloid.

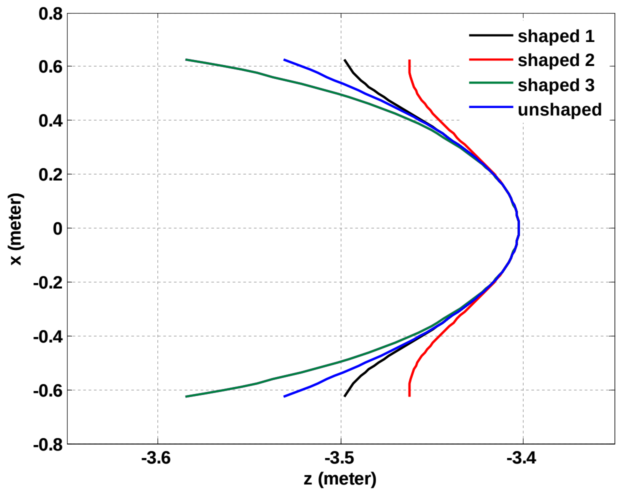

Fig. 3.4: Multiple shaped hyperboloidal subreflector surfaces defined by varying sets of distortion function parameters.

An unshaped surface and a shaped surfaces defined by (3.8) along with (3.7) is shown in Fig. 3.3. It can be seen that the shaped surface has the desired curvature near the edge. The value of the distortion parameters for Fig. 3.3 are: $\tau_1 = -3.8923$, $\zeta_1 = 2.0005$, $\tau_2 = 1.0112$, and $\zeta_2 = 0.6803$. By varying these 4 parameters, almost any desired shaped hyperboloid can be defined. Fig. 3.4 shows multiple shaped hyperboloids in the *xz* plane defined by various sets of values of the distortion parameters. It can be observed that, the shaped surface can curve in both directions compared to the unshaped surface by using appropriate values of the distortion parameters. So, (3.8) along with (3.7) can define wide range of shaped hyperboloid surfaces.

3.4.2 Shaped ellipsoidal subreflector surface

The shaped ellipsoidal subreflector surface is defined in a similar way as the shaped hyperboloidal surface was defined. An unshaped ellipsoid with one focus on the origin and symmetric around the z axis can be defined by the following equation [20]:

$$\frac{(z+c)^2}{a^2}+\frac{x^2+y^2}{b^2}=1 \ . \tag{3.9}$$

Where,

$$b^2=a^2-c^2 \, . \tag{3.10}$$

Using (3.3) in (3.9):

$$\frac{(z+c)^2}{a^2}+\frac{\rho_s^2}{b^2}=1 . \tag{3.11}$$

Introducing the distortion function in (3.11):

$$\frac{(z+c)^2}{a^2}+\frac{\rho_s^2}{b^2}\delta\left(\rho_s\right)=1 \ , \tag{3.12}$$

$$z=-c-\frac{a}{b}\sqrt{b^2-\rho_s^2\delta\left(\rho_s\right)} \ . \tag{3.13}$$

It is found that the distortion function defined in (3.8) can be used to define shaped ellipsoidal surfaces as well. So, defining another distortion function is not necessary.

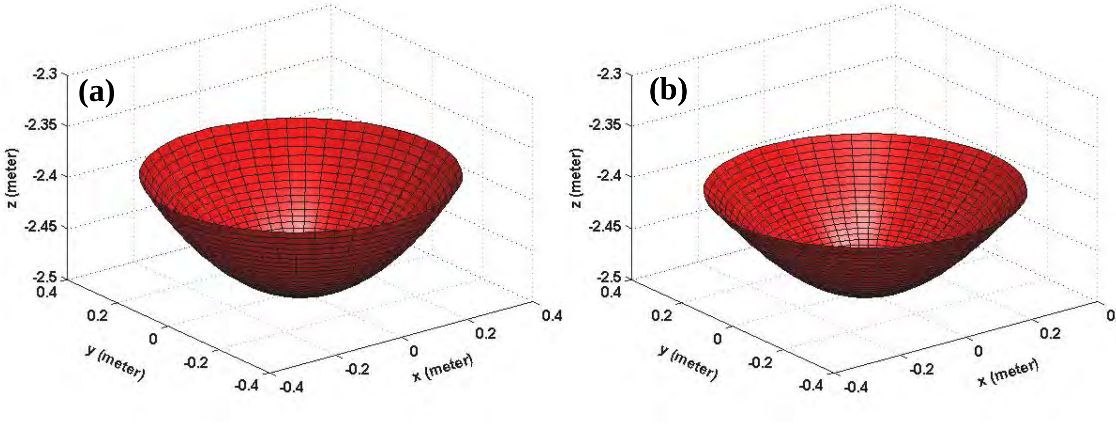

Fig. 3.5: Three dimensional representation of the subreflector surface for (a) unshaped ellipsoid, (b) shaped ellipsoid.

An unshaped surface and a shaped surfaces defined by (3.13) along with (3.7) is shown in Fig. 3.5. It can be seen that the shaped surface curves towards the vertex direction near the edges. It is found form literature review that most ellipsoidal shaped subreflectors have this characteristic [23]. The value of the distortion parameters for Fig. 3.5 are: $\tau_1 = -4.1986$, $\zeta_1 = 1.7049$, $\tau_2 = 1.0213$, and $\zeta_2 = 0.9257$.

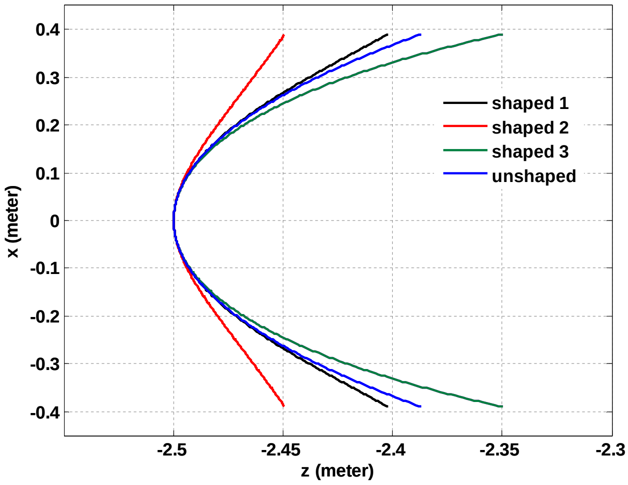

Fig. 3.6: Multiple shaped hyperboloidal subreflector surfaces defined by varying sets of distortion function parameters.

By varying the 4 distortion parameters, almost any desired shaped ellipsoid can be defined. Fig. 3.6 shows multiple shaped hyperboloids in the *xz* plane defined by various sets of values of the distortion parameters.

3.5 Representing Practical Shaped Subreflector Surfaces

It is seen that the using the distortion function defined in (3.8), the surfaces represented by (3.7) and (3.13) can resemble shaped hyperboloidal/ellipsoidal reflector surfaces.

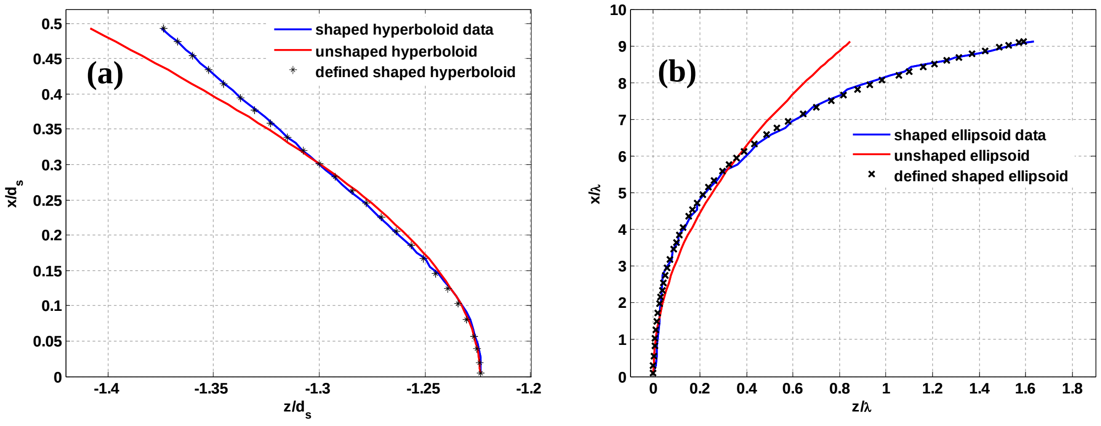

Fig. 3.7: Representation of practical shaped subreflector surfaces: (a) shaped hyperboloid, (b) shaped ellipsoid.

However, it is necessary to establish that practical shaped subreflector surfaces can be accurately represented by these equations. Practical data of a shaped hyperboloidal and shaped ellipsoidal subreflector surfaces are taken from literature [11], [23]. The dimensions are normalized with respect to subreflector diameter in [11] and with respect to wavelength in [23]. Equations (3.7) and (3.13) along with (3.8) are used to find a surface that closely resembles these surfaces. By adjusting the distortion parameters, it is found that surfaces very close to these can be generated. The results are shown in Fig. 3.7. It is clear that the unshaped surfaces are very different from the shaped surface in both cases. With, $\tau_1 = -3.3363$, $\zeta_1 = 0.5706$, $\tau_2 = 2.1697$, and $\zeta_2 = 0.1951$, the sum of squares of the error between the defined shaped hyperboloidal surface and the practical data of [11] is 3.2×10^{-5}. Similarly, with, $\tau_1 = 1.1394$, $\zeta_1 = 0.4987$, $\tau_2 = -1.4815$, and $\zeta_2 = 0.2126$, the sum of squares of the error between the defined shaped ellipsoidal surface and the practical data of [23] is 2.3×10^{-2}. So, in both cases, the derived equations represent the practical shaped surfaces very closely.

3.6 Differential Geometry Based Analysis of Shaped Subreflector Surfaces

Analysis methods of reflector antennas are often related to differential geometry. Specially, the reflected field analysis using GO methods often require formulation using differential geometric quantities [16]. Many calculations of PO and UTD require differential geometry. In this Section, using differential geometry, the shaped subreflector surfaces and the normal vectors on the surfaces will be defined.

3.6.1 Analysis of the shaped hyperboloidal surface

The shaped hyperboloidal surface defined by (3.7) can be represented using parameters ρ_s and ϕ_s in differential geometrical form as [16], [24]:

$$\mathbf{r} = \rho_s \cos\phi_s\,\hat{\mathbf{x}} + \rho_s \sin\phi_s\,\hat{\mathbf{y}} - \left[c + \frac{a}{b}\sqrt{b^2 + \rho_s^2 \delta(\rho_s)} \right] \hat{\mathbf{z}} \quad . \tag{3.14}$$

Here, (ρ_s, ϕ_s) is the polar co-ordinates of the projection of a surface point on the *xy* plane. The unit normal vector, $\hat{\mathbf{n}}_s$, is defined by the following equation [25]:

$$\hat{\mathbf{n}}_s = \frac{\dfrac{\partial \mathbf{r}}{\partial \rho_s} \times \dfrac{\partial \mathbf{r}}{\partial \phi_s}}{\left| \dfrac{\partial \mathbf{r}}{\partial \rho_s} \times \dfrac{\partial \mathbf{r}}{\partial \phi_s} \right|} \quad . \tag{3.15}$$

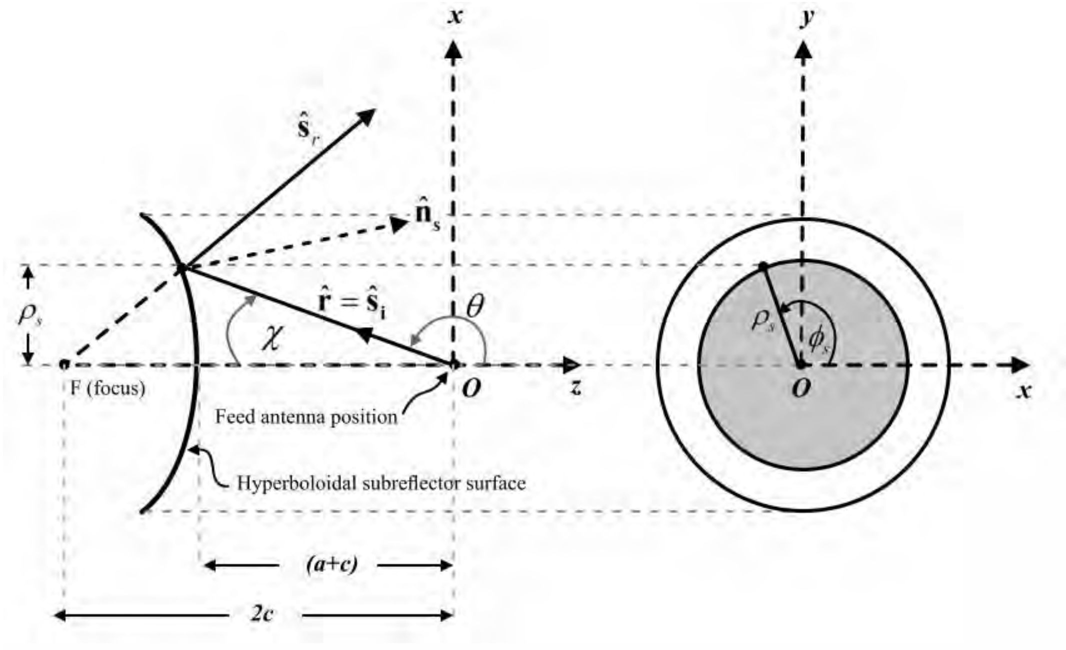

Fig. 3.8: Differential geometrical representation of the shaped hyperboloid.

The differential geometrical parameters along with the co-ordinate system are shown in Fig. 3.8. The incident ray vector ($\hat{\mathbf{s}}_\mathbf{i}$) and the reflected ray vector ($\hat{\mathbf{s}}_\mathbf{r}$) are also shown in Fig. 3.8. As the unit normal vector is required for many calculations later, (3.15) needs to be evaluated. The partial derivates can be calculated from (3.14) using (3.8):

$$\frac{\partial \mathbf{r}}{\partial \rho_s} = \cos\phi_s\,\hat{\mathbf{x}} + \sin\phi_s\,\hat{\mathbf{y}} - \left[\frac{a}{2b}\frac{\rho_s\delta(\rho_s)\left\{\sum_{n=1}^{N}\tau_n\rho^{2n\zeta_n}+2\right\}}{\sqrt{b^2+\rho_s^2\delta(\rho_s)}}\right]\hat{\mathbf{z}}\ , \tag{3.16}$$

$$\frac{\partial \mathbf{r}}{\partial \phi_s} = -\rho_s\sin\phi_s\,\hat{\mathbf{x}} + \rho_s\cos\phi_s\,\hat{\mathbf{y}}\ . \tag{3.17}$$

Substituting these values in (3.15):

$$\hat{\mathbf{n}}_\mathbf{s} = \frac{\Lambda(\rho_s)\cos\phi_s}{\sqrt{\Lambda^2(\rho_s)+\Delta_H^2(\rho_s)}}\hat{\mathbf{x}} + \frac{\Lambda(\rho_s)\sin\phi_s}{\sqrt{\Lambda^2(\rho_s)+\Delta_H^2(\rho_s)}}\hat{\mathbf{y}} + \frac{\Delta_H(\rho_s)}{\sqrt{\Lambda^2(\rho_s)+\Delta_H^2(\rho_s)}}\hat{\mathbf{z}}\ . \tag{3.18}$$

Where,

$$\Delta_H(\rho_s) = 2b\sqrt{b^2+\rho_s^2\delta(\rho_s)}\ , \tag{3.19}$$

$$\Lambda(\rho_s) = a\delta(\rho_s)\varepsilon(\rho_s)\ , \tag{3.20}$$

$$\varepsilon(\rho_s) = \rho_s\left\{\sum_{n=1}^{N}\tau_n\rho^{2n\zeta_n}+2\right\}. \tag{3.21}$$

These equations will be used in the following chapters for field calculations.

3.6.2 Analysis of shaped ellipsoidal surface

The shaped ellipsoidal surface defined by (3.13) can be represented using parameters ρ_s and ϕ_s in differential geometrical form as [16], [24]:

$$\mathbf{r} = \rho_s \cos\phi_s \,\hat{\mathbf{x}} + \rho_s \sin\phi_s \,\hat{\mathbf{y}} - \left[c + \frac{a}{b}\sqrt{b^2 - \rho_s^2 \delta(\rho_s)} \right] \hat{\mathbf{z}} \quad . \tag{3.22}$$

Here, (ρ_s, ϕ_s) is the polar co-ordinates of the projection of a surface point on the *xy* plane. The parameters along with the co-ordinates system is shown in Fig. 3.9.

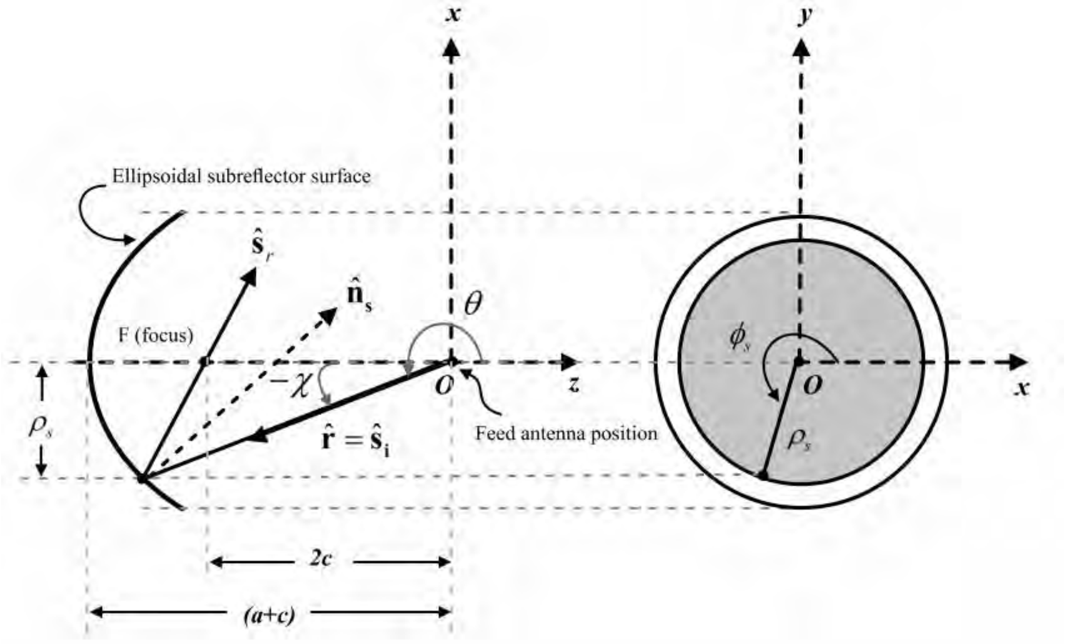

Fig. 3.9: Differential geometrical representation of the shaped ellipsoid.

The only difference between (3.14) and (3.22) is the sign of the second term inside the squire root. The normal vector is still defined by (3.15). The partial derivatives for the shaped ellipsoidal surface are calculated to be:

$$\frac{\partial \mathbf{r}}{\partial \rho_s} = \cos\phi_s \,\hat{\mathbf{x}} + \sin\phi_s \,\hat{\mathbf{y}} + \left[\frac{a}{2b} \frac{\rho_s \delta(\rho_s) \left\{ \sum_{n=1}^{N} \tau_n \rho^{2n\zeta_n} + 2 \right\}}{\sqrt{b^2 - \rho_s^2 \delta(\rho_s)}} \right] \hat{\mathbf{z}} \quad , \tag{3.23}$$

$$\frac{\partial \mathbf{r}}{\partial \phi_s} = -\rho_s \sin\phi_s \,\hat{\mathbf{x}} + \rho_s \cos\phi_s \,\hat{\mathbf{y}} \quad . \tag{3.24}$$

Using (3.15), the normal vector is found to be:

$$\hat{\mathbf{n}}_\mathrm{s} = -\frac{\Lambda(\rho_s)\cos\phi_s}{\sqrt{\Lambda^2(\rho_s)+\Delta_E^2(\rho_s)}}\hat{\mathbf{x}} - \frac{\Lambda(\rho_s)\sin\phi_s}{\sqrt{\Lambda^2(\rho_s)+\Delta_E^2(\rho_s)}}\hat{\mathbf{y}} + \frac{\Delta_E(\rho_s)}{\sqrt{\Lambda^2(\rho_s)+\Delta_E^2(\rho_s)}}\hat{\mathbf{z}} \ . \quad (3.25)$$

Where,

$$\Delta_E(\rho_s) = 2b\sqrt{b^2-\rho_s^2\delta(\rho_s)} \ . \quad (3.26)$$

$\Lambda(\rho_s)$ and $\varepsilon(\rho_s)$ are defined by (3.20) and (3.21) respectively. These derived equations will be used in the following chapters for field calculations.

3.7 Defining Shaped Main Reflector Surface

In a dual reflector system, the shape of the main reflector is completely dependent on the shape of the subreflector. Once the shape of the subreflector is defined, the main reflector must be shaped so that the path lengths of the rays are constant at an observation plane perpendicular to the main reflector axis. Using GO methods to calculate the incident and reflected ray vectors, the required position of a point on the main reflector surface for a given point on the subreflector surface can be formulated.

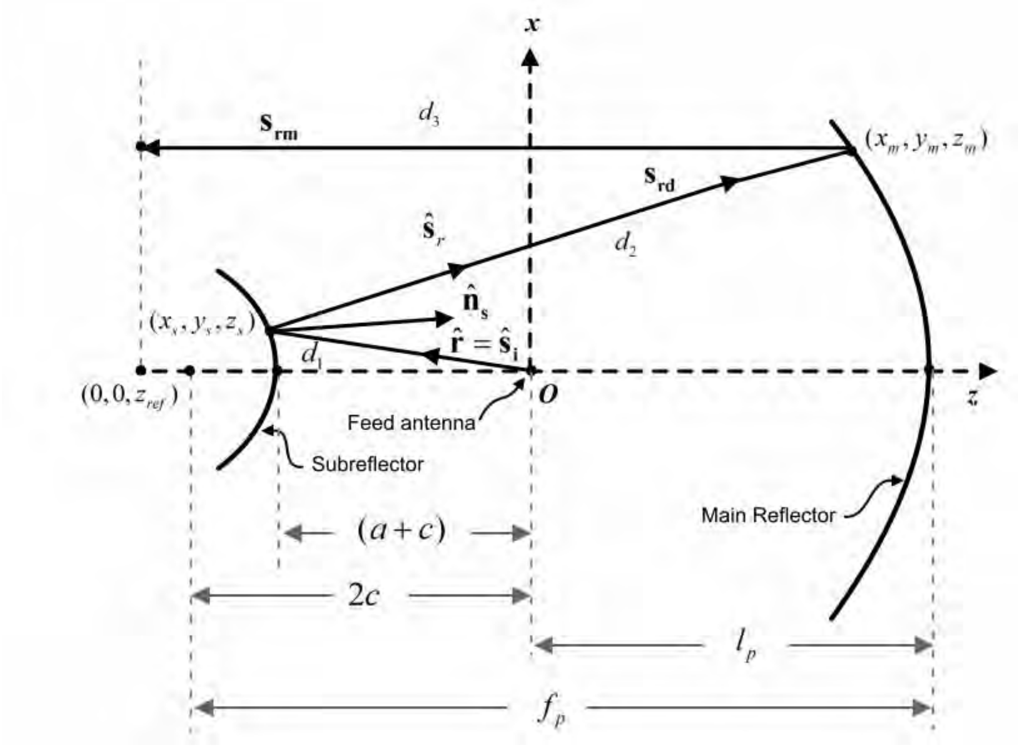

Fig. 3.10: Synthesis of main reflector surface for a given shaped subreflector.

The geometry of dual reflector system with a shaped hyperboloidal subreflector is shown in Fig. 3.10. An observation plane is defined parallel to the *xy* plane. In the two dimensional diagram of Fig. 3.10, the observation plane is shown as line parallel to x axis going through the point ($0, 0, z_{ref}$). For a ray emitted from the feed, the sum of the distances d_1, d_2 and d_3 must be constant (k_1), irrespective of the position of reflection on the subreflector surface. So,

$$d_1 + d_2 + d_3 = k_1 \quad . \tag{3.27}$$

The distance k_1 can be calculated by considering an axial ray from the feed (along the z axis). From Fig. 3.10, for the axial ray, the distance from feed to subreflector is ($a+c$), then the subreflector to main reflector distance is ($a+c+l_p$), and finally the distance from main reflector to observation point is ($l_p - z_{ref}$), considering z_{ref} to be a negative quantity. So, k_1 is calculated as:

$$k_1 = (a+c) + (a+c+l_p) + (l_p - z_{ref}) = 2(a+c+l_p) - z_{ref} \ . \tag{3.28}$$

The parameter l_p can be related to the geometrical parameters of the unshaped subreflector, c and the unshaped main reflector f_p as seen in Fig. 3.10.

$$l_p = f_p - 2c \quad . \tag{3.29}$$

Using (3.29) in (3.28):

$$k_1 = 2(a - c + f_p) - z_{ref} \quad . \tag{3.30}$$

The distance d_1 is related to the co-ordinates of the subreflector surface point (x_s, y_s, z_s) as:

$$d_1 = \sqrt{x_s^2 + y_s^2 + z_s^2} \quad . \tag{3.31}$$

The reflected ray from the main reflector is parallel to the z axis. The distance d_3 can easily be related to the co-ordinates of the main reflector surface point (x_m, y_m, z_m) as:

$$d_3 = z_m - z_{ref} \quad . \tag{3.32}$$

To calculate distance d_2, it is necessary to calculate the reflected ray vector. The unit vector in the direction of the reflected ray is found from GO method and is given by [16]:

$$\hat{\mathbf{s}}_\mathbf{r} = \hat{\mathbf{s}}_\mathbf{i} - 2\left(\hat{\mathbf{n}}_\mathrm{s} \cdot \hat{\mathbf{s}}_\mathbf{i}\right)\hat{\mathbf{n}}_\mathrm{s} \ . \tag{3.33}$$

Where,

$$\hat{\mathbf{s}}_\mathbf{i} = \hat{\mathbf{r}} = \frac{\mathbf{r}}{|\mathbf{r}|} \quad . \tag{3.34}$$

The vector $\mathbf{r}$ is defined by (3.14) or (3.22) and $\hat{\mathbf{n}}_\mathrm{s}$ is defined by (3.18) or (3.25) depending on the subreflector shape. Once the unit vector along the reflected ray is formulated, the reflected ray vector, $\mathbf{s_{rd}}$ defined from the reflection point on the subreflector surface can be defined as:

$$\mathbf{s_{rd}} = \hat{\mathbf{s}}_{\mathbf{r}} d_2 + x_s \hat{\mathbf{x}} + y_s \hat{\mathbf{y}} + z_s \hat{\mathbf{z}} \ . \tag{3.35}$$

Equation (3.35) can be reorganized as:

$$\mathbf{s_{rd}} = \left\{ \left(\hat{\mathbf{s}}_{\mathbf{r}} \cdot \hat{\mathbf{x}} \right) d_2 + x_s \right\} \hat{\mathbf{x}} + \left\{ \left(\hat{\mathbf{s}}_{\mathbf{r}} \cdot \hat{\mathbf{y}} \right) d_2 + y_s \right\} \hat{\mathbf{y}} + \left\{ \left(\hat{\mathbf{s}}_{\mathbf{r}} \cdot \hat{\mathbf{z}} \right) d_2 + z_s \right\} \hat{\mathbf{z}} \ . \tag{3.36}$$

The components of this vector indicate the co-ordinates of the main reflector [24], [25]. So,

$$\left. \begin{aligned} x_m &= \left(\hat{\mathbf{s}}_{\mathbf{r}} \cdot \hat{\mathbf{x}} \right) d_2 + x_s \\ y_m &= \left(\hat{\mathbf{s}}_{\mathbf{r}} \cdot \hat{\mathbf{y}} \right) d_2 + y_s \\ z_m &= \left(\hat{\mathbf{s}}_{\mathbf{r}} \cdot \hat{\mathbf{z}} \right) d_2 + z_s \end{aligned} \right\} . \tag{3.37}$$

Substituting the value of z_m from (3.37) to (3.32):

$$d_3 = \left(\hat{\mathbf{s}}_{\mathbf{r}} \cdot \hat{\mathbf{z}} \right) d_2 + z_s - z_{ref} \ . \tag{3.38}$$

Now, replacing (3.38) and (3.31) in (3.21):

$$d_2 = k_1 - d_1 - d_3 = 2\left(a - c + f_p \right) - z_{ref} - \sqrt{x_s^2 + y_s^2 + z_s^2} - \left\{ \left(\hat{\mathbf{s}}_{\mathbf{r}} \cdot \hat{\mathbf{z}} \right) d_2 + z_s - z_{ref} \right\} \ . \tag{3.39}$$

Solving for d_2:

$$d_2 = \frac{2\left(a - c + f_p \right) - \sqrt{x_s^2 + y_s^2 + z_s^2} - z_s}{1 + \left(\hat{\mathbf{s}}_{\mathbf{r}} \cdot \hat{\mathbf{z}} \right)} \ . \tag{3.40}$$

Equation (3.40) can be used to calculate d_2 for a given subreflector surface point and it can be replaced in (3.37) to calculate corresponding main reflector surface point. Thus the derived equations can synthesize the main reflector surface for an arbitrary subreflector surface. Although Fig. 3.10 shows the diagram for a shaped hyperboloidal subreflector, the derived equations can be used for shaped ellipsoidal subreflector surfaces as well.

To verify the method, the main reflectors for an unshaped hyperboloid and an unshaped ellipsoid are synthesized. It is known that the main reflector shaped should be an exact paraboloid for both these cases. The results are shown in Fig. 3.11. It is found that the surfaces are exact paraboloidal surfaces. Thus the method is verified.

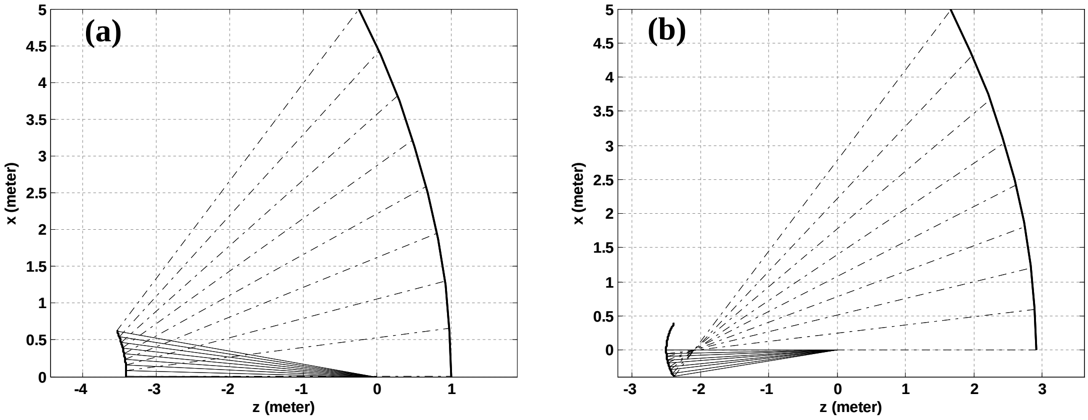

Fig. 3.11: Synthesis of main reflector surfaces for:
(a) unshaped hyperboloidal subreflector, (b) unshaped ellipsoidal subreflector.

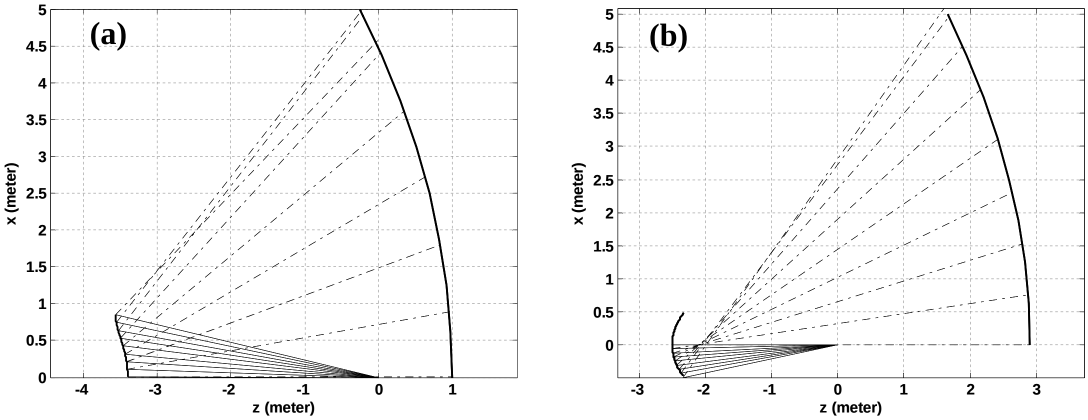

Fig. 3.12: Synthesis of main reflector surfaces for:
(a) shaped hyperboloidal subreflector, (b) unshaped ellipsoidal subreflector.

The main reflector surfaces for a shaped hyperboloidal subreflector and a shaped ellipsoidal subreflector are synthesized using (3.37) and (3.40). The results are shown in Fig. 3.12. The shaped hyperboloidal subreflector surface used here, is defined by the parameters shown in Table 3.1 with the subreflector diameter extended to 1.7 m and the distortion parameter set: $\tau_1 = -3.3928$, $\zeta_1 = 1.7212$, $\tau_2 = 2.5015$, and $\zeta_2 = 0.7184$. Similarly, the shaped ellipsoidal subreflector surface used here, is defined by the parameters shown in Table 3.1 with the subreflector diameter extended to 0.98 m and the distortion parameter set: $\tau_1 = -3.7836$, $\zeta_1 = 1.6870$, $\tau_2 = 1.2241$, and $\zeta_2 = 0.6001$. The significance of the used distortion parameter set will be explained in following chapters. Although, the results for only one pair of shaped surfaces are shown here, the main reflector synthesis method described here is general.

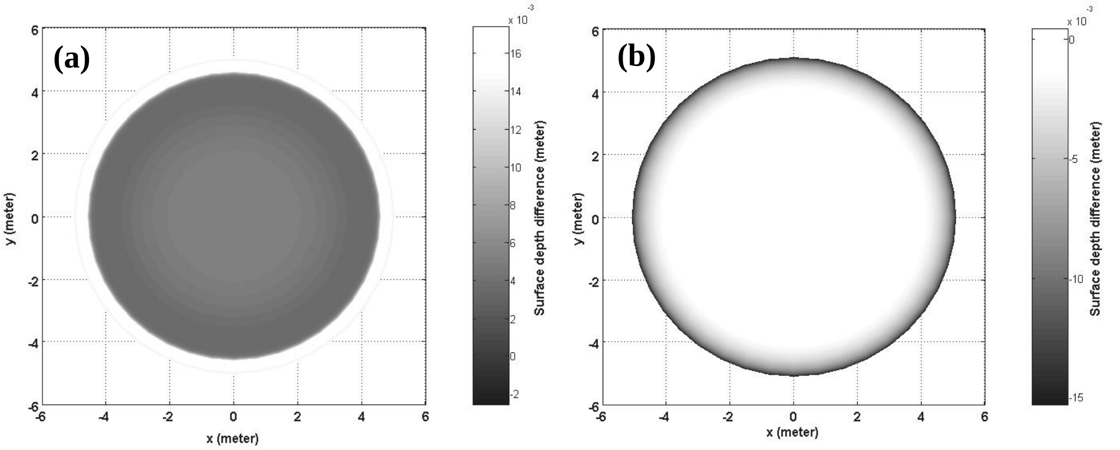

Fig. 3.13: Difference of surface depth of the shaped main reflector compared to unshaped main reflector for: (a) shaped Cassegrain geometry, (b) shaped Gregorian geometry.

The difference between the shaped main reflector surfaces shown in Fig. 3.12 and the unshaped main reflector surfaces shown in Fig. 3.11 is not noticeable in Fig. 3.12 and Fig. 3.11. This is because of the fact that, the distortion of the main reflector surface is very small. The difference in unshaped main reflector surface and shaped main reflector surface is shown in Fig. 3.13. It shows the *xy* plane view of the main reflector surface. The shadings in the contour plot indicate the difference of the surface depths (difference of z values) of the shaped main reflector compared to the unshaped main reflector. The depth difference is mostly positive for the shaped Cassegrain system, implying that the shaped main reflector curves towards the positive z axis more compared to the unshaped main reflector. The depth difference is negative for the shaped Gregorian system, implying that the shaped main reflector curves towards the negative z axis more compared to the unshaped main reflector. In both cases, the depth difference high towards the edge of the main reflector. This is expected as the shaped subreflector also differs from the unshaped subreflector towards the edge region.

3.8 Conclusion

In this chapter, a method of defining shaped subreflector surfaces has been presented. Important geometrical parameters have been defined. Also, the method of synthesizing shaped main reflector surface for a given shaped subreflector has been discussed. The geometries defined in this chapter will be used in the following chapters for field calculations.

CHAPTER 4

FEED ANTENNA DESIGN

4.1 Introduction

One of the most important parts of a reflector antenna system is the feed antenna. A feed antenna supplies energy to (or receives energy from) the reflectors. For this reason, feed antennas are often referred to as *primary feed* and the reflectors are referred to as the *secondary antenna*. For the same reason, the radiation pattern of the feed antenna is known as the *primary pattern* and the radiation pattern of the composite reflector system is known as the *secondary pattern* [5]. Most of the radiation characteristics of the secondary antenna depend on the characteristics of the feed antenna. The proper choice of feed antenna is determined by the application of the secondary antenna. The design procedure of the feed antenna takes into account the frequency band of operation, the geometry of the reflectors, and other radiation parameters.

This chapter starts with a discussion on desired characteristics of a feed antenna followed by brief description of different types of feed antennas. After that, the design requirements are discussed. A conical corrugated horn is found to be a suitable feed antenna as it meets all the design criteria. The geometry of the corrugated horn antenna is described. The dimensions of the horn and the corrugations are designed for optimum performance for Ku band frequencies. The chapter concludes with the calculation and analysis of radiation characteristics of the horn antenna.

4.2 Desired Characteristics of Feed Antennas

An antenna must have a set of specific radiation characteristics to be used as a feed antenna. The radiation parameters of the feed antenna must be within specific range for practical applications. The desired range of these parameters depends on the application of the antenna. A properly designed feed will have optimum values of these parameters which will increases the overall performance of the reflector antenna. For optimum design, it is necessary to know the important radiation parameters and the desired range of their values. A brief description on the desired characteristics of a feed antenna is provided next.

4.2.1 Radiation pattern

An axially symmetric radiation pattern is usually desired for a feed antenna. A symmetric primary pattern can produce a symmetric secondary pattern. In a dual reflector system, the feed antenna illuminates the subreflector. The feed antenna pattern should be such that the entire subreflector surface is illuminated by the main lobe. The ratio of the field strength at the edge of the illuminated surface to the maximum field strength on the illuminated surface is known as *edge taper* [2]. The edge taper of the main reflector depends on the edge taper of the subreflector. The edge taper of the subreflector depends on the radiation pattern of the feed. The edge taper of the main reflector is related to the beamwidth and sidelobe levels of the secondary pattern [3]. High value of edge taper gives high gain, but it also increases spillover loss. Typical value of main reflector edge taper is around –12 dB [2]. The radiation pattern of the feed antenna must be such that it provides the desired taper. As the position of the edge of the subreflector is depended on the geometry of the reflector system, the geometry must be knows before designing the feed. For a –12 dB edge taper, the –12 dB beamwidth of the feed antenna must be equal to twice the opening-half angle (or half-subtended angle) of the subreflector.

4.2.2 S_{11} parameter

The reflection coefficient of an antenna is known as the S_{11} parameter. The S_{11} parameter of a feed antenna indicates how much power is transmitted towards the reflectors and how much power is reflected back due to the mismatch between the medium and the feed antenna. Low value of S_{11} parameter is desirable. For satellite ground station reflector antennas, feed reflection coefficient value below –17.7 dB is desirable [2]. S_{11} parameter is a function of operating frequency. So, it is necessary for feed antenna to have low S_{11} parameter value throughout the entire operating frequency band. Well designed microstrip feeds can have very low values of S_{11} parameter [26].

4.2.3 Polarization

Electric field radiated by an antenna can be either linearly polarized or circularly polarized. For both cases, the electric field can be separated into two components: the desired polarization or the copolarized component and the usually undesired cross-polar component [2]. These components are orthogonal to each other. Copolar and cross-polar field components can be calculated from the expression of radiated electric field of the antenna using Ludwig's definition of cross-polarization [27]. Cross-polarization becomes important when two orthogonal polarizations are used to transmit two different communication channels at the same frequency. Frequency reuse by using dual polarization effectively doubles the bandwidth of the antenna. If an antenna suffers from high cross polarization, then it will have significant power in both polarizations. In such cases, the orthogonal polarizations will interfere with each other resulting in a very low signal to interference ratio (SIR). The high interference level will make the antenna unsuitable for practical communication systems.

Feed antennas are often used in reflector antennas used in communication systems. In such cases, orthogonal polarizations are used to create two communication channels having the same frequency. So, the feed antenna must have low cross-polarization level to create sufficient isolation between the two channels.

4.2.4 Bandwidth

The bandwidth of an antenna is defined as the frequency range over which the performance of the antenna is satisfactory [2]. The parameter most commonly used to measure the antenna performance is reflection coefficient (S_{11} parameter). Other parameters like: beamwidth, gain, cross-polarization level etc. can also be used to calculate bandwidth. In practical cases, effective bandwidth of an antenna is defined as the frequency range over which all the desired parameters have acceptable values. Feed antennas used in communication systems must have bandwidth greater or equal to the bandwidth of the communication channels.

4.3 Different Types of Feed Antennas

There are many different types of feed antennas. Small dipoles, open-ended waveguides, horn antennas, microstrip patches, arrays, traveling wave antennas etc. are used as feed antennas [2]. Each of these types of feed antennas has certain qualities which makes them suitable for specific applications. A brief description of commonly used feed antennas for reflector antenna system is presented next.

4.3.1 Horn antennas

Horn antennas are the most commonly used feed antennas. Their simple geometry, and directive radiation characteristics makes them suitable as feeds of reflector antennas. Horn antennas of various geometries exist. Horn antennas can be pyramidal or conical in shape. The profile of the flare section of the horn can be linear, Gaussian or other curved shaped. Horns can also be dielectric filled or hollow. The inside walls of a horn antenna can be smooth or corrugated. The most common horn antennas are the smooth-walled pyramidal horn and the smooth-walled conical horn. But these horns usually do not have axially symmetric radiation pattern [2], which is a desired characteristic of feed antennas. Potter horns use discontinuities or steps to excite higher order modes, which improve the radiation characteristics and produce a more symmetric pattern [1]. Conical corrugated horns have corrugated inner surface which creates hybrid modes [1]. This creates symmetric radiation pattern and low cross polarization level. For these reason Potter horns and corrugated horns are often used as feed antennas.

4.3.2 Microstrip feeds

Microstrip patch antennas can be used in feed applications. Microstrip arrays are often used as feeds instead of single microstrip patch. The main advantage of microstrip antennas is that it can be easily integrated to electronics. Unlike a horn antenna, the radiation pattern of a microstrip array can be electronically controlled to create a phased array. A reflector antenna with a phased array feed in known as Hybrid Antenna (HA) [26]. Such antennas have high gain and also provide beam scanning capability, which makes it suitable for RADAR applications. The excitation of the array elements can be controlled to provide any type of illumination for the reflectors. This gives control over the gain and sidelobe level of the secondary pattern. Microstrip antennas also have smaller size and lower weight compared to a horn antenna.

Microstrip antennas are more difficult to fabricate compared to horn antennas. Creating a phased array feed with microstrip patches require expensive electronic circuits and instruments. Microstrip antennas usually have asymmetric pattern and have high cross polarization levels [2]. In most communication applications, horn antennas are a better choice compared to microstrip antennas as feed antennas. Microstrip feed is suitable in applications where the primary feed pattern needs to be changed, or very specific illumination of the reflector surface is required.

4.4 Design Requirements and Selection of Feed Antenna Type

The design requirements and the subsequent selection of feed antenna type depend on the application of the overall antenna system. The dual reflector antennas presented in this thesis is designed for communication system application. Communication antennas used for satellite ground station or deep space communication has similar set of design requirements. Dynamic primary radiation pattern is usually not necessary for such applications. So, horn antennas are preferred as feed antennas over microstrip patches. As communication systems require low reflection coefficient and low cross-polarization level, conical corrugated horn antenna with linear flare is selected as the desired feed antenna type. Also, the geometry of the Cassegrain and Gregorian dual reflector requires –12 dB beamwidth of the feed to be 10.04° and 9.28° respectively, for a –12 dB edge taper at the subreflector surface.

4.5 Conical Corrugated Horn Antenna

The conical corrugated horns must be designed based on the frequency of operation and reflector geometry. Since both Cassegrain and Gregorian dual reflector systems are discussed in this thesis, corrugated horn feeds for both geometries is designed. Both horns are designed for Ku-band frequencies. The geometry, field characteristics and design parameters of the corrugated horns are discussed in the following sections.

4.5.1 Geometry of the conical corrugated horn

A cross sectional view of a conical corrugated horn is shown in Fig. 4.1. Here, a_H is the aperture radius of the horn, a_w is the radius of the feed waveguide, L_H is the length of the horn, L_{Hf} is the length of the horn flare section, and θ_{Hf} is the semi-flare angle of the horn. As the horn is rotationally symmetric, the two dimensional view of Fig. 4.1 gives complete description of the horn geometry.

The inside walls of the flare section of the horn is corrugated. Part of the waveguide section may also be corrugated. The corrugated surface can be visualized as a series of *slots* and *teeth*. A zoomed in view of the corrugated surface is shown in Fig. 4.1. Here, d_n is the depth of the nth corrugation, w_n is the width of the nth slot, and t_n is the width of nth tooth.

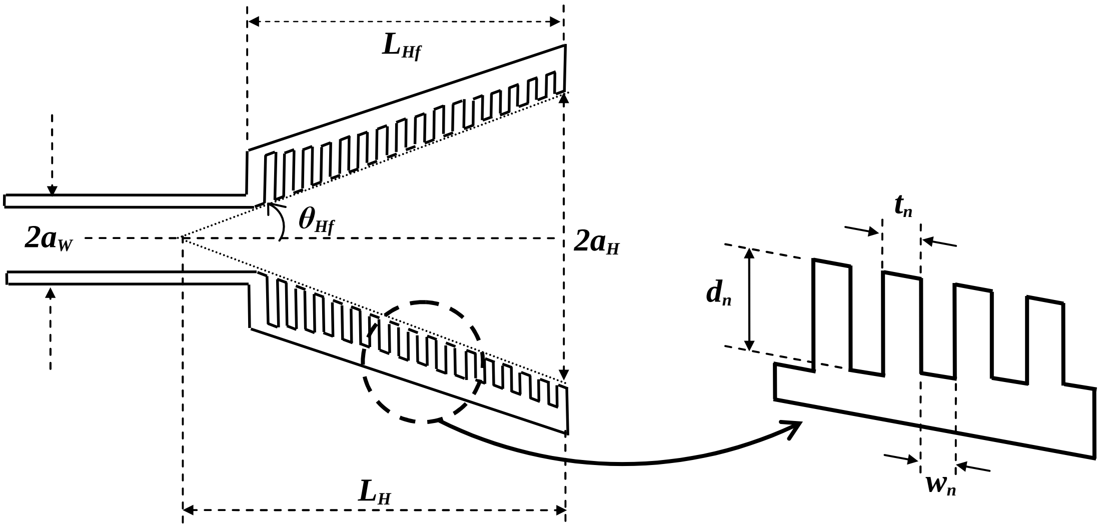

Fig. 4.1: Geometry of a conical corrugated horn antenna.

4.5.2 Design of the horn

For design, the Ku-band operating frequency of 14 GHz is selected. First, the corrugated surface needs to be defined. Conical corrugated horn antennas with uniform corrugations are much simpler to fabricate compared to antennas in which each corrugation has different depths and widths. Keeping the corrugation length uniform does not significantly hamper the performance of the horn for most applications. The corrugation depth is taken to be a quarter of the operating wavelength for optimum performance [1]. The tooth width is taken to be 20% of slot width ($t = 0.2w$), and slot width is taken to be 10% of wavelength ($w = 0.1\lambda$) [2].

The aperture radius and the length of the horn are selected based on the required beamwidth of the horn. For a given beamwidth, the horn gain can be approximated [21]. For the current design problem, the –12 dB beamwidth of 10.04° and 9.28° is required for the Cassegrain and the Gregorian geometry respectively. Using simple equations, the horn length and aperture radius can be calculated [2]. The waveguide radius is selected from the standard Ku-band waveguide sizes. The waveguide radius can be selected independently without effecting L_H and a_H as L_{fH} adjusted (within limits) without effecting the horn performance significantly. The geometric parameters are fine tuned after performing far-field analysis of the horn. The final design of the feed horns for Cassegrain and Gregorian system is given table 4.1.

Table Error! No text of specified style in document.**.1: Design parameters of the feed horns.**

Dimension parameter	Feed horn for the Cassegrain geometry	Feed horn for the Gregorian geometry
Aperture radius, a_H	63 mm	69 mm
Horn length, L_H	380 mm	380 mm
Semi-flare angle, θ_{Hf}	9.4°	10.3°
Waveguide radius, a_W	15.08 mm	15.08 mm
Horn flare length, L_{fH}	289 mm	297 mm
Corrugation depth, d_n	5.36 mm	5.36 mm
Slot width, t_n	0.43 mm	0.43 mm
Tooth width, w_n	2.14 mm	2.14 mm
Number of slots	112	116

The number of slots (or the number of corrugations) is calculated from the t_n, w_n and L_{fH}, assuming that the corrugations only exist in the flare section. The design parameters of both horns are similar because of the similarity in the size of the Cassegrain and Gregorian geometries considered here. These designs are made for the *unshaped* reflector systems. Slight modifications are needed for shaped reflectors. This happens because the beamwidth requirement of the feed changes as the subreflector is shaped. But the only the horn aperture radius is required to be modified slightly for such cases. The change in radiation performance is negligible for such variations.

4.5.3 Radiation characteristics

The radiation characteristics of the conical corrugated horn antenna are determined by the mode of propagation of electromagnetic waves inside the horn. Corrugated horns support *hybrid* modes. The hybrid modes are distinguished from the TE and TM modes by the non-zero field components in the direction of propagation. The dominant mode in a conical corrugated horn antenna is HE_{11} mode, which is combination of TE_{11} and TM_{11} modes [1]. The radiation from the horn operating in HE_{11} mode near balanced hybrid conditions can be formulated using aperture field methods. Radiated fields of horn antennas are often expressed in terms spherical field components. For far-field region, the spherical components of the radiated electric field for $\theta_{Hf} < 35°$ can be approximated as [1] by the following equations:

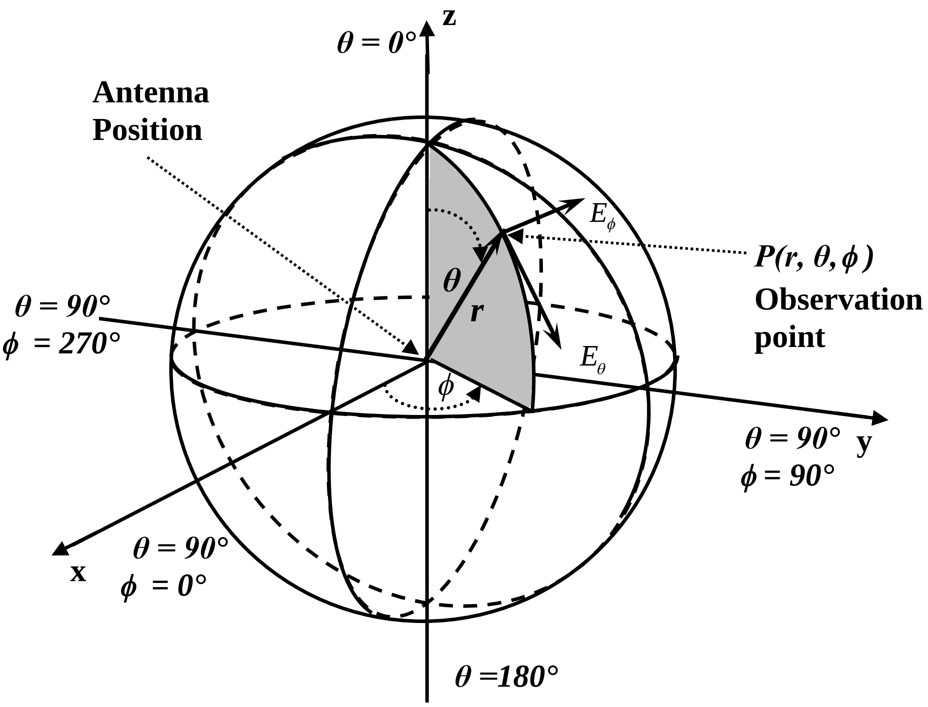

Fig. 4.2: Thee dimensional co-ordinate system showing electric field components.

$$E_\theta(r,\theta,\phi) = E_o k a_H \frac{e^{-jkr}}{r} F_\theta G_0(w)\cos\phi , \tag{4.1}$$

$$E_\phi(r,\theta,\phi) = -E_o k a_H \frac{e^{-jkr}}{r} F_\phi G_0(w)\sin\phi . \tag{4.2}$$

Here, (r,θ,ϕ) is the spherical co-ordinates of the observation point, E_θ and E_ϕ are spherical field components as shown in Fig. 4.2. The direction of propagation is assumed to be along positive z axis with the horn being located at the origin. $G_0(w)$ is given by the integration:

$$G_0(w) = \frac{1}{a_H^2}\int_0^{a_H} J_0\left(p_{11}\,\rho'/a_H\right) J_0\left(w\rho'\right)\exp\left(-jk\,\rho'^2/2L_H\right)\rho' d\rho' \ . \tag{4.3}$$

F_θ and F_ϕ are obliquity factors and are given by:

$$F_\theta = \frac{1}{2}\left[1+\frac{\beta}{k}\cos\theta + \Gamma\left(1-\frac{\beta}{k}\cos\theta\right)\right], \tag{4.4}$$

$$F_\phi = \frac{1}{2}\left[\cos\theta + \frac{\beta}{k} + \Gamma\left(\cos\theta - \frac{\beta}{k}\right)\right]. \tag{4.5}$$

Here,

$k =$ wave number $= 2\pi/\lambda$ (λ = wavelength),

$E_o =$ amplitude of the dominant HE_{11} mode,

$w = k\sin\theta =$ angular co-ordinate,

$\Gamma =$ reflection co-efficient at the horn aperture,

$J_m(.) =$ Bessel functions of the first kind & order *m*,

$p_{11} = 1.84118$ = first non-vanishing root of $J_1'(.)$, where, $J_1'(.)$ = first derivative of $J_1(.)$,

$\rho' =$ variable of integration, and,

$\beta =$ dominant HE_{11} mode propagation constant,

$$= k\sqrt{1-\left(\frac{2.4048}{ka_H}\right)^2} \quad .$$

The other symbols used in the equations are horn geometrical parameters discussed in section (4.5.1). The copolarized component (E_{cp}) and cross-polarized component (E_{xp}) of the electric can be computed from Ludwig's definition of cross-polarization [1], [27]. The quantities are given by the matrix equation:

$$\begin{bmatrix} E_{cp} \\ E_{xp} \end{bmatrix} = \begin{bmatrix} \cos(\phi-\phi_o) & -\sin(\phi-\phi_o) \\ -\sin(\phi-\phi_o) & -\cos(\phi-\phi_o) \end{bmatrix} \cdot \begin{bmatrix} E_\theta \\ E_\phi \end{bmatrix} \quad . \tag{4.6}$$

Where, ϕ_o is the reference direction which is taken to be 0°.

The reflection coefficient at the horn aperture can be calculated from the self admittance which is given by the equation [1]:

$$y_{11} = \frac{5.783}{(ka_H)^2}\frac{k}{\beta}\int_0^\infty \frac{w(2-w^2)}{\sqrt{1-w^2}} \times \frac{J_0^2(ka_H w)}{\left\{w^2-\left(2.4048/ka_H\right)^2\right\}^2}\, dw \quad . \tag{4.7}$$

The S_{11} parameter or the reflection coefficient is now given by:

$$S_{11} = \Gamma = \frac{1-y_{11}}{1+y_{11}} \quad . \tag{4.8}$$

Using (4.6) along with (4.1) – (4.5), the copolarized and cross-polarized far-field pattern of the design horns are calculated. Γ can be assumed negligible for these calculations. The results for the designed Cassegrain feed horn and the Gregorian feed horn at operating frequency of 14 GHz and $\phi = 0^\circ$ plane are shown in Fig. 4.3 and Fig. 4.4. The cross-polarized components are normalized with respect to the co-polarized component.

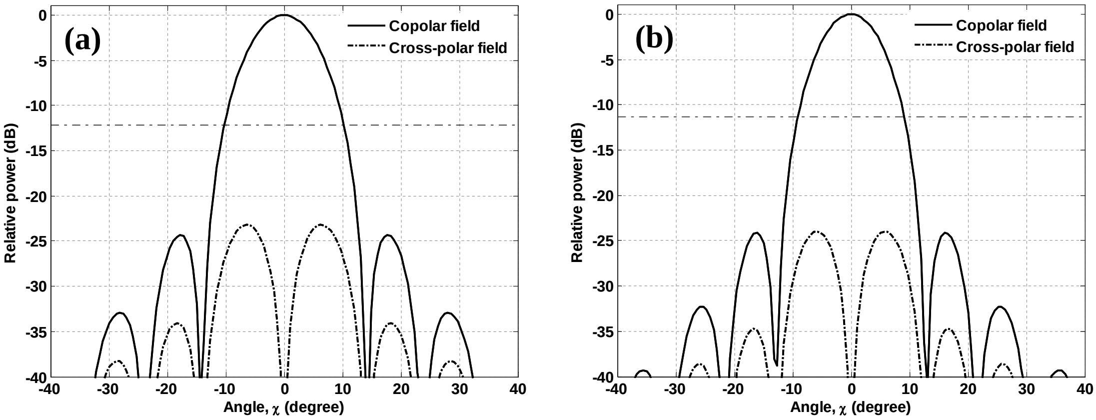

Fig. 4.3: Far field radiation pattern at 14 GHz and $\phi = 0^\circ$ plane of the conical corrugated feed horns for the (a) Cassegrain geometry, (b) Gregorian geometry.

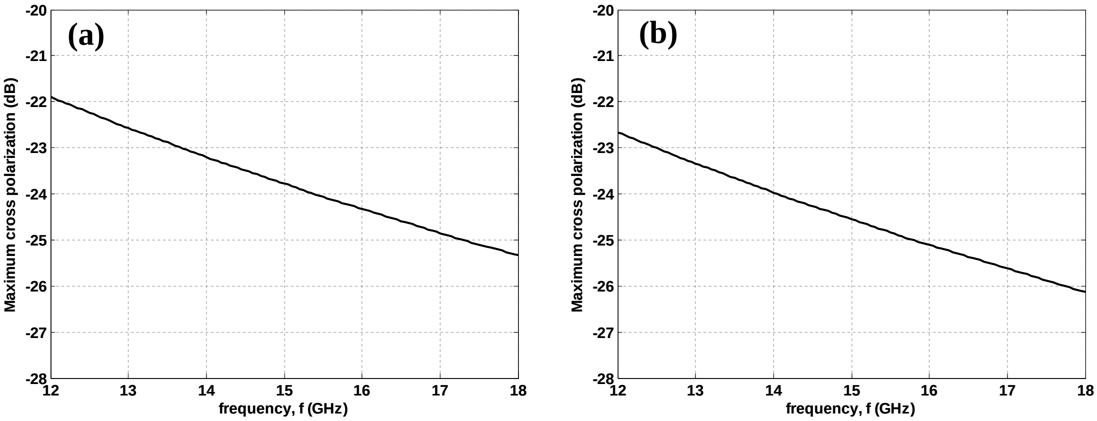

Fig. 4.4: Maximum cross-polarization level of the conical corrugated feed horns for the (a) Cassegrain geometry, (b) Gregorian geometry.

The corrugated horn has almost completely symmetric radiation pattern. So, the pattern at other ϕ planes is almost identical. The angle χ is used as the variable here which is exactly the same as θ used in the equations. So, $\chi = \theta$ in this case. χ is used here to be match notations with the dual reflector geometry.

The 10.04° and 9.28° beamwidth are indicated by a horizontal line on the curves respectively. It is seen that the taper at this angle is near –12 dB which is one of the design requirements. The cross polarization level is found to be relatively small compared to the co-polarized component. In fact, the maximum cross-polarization level is below –20 dB through out the entire Ku-band (12 – 18 GHz) for both horns as shown in Fig. 4.4.

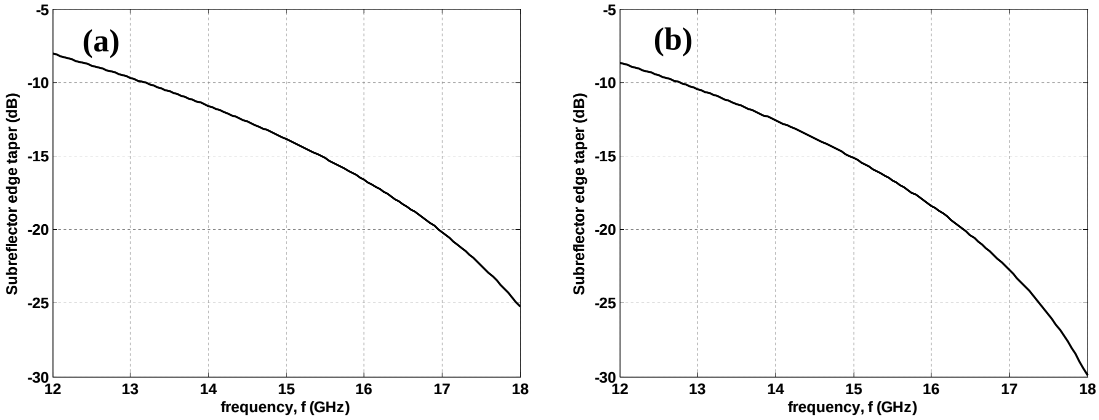

Fig. 4.5: Edge taper of the conical corrugated feed horns for the
(a) Cassegrain geometry, (b) Gregorian geometry.

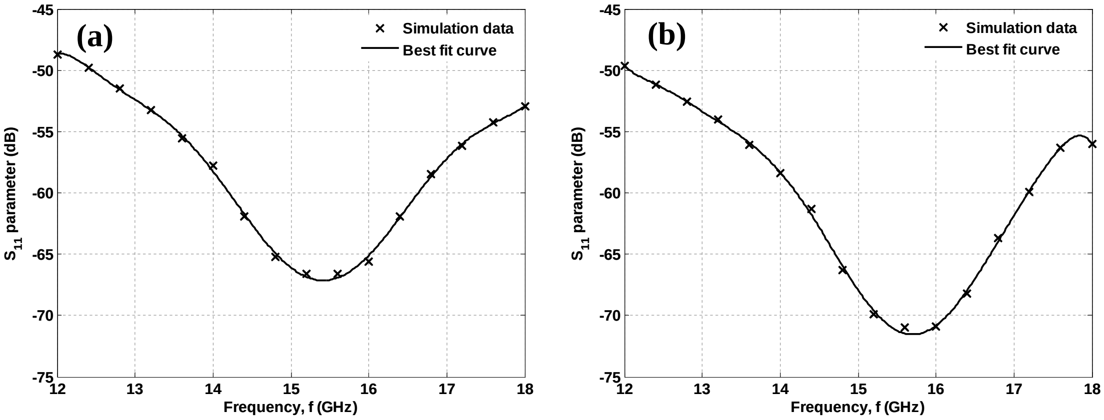

Fig. 4.6: S_{11} parameter of conical corrugated feed horns for the
(a) Cassegrain geometry, (b) Gregorian geometry.

Although the edge taper has the required value at 14 GHz, it varies with frequency. The edge taper variation with frequency is shown in Fig. 4.5. This variation leads to gain and sidelobe fluctuations of the secondary pattern with frequency. However, the variations are within acceptable limits in this case. The S_{11} parameters of the horns are calculated using (4.7) and (4.8). The results are shown in Fig. 4.6. The reflection coefficient has very small values for Ku band frequencies, as expected for corrugated horns. The values are below –45 dB, which is very satisfactory for most practical communication system applications.

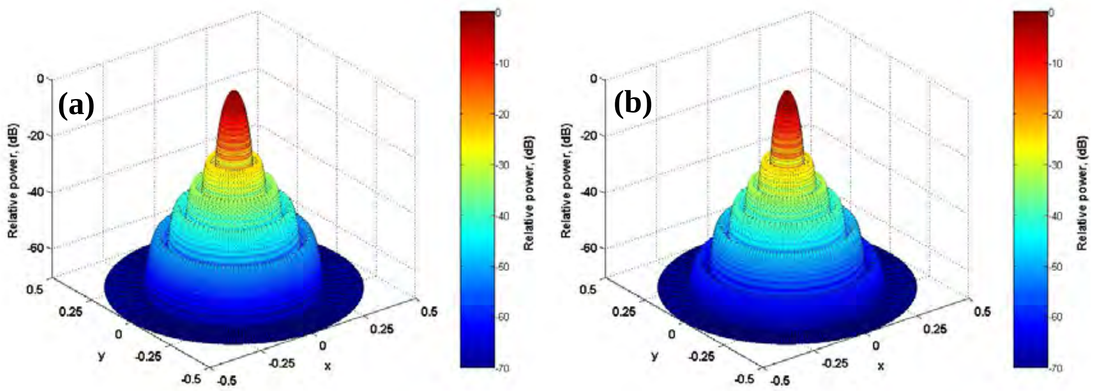

Fig. 4.7: Three dimensional radiation pattern of the designed corrugated feed horn at 14 GHz for the (a) Cassegrain geometry, (b) Gregorian geometry.

The three dimensional radiation pattern of the horn antennas at 14 GHz are shown in Fig. 4.7. As expected, the pattern is found to be highly symmetric. The peak of the surface plots indicate z axis and $\chi = \theta = 0°$. The horizontal *xy* plane indicates $\chi = \theta = \pm \pi/2$ plane. The low sidelobe levels imply that the spillover loss will be small. This makes the designed horns ideal to be used as feed antennas.

4.6 Conclusion

Based on the design requirements, conical corrugated feed horns are selected as the optimum feed antenna choice. Two feed horns are designed for the Cassegrain and the Gregorian geometry requirements respectively. The radiation characteristics of the designed horns are computed. The performance parameters of the feed antenna are selected to be beamwidth, edge taper, cross-polarization level and S_{11} parameter. After calculating these quantities, it is found that the performances of the feed horns satisfy all the design requirements. Although, the designs are made for unshaped dual reflector systems, only slight modifications of the feed antenna geometries are necessary for them to be suitable for the shaped reflector systems. The radiation characteristics of the feed horns will not change significantly due to these modifications. So, they will have characteristics almost identical to the ones described in this chapter.

CHAPTER 5

SUBREFLECTOR SCATTERED FIELD FORMULATION

5.1 Introduction

The feed antenna illuminates the subreflector is a dual reflector antenna system. Many of the radiation characteristics of the antenna system depend on the characteristics of the field scattered from the subreflector. Using the field equations of the feed antenna described in Chapter 4, the field intensity on the surface of the subreflector can be formulated. The scattered field depends on the incident field and the shape of the subreflector. The shapes of the subreflector surfaces have been covered in Chapter 3. Using these data, the scattered field can be formulated using a suitable numerical analysis method. UTD is used for this purpose here. The reasons have been discussed in Chapter 2.

This chapter starts with a discussion on the major contributing components of the scattered field and concept of ray tubes. After that, the reflected field is formulated using GO method. The observation points are defined on the surface of the main reflector. Next, the diffracted fields are computed using UTD. Finally, the overall scattered field is found from the reflected and the diffracted fields.

5.2 Components of the Scattered Field

For reflector antennas, the total scattered field from the reflecting surface results mainly from reflection and diffraction. The dominant part of the scattered field for majority of the observation region is the reflected field. GO method is a universally accepted method for reflected field calculations when the reflecting surface is large compared to the wavelength of the field [16]. The fields can be expressed as ray optic fields for such cases.

The diffracted fields originate from the edges of the reflector surface. These fields follow Keller’s law of diffraction [16]. The diffracted fields are dominant near the *shadow boundaries*. The incident shadow boundary (ISB) is defined as border where the incident field can not *directly* illuminate due to an obstacle. Similarly, the reflection shadow boundary (RSB) is defined as border where the reflected field can not *directly* illuminate due to an obstacle. The shadow regions are shown in Fig. 5.1. A flat reflecting surface is shown in Fig. 5.1 for convenience. The GO method predicts zero field values at the shadow boundaries as no incident or reflected field exist at those regions. This discontinuity in field distribution is compensated by the diffracted fields.

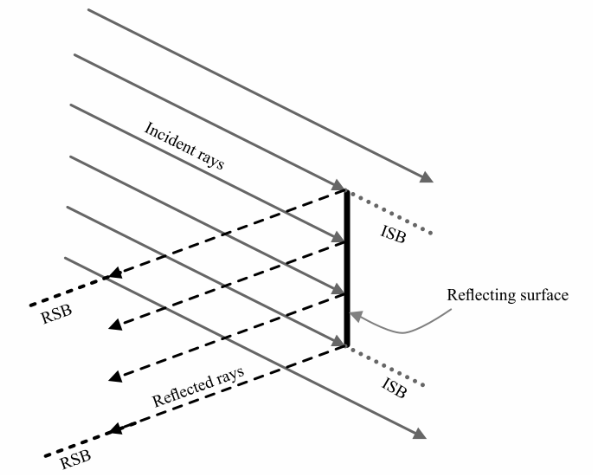

Fig. 5.1: Incident and reflection shadow boundaries.

The diffracted field has relatively small magnitude in most of the observation angles. However, near ISB and RSB, the diffracted field has significant magnitude. So, for accurate results, diffracted fields must be accounted for. UTD calculates both reflected and diffracted fields to give accurate results.

5.3 Rays Tubes

The reflected field formulation in UTD method is the same as the formulation in GO method. The fields are visualized as *ray tubes*. The energy is transported through this ray tubes in the direction of propagation. The variation of amplitude of the fields within the ray tube is determined by the law of conservation of energy [4]. An astigmatic ray tube is shown in Fig. 5.2. The direction along the ray is expressed by the variable s. An arbitrary reference point is shown in Fig. 5.2, labeled at $s = 0$. The two curved surfaces shown at $s = 0$ and $s = s$, represent two surfaces where the phase of the field is constant. These surfaces are normal to the direction of rays (direction of propagation). Such surfaces are referred to as *eikonal* [4]. The surfaces are characterized by the curvature at

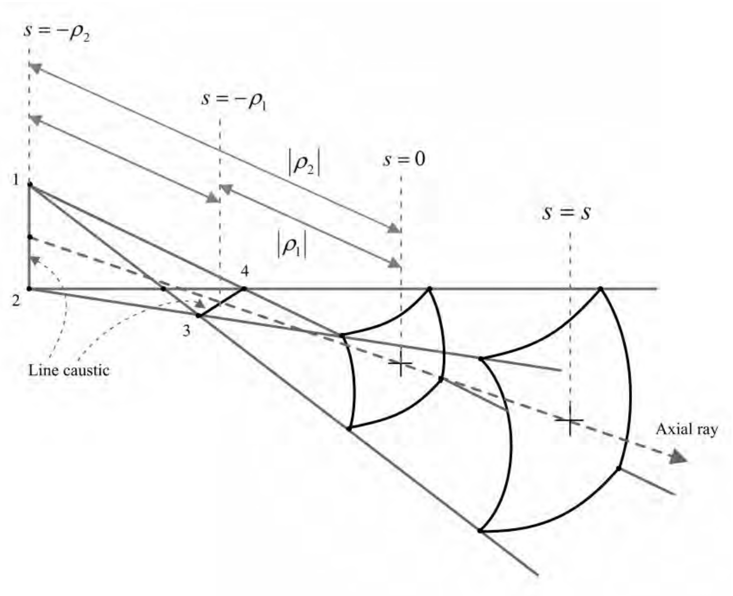

Fig. 5.2: An astigmatic ray tube.

two principal radii of curvatures ρ_1 and ρ_2, measured on the central or axial ray. The field at a point $s = s$ on the ray tube can be calculated from the field at $s = 0$ using:

$$\mathbf{E}(s) = \mathbf{E}(0)\sqrt{\frac{\rho_1\rho_2}{(\rho_1+s)(\rho_2+s)}}\exp(-jks) \quad . \tag{5.1}$$

Here, k is the wave number and **E** is the electric field along the ray tube.

Equation (5.1) gives invalid results at $s = -\rho_1$ or $s = -\rho_2$. These points are called *caustics* [16]. The linear caustic regions are highlighted in Fig. 5.2 as 1-2 line and 3-4 line. The GO fields fail to give accurate results in caustic regions. This is one of the limitations of GO methods. As the UTD uses GO to find reflected fields, it also fails in the caustic regions. However, if the observation region does not contain any caustic points, the results are sufficiently accurate.

5.4 Reflected Field Formulation

The general expression of GO reflected field at an observation point P is can be calculated from the equation [16]:

$$\mathbf{E_r}(P) = \mathbf{E_r}(Q_r)\sqrt{\frac{\rho_{1r}\rho_{2r}}{(\rho_{1r}+s_r)(\rho_{2r}+s_r)}}\exp(-jks_r) \quad . \tag{5.2}$$

Here, ρ_{1r} and ρ_{2r} are the principal radii of curvature of the reflected ray tube, s_r is the distance of the observation point along the ray, Q_r is the point of reflection, $\mathbf{E_r}(P)$ is the reflected electric field at point P, and $\mathbf{E_r}(Q_r)$ is the reflected electric field at point Q_r. $\mathbf{E_r}(Q_r)$ can be calculated from the field incident at Q_r using:

$$\mathbf{E_r}(Q_r) = -\mathbf{E_i}(Q_r) + 2\left[\hat{\mathbf{n}}_\mathbf{s} \cdot \mathbf{E_i}(Q_r)\right]\hat{\mathbf{n}}_\mathbf{s} \; . \tag{5.3}$$

Here, $\hat{\mathbf{n}}_\mathbf{s}$ is the normal on the subreflector surface defined in Section 3.6.1 and Section 3.6.2 of Chapter 3. $\mathbf{E_i}(Q_r)$ is the incident field at Q_r, which can be calculated from the feed antenna characteristic equations discussed in Section 4.5.3. The normal vector along with the observation points, feed position and point of reflection are shown in Fig. 5.3. Diagrams for the shaped hyperboloidal and shaped ellipsoidal subreflector are shown separately. The observation point, P, is defined on the main reflector surface. The main reflector surface points are found from equations derived in Section 3.7. The angle χ shown in Fig. 5.3 is related to the polar co-ordinate of Q_r. It is required to formulate $\mathbf{E_i}(Q_r)$.

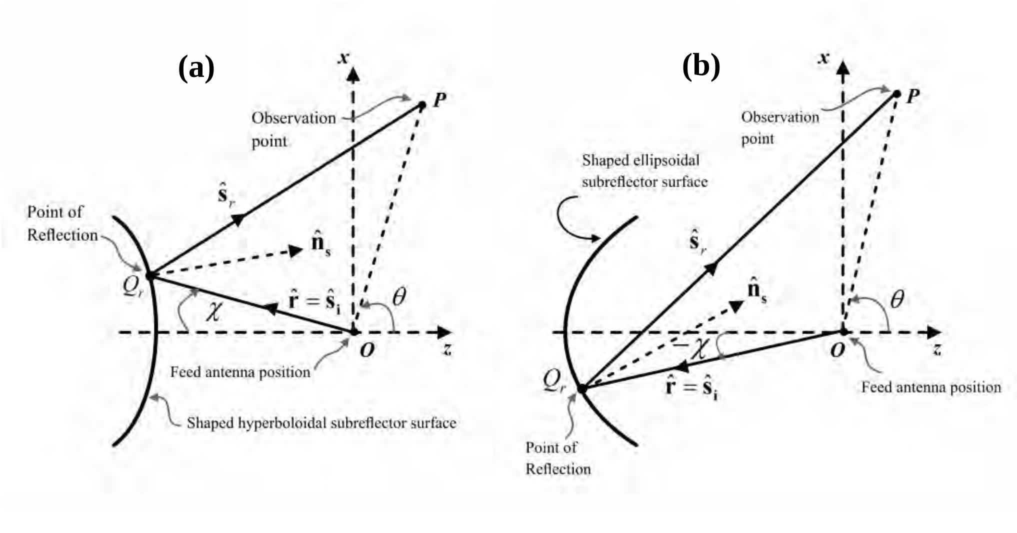

Fig. 5.3: GO vectors used for reflected field formulations: (a) shaped hyperboloidal subreflector, (b) shaped ellipsoidal subreflector.

The point of reflection Q_r must be determined to calculate the fields. The position of Q_r depends on the position of P and the reflecting surface. It can be determined from the law of reflection [16]:

$$\hat{\mathbf{n}}_\mathbf{s} \cdot \hat{\mathbf{s}}_\mathbf{i} = -\hat{\mathbf{n}}_\mathbf{s} \cdot \hat{\mathbf{s}}_\mathbf{r} \; . \tag{5.4}$$

For a given P and Q_r, the vectors $\hat{\mathbf{s}}_\mathbf{i}$ and $\hat{\mathbf{s}}_\mathbf{r}$ can be calculated from equations derived in Section 3.7. The point on the subreflector surface that satisfies (5.4) for a given P, is the required Q_r for that P. Equation (5.4) is a nonlinear equation, which can be easily solved using any suitable numerical methods. For unshaped hyperboloidal or ellipsoidal subreflectors, only one Q_r is possible for one P location. However, for some shaped surfaces, multiple values of Q_r is possible for a given P. This must be noted while solving (5.4). The length parameter s_r is the distance between P and Q_r. It can easily be calculated from the co-ordinates of the points.

The only parameters of (5.2) that haven't been formulated yet are ρ_{1r} and ρ_{2r}. There are multiple methods of formulating the radii of curvature. A method which is especially suitable antenna applications is used here. For an axially symmetric reflecting surfaces (like the shaped hyperboloidal or shaped ellipsoidal subreflectors), the radii of curvature can be expressed as:

$$\rho_{1r} = \rho_{2r} = \frac{m_s}{M_s} \ . \tag{5.5}$$

Where,

$$\left.\begin{aligned} m_s &= \left(\frac{\partial \mathbf{r}}{\partial \phi_s}\right) \cdot \left(\frac{\partial \hat{\mathbf{s}}_\mathbf{r}}{\partial \phi_s}\right) \\ M_s &= \left(\frac{\partial \hat{\mathbf{s}}_\mathbf{r}}{\partial \phi_s}\right) \cdot \left(\frac{\partial \hat{\mathbf{s}}_\mathbf{r}}{\partial \phi_s}\right) \end{aligned}\right\} \ . \tag{5.6}$$

The parameter ϕ_s and the vector $\mathbf{r}$ are defined in Section 3.6.1 and Section 3.6.2.

Using the derived equations, the scattered field from an unshaped hyperboloidal subreflector and an unshaped ellipsoidal subreflector is calculated. The results are shown in Fig. 5.4. The geometrical parameters used for the analysis is described in Chapter 3. From Fig. 5.4, it can be observed that the reflected field falls sharply at the RSB. The RSB for the unshaped Cassegrain geometry is 87.1345° and for the unshaped Gregorian geometry is 71.532°. The discontinuity of the reflected field past the RSB is expected. However, the total scattered field will not be discontinuous, as the diffracted field is not discontinuous around RSB. This fact will be shown in the following sections.

Although results are shown for unshaped surfaces, general equations of the shaped surfaces are used for calculations. Setting the distortion parameter τ_1 and τ_2 to zero gives

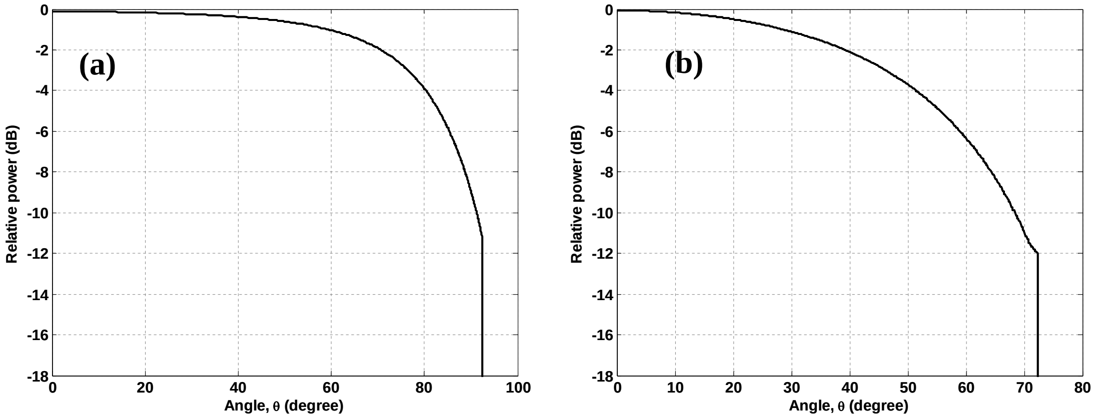

Fig. 5.4: Normalized reflected field from the (a) hyperboloidal subreflector, (b) ellipsoidal subreflector.

an unshaped surface. The optimum value of the distortion parameters are selected in the Chapter 6. The scattered field for the shaped subreflectors will be covered in that chapter.

5.5 Diffracted Fields

Complete formulation of the scattered field requires the formulation of the diffracted fields. Diffracted fields originate mostly from the edge of the reflecting surface. In this section, diffraction points will be identified. UTD diffraction coefficients, transition and function will be calculated. Finally, the overall diffracted field will be formulated.

5.5.1 Diffraction points

For an axially symmetric reflecting surface with the feed located on the axis at a finite distance for the surface, only two single edge-diffracted rays are possible for an observation point [28]. The rays emit from the two edges in the *xz* plane view of the subreflector. The edge points are arbitrarily termed as Q_{ep} and Q_{en}. The points as Q_{ep} and Q_{en} along with the diffracted rays are shown in Fig. 5.5 and Fig. 5.6. An incident ray at a single point on the reflecting surface results in only one reflected ray; but an incident ray on an edge point creates infinite number of diffracted rays which occupy *Keller's diffraction cone* [16]. However, at an arbitrary observation point, there is only one diffracted ray from each diffraction point. So, the total diffracted field at point P is the vector summation of the two edge diffracted fields from Q_{ep} and Q_{en}.

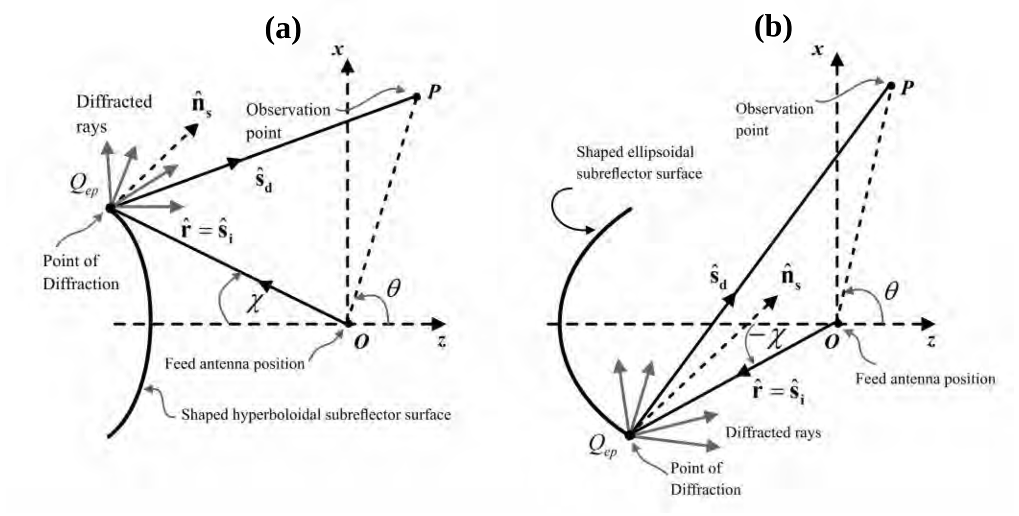

Fig. 5.5: Edge diffracted rays from point Q_{ep} for (a) shaped hyperboloidal subreflector, (b) shaped ellipsoidal subreflector.

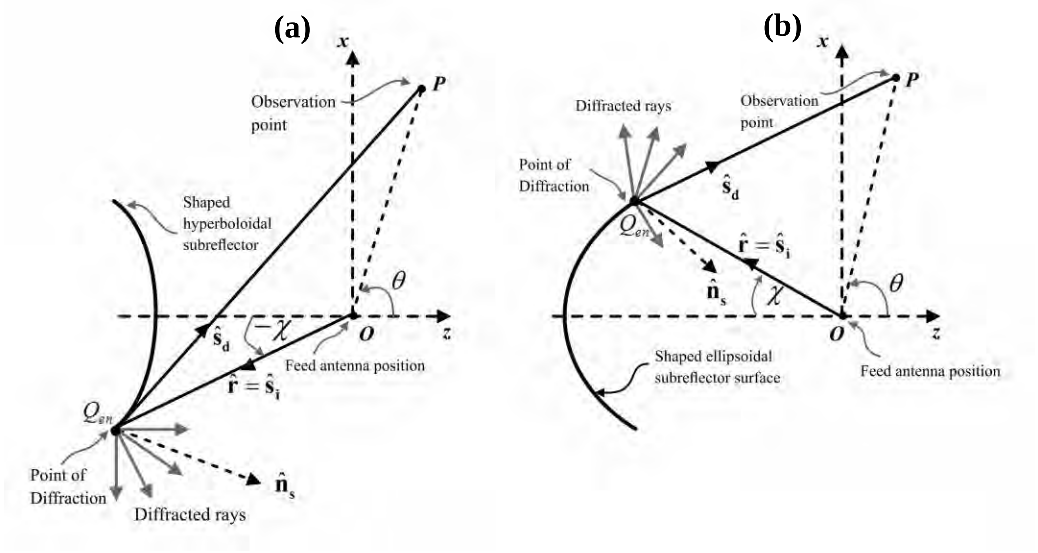

Fig. 5.6: Edge diffracted rays from the point Q_{en} for (a) shaped hyperboloidal subreflector, (b) shaped ellipsoidal subreflector.

5.5.2 UTD edge diffraction coefficients

Diffracted fields are characterized by diffraction coefficients. The three dimensional diffraction coefficients are given by:

$$\left.\begin{array}{l} D_s = D_1 + D_2 - (D_3 + D_4) \\ D_h = D_1 + D_2 + (D_3 + D_4) \end{array}\right\} . \tag{5.7}$$

Here, D_s and D_h are the soft and hard diffraction coefficient [28]. The components of the diffraction coefficients are given by the following equations:

$$D_1 = \frac{-\exp(-j\pi/4)}{2n\sqrt{2\pi k}\sin\beta_0}\cot\left[\frac{\pi+(\phi_d-\phi_i)}{2n}\right]F\left[kL_i a_+(\phi_d-\phi_i)\right], \tag{5.8}$$

$$D_2 = \frac{-\exp(-j\pi/4)}{2n\sqrt{2\pi k}\sin\beta_0}\cot\left[\frac{\pi-(\phi_d-\phi_i)}{2n}\right]F\left[kL_i a_-(\phi_d-\phi_i)\right], \tag{5.9}$$

$$D_3 = \frac{-\exp(-j\pi/4)}{2n\sqrt{2\pi k}\sin\beta_0}\cot\left[\frac{\pi+(\phi_d+\phi_i)}{2n}\right]F\left[kL_{rn} a_+(\phi_d+\phi_i)\right], \tag{5.10}$$

$$D_4 = \frac{-\exp(-j\pi/4)}{2n\sqrt{2\pi k}\sin\beta_0}\cot\left[\frac{\pi-(\phi_d+\phi_i)}{2n}\right]F\left[kL_{ro} a_-(\phi_d+\phi_i)\right]. \tag{5.11}$$

The angles ϕ_i and ϕ_d are angles of the incident and diffracted rays measured from the tangent line at the diffraction point. The angles are shown in Fig. 5.7.

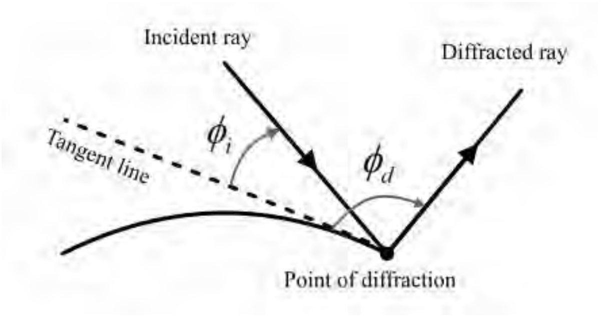

Fig. 5.7: Diffraction angle defined at the point of diffraction.

Equation (5.8) – (5.14) contains multiple parameters. Each parameter needs to be defined. The angle β_0 is the diffraction cone half-angle, which is 90° for the shaped circularly symmetric subreflectors having the geometric propertied discussed in Chapter 3 [16]. The parameter n has a value of 2 when the both faces of the reflecting surface have the same curvature [16]. This assumption is made through out this thesis and therefore, $n = 2$ is used. *F(.)* is the *transition function* that will be discussed in detail in the following Sections.

L_i, L_{ro}, and L_{rn} are *distant parameters* associated with the incident shadow boundary and reflection shadow boundaries. The *o* and *n* subscripts refer to the two faces or the reflecting surface. The faces are shown in Fig. 5.8. The labeling of *o* and *n* is completely arbitrary. The faces can be identical or different as depicted in Fig. 6.8. It is assumed throughout this thesis that the two faces are identical. So, the *o* and *n* subscripts are equivalent.

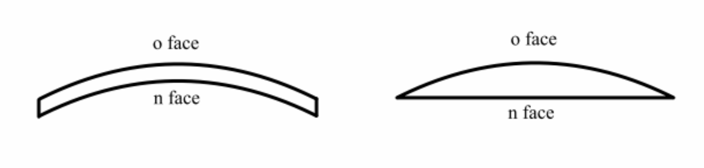

Fig. 5.8: o face and n face of the reflecting surfaces (identical faces on the left and non-identical faces on the right).

The distant parameter L_i can be expressed by the following equation for a spherical incident field wave front:

$$L_i = \frac{s_d s_i}{s_d + s_i} \sin^2(\beta_0) \ . \tag{5.12}$$

s_d is the distance from the diffraction point to observation point, and s_i is the distance from the feed antenna to the diffraction point. The distant parameters L_{ro} and L_{rn} can be expressed for discussed case as [16]:

$$L_{ro} = L_{rn} = \frac{s_d(\rho_{er} + s_d)\rho_{1r}\rho_{2r}}{\rho_{er}(\rho_{1r} + s_d)(\rho_{2r} + s_d)} \sin^2(\beta_0) \ . \tag{5.13}$$

Where,

$$\rho_{er} = \left\{ \frac{1}{s_i} - \frac{2(\hat{\mathbf{n}}_\mathbf{e} \cdot \hat{\mathbf{n}}_\mathbf{s})(\hat{\mathbf{s}}_\mathbf{i} \cdot \hat{\mathbf{n}}_\mathbf{s})}{a_e \sin^2(\beta_0)} \right\}^{-1} \ . \tag{5.14}$$

Here, $\hat{\mathbf{n}}_\mathbf{e}$ is vector normal to the edge and depends on the shape of the reflecting surfaces and the position of the diffraction point [16]. The radii of curvature ρ_{1r} and ρ_{2r} have been defined in (5.5). Alternate expressions of these quantities also exist. The term a_e is the radius of curvature of the reflecting surface at the diffraction point. It can be numerically evaluated by taking two points $P_1(x_e, z_e)$ and $P_2(x_e+\Delta x_e, z_e + \Delta x_e)$ close to the diffraction point and using the following equation:

$$a_e = \frac{\sqrt{(\Delta x_e)^2 + (\Delta z_e)^2}}{\cos^{-1}(\hat{\mathbf{n}}_\mathbf{s1} \cdot \hat{\mathbf{n}}_\mathbf{s2})} \ . \tag{5.15}$$

Here, $\hat{\mathbf{n}}_\mathbf{s1}$ and $\hat{\mathbf{n}}_{\mathbf{s}2}$ are normals on the surface at P_1 and P_2. The equation can be derived from the definition of radius of curvature [25].

The functions *a*₊*(.)* and *a*₋*(.)* are defined as:

$$\left.\begin{aligned} a_{+}(\gamma) &= 2\cos^2\left(\frac{2n\pi N_{+}-\gamma}{2}\right) \\ a_{-}(\gamma) &= 2\cos^2\left(\frac{2n\pi N_{-}-\gamma}{2}\right) \end{aligned}\right\} . \tag{5.16}$$

Where, N_+ and N_- are integers that most nearly satisfy:

$$\left.\begin{aligned} 2n\pi N_{+}-\gamma &= \pi \\ 2n\pi N_{-}-\gamma &= -\pi \end{aligned}\right\} . \tag{5.17}$$

Using (5.7) – (5.17), the diffraction coefficients can be calculated.

5.5.3 The transition function

Keller’s original GTD became unbounded in the shadow boundaries [16]. The problem was solved in UTD by introducing the transition function, *F(.)*, in the diffraction coefficients. The transition function used in the UTD diffraction coefficients keep the diffracted field value bounded. The transition function is expressed as:

$$F(x) = 2j\sqrt{x}\exp(jx)\int_{\sqrt{x}}^{\infty}\exp(-ju^2)\,du \ . \tag{5.18}$$

The integral part of the transition function resembles a Fresnel integral [20]. The function can be evaluated numerically. However, if the function can be converted to a standard integral, computer routines for evaluating the function will be easier. *F(.)* can be expressed in terms of the *incomplete gamma function*, *Γ(.)*,which is defined as:

$$\Gamma(v,x) = \int_{x}^{\infty}\exp(-t)t^{v-1}\,dt \ . \tag{5.19}$$

By reorganizing (5.18) in the form of (5.19), *F(.)* can be expressed as:

$$F(x) = \sqrt{jx}\exp(jx)\Gamma\left(\frac{1}{2}, jx\right) . \tag{5.20}$$

In the ISB and RSB region, the arguments of *F(.)* in (5.8) – (5.11) have small values. The cotangent functions become very large in ISB and RSB region. Therefore, *F(.)* must have small values to compensate the overall value of the diffraction coefficient. In other regions, the effect of *F(.)* should be negligible. The transition function fulfills these requirements. It can be observed from the magnitude and phase plot of F(.) as shown in Fig. 5.9.

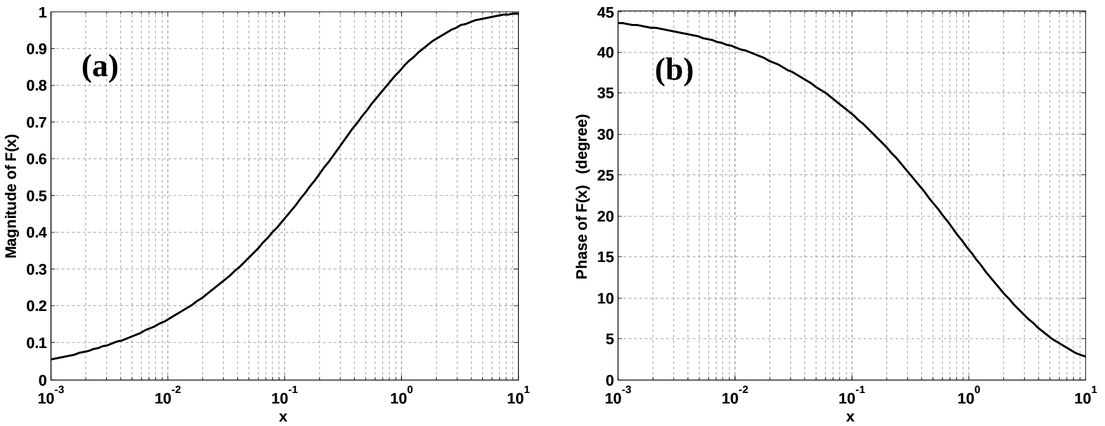

Fig. 5.9: Characteristics of the transition function (a) magnitude plot, (b) phase plot.

5.5.4 Diffracted field formulation

The diffracted fields can be formulated using the following equation:

$$\begin{bmatrix} E_{d,\beta_d} \\ E_{d,\phi_d} \end{bmatrix} = \begin{bmatrix} -D_s & 0 \\ 0 & -D_h \end{bmatrix} \cdot \begin{bmatrix} E_{i,\beta_i}\left(Q_e\right) \\ E_{i,\phi_i}\left(Q_e\right) \end{bmatrix} \sqrt{\frac{\rho_d}{s_d(s_d+\rho_d)}}\exp(-jks_d) \ . \qquad (5.21)$$

Here, E_{d,β_d} and E_{d,ϕ_d} are the components of the diffracted field expressed in the edge fixed co-ordinate system [16]. Similarly, E_{i,β_i} and E_{i,ϕ_i} are the components of the incident field expressed in the edge fixed co-ordinate system and evaluated at the diffraction point Q_e. Any arbitrary polarized wave can be resolved into edge fixed component using:

$$\left.\begin{aligned} \mathbf{E_i} &= \left(\mathbf{E_i}\cdot\hat{\boldsymbol{\beta}}_{\mathbf{i}}\right)\hat{\boldsymbol{\beta}}_{\mathbf{i}} + \left(\mathbf{E_i}\cdot\hat{\phi}_i\right)\hat{\phi}_i \\ \mathbf{E_d} &= \left(\mathbf{E_d}\cdot\hat{\boldsymbol{\beta}}_{\mathbf{d}}\right)\hat{\boldsymbol{\beta}}_{\mathbf{d}} + \left(\mathbf{E_d}\cdot\hat{\boldsymbol{\phi}}_{\mathbf{d}}\right)\hat{\boldsymbol{\phi}}_{\mathbf{d}} \end{aligned}\right\} . \qquad (5.22)$$

The edge fixed co-ordinate vectors depend on the geometry of the surface and the position of the diffraction point. They can be easily formulated from the set of equations provided in [16] and therefore is not repeated here.

The term ρ_d of (5.21) can be evaluated using:

$$\rho_d = \left\{\frac{1}{s_i} - \frac{\hat{\mathbf{n}}_{\mathbf{e}}\cdot\left(\hat{\mathbf{s}}_{\mathbf{i}} - \hat{\mathbf{s}}_{\mathbf{d}}\right)}{\left|a_e\right|\sin^2\left(\beta_0\right)}\right\}^{-1} \ . \qquad (5.23)$$

Using (5.21) along with the other derived equations, the diffracted field at an observation point for a given diffraction point at Q_e. The diffracted field for both Q_{ep}

and Q_{en} points are formulated separately and vector sum is performed to find the total diffracted field. The diffracted fields for the unshaped hyperboloidal subreflector and the unshaped ellipsoidal subreflector are shown in Fig. 5.10. The diffracted fields are normalized with respect to the maximum value of the reflected field. It can be observed that the diffracted fields have maximum value near the RSB which is located at 87.1345° for the unshaped Cassegrain geometry and at 71.532° for the unshaped Gregorian geometry. The oscillatory nature of the diffracted field is due to the fact that it is a vector summation of two edge diffracted rays. The phase mismatch between these rays causes the oscillation. Near the RSB, the effect of one edge ray is much larger than the other, causing the oscillation amplitude to decrease.

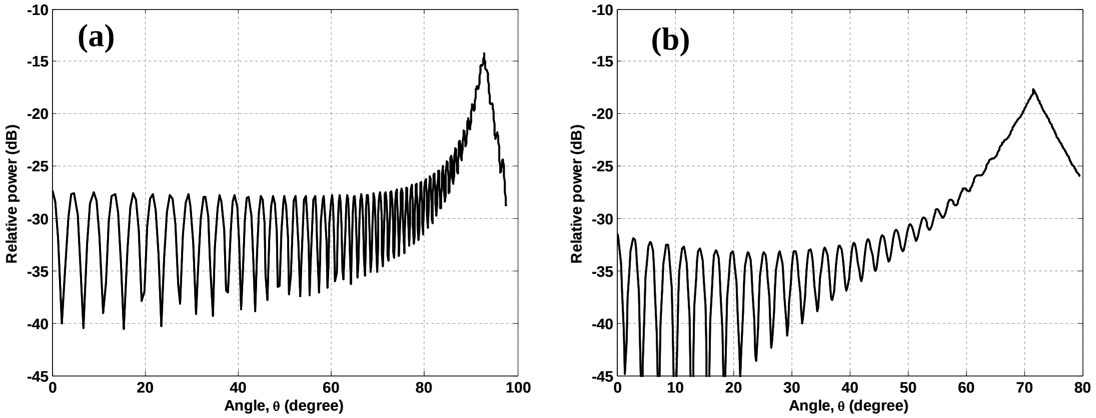

Fig. 5.10: Diffracted field for the (a) hyperboloidal subreflector,
(b) ellipsoidal subreflector.

5.6 Total Scattered Field

The total scattered field is calculated using the vector summation of the reflected and scattered field. The incident field component at the observation region is neglected it. This is because of the fact that the observation region is defined on the main reflector surface. In the dual reflector geometries, the main reflector is located behind the feed antenna. Since a horn antenna is used as the feed, the radiated field of the horn at angles near 180° from its axis is expected to be very small. So, neglecting the feed field at observation region will have no significant affect on accuracy of the results.

The total scattered field can be expressed as:

$$\mathbf{E_s} = \mathbf{E_r} + \mathbf{E_d} \ . \tag{5.24}$$

The reflected field is zero past the RSB, and the total scatted field is the diffracted field only. The diffracted field has non-zero values everywhere. The total scattered field for the unshaped Cassegrain and Gregorian geometry is shown in Fig. 5.11 and Fig. 5.12.

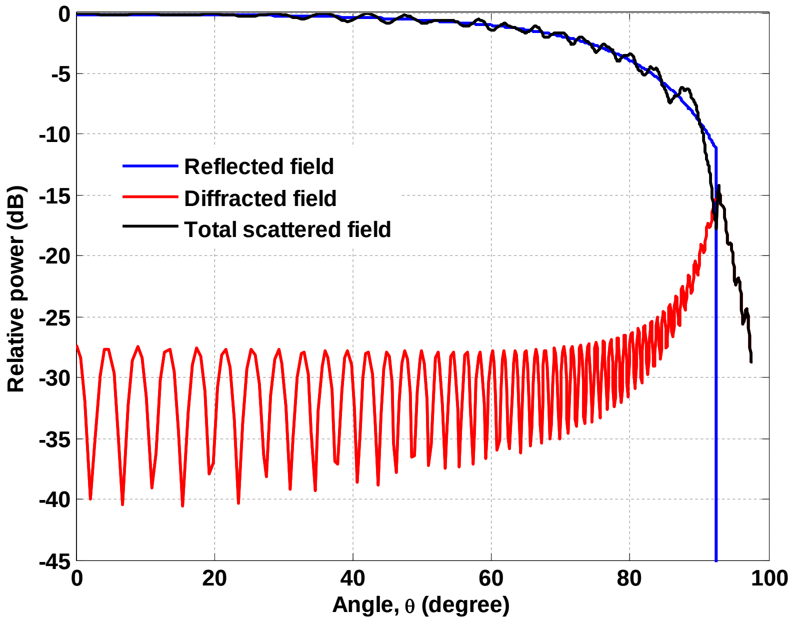

Fig. 5.11: Total scattered field from the unshaped hyperboloidal subreflector.

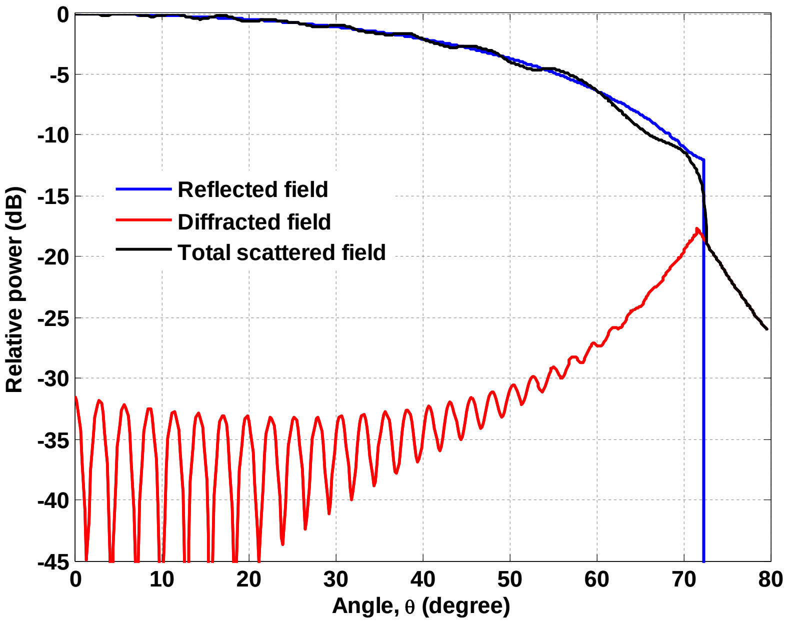

Fig. 5.12: Total scattered field from the unshaped ellipsoidal subreflector.

It can be observed that the total scattered field is continuous through out the observation region. Thus the UTD calculation is accurate.

Similar calculations will be performed for the shaped geometries. Appropriate values of the distortion parameters are required to define the required shaped surfaces. These values will be calculated in Chapter 6. The scattered field from the shaped surfaces will be discussed in that chapter, after the distortion parameter values are selected.

5.7 Conclusion

The fields scattered from the subreflector have formulated in this chapter. The reflected fields and the diffracted fields are formulated separately. Vector addition is performed to find the total scattered field. Numerical results are shown for unshaped hyperboloidal and unshaped ellipsoidal subreflectors. The results for the shaped surfaces will be discussed in Chapter 6 after optimized subreflector surfaces are defined.

CHAPTER 6

OPTIMIZATION USING DIFFERENTIAL EVOLUTION

6.1 Introduction

Optimization refers to finding values of a set of design parameters that give the best possible results. Optimization is a key step for many design problems. For shaped dual reflector antennas, the shape of the reflectors must be optimized to satisfy certain design requirements. As discussed in Chapter 3, the shapes of the reflector surfaces are determined by the value of the distortion parameters. Optimum value of these parameters must be determined. The complex relationship between the distortion parameters and radiation characteristics of the antenna is not apparent. Due to the lack of a direct relation, differentiation based optimization approach can not be easily applied. So, a search based optimization algorithm is expected to be suitable to find the optimum values of the parameters. Differential evolution (DE) algorithm is used in this thesis for optimizing the parameters.

In this chapter, a brief discussing on DE algorithm is given. It is followed by the formulation of the cost function for the current problem. Next, two different optimization is performed for the shaped Cassegrain geometry for two different goals. The performance of the optimized design is compared with that of the unshaped geometry. The same steps are repeated for the shaped Gregorian geometry.

6.2 Differential Evolution Algorithm

DE is a stochastic global optimization algorithm. The algorithm was first proposed by Storn and Price in 1997 [15]. Since then, DE has been used successfully in many engineering applications including electromagnetics [29], [30]. The algorithm has been proven to be highly robust. It also has a fast converging rate. DE is a search based approach, and therefore differentiation is not required. Other popular search based optimization algorithm includes: genetic algorithm (GA), particle swarm optimization (PSO), simulated annealing (SA) etc. These algorithms are well known and they have been used for many applications. Each algorithm has its advantages and disadvantages. DE algorithm often outperforms PSO, GA and other algorithms [29]. For this reason, DE is used in this thesis.

Since DE algorithm is covered in literature [15], [29], only a brief overview of the algorithm is presented here. The terminology used in the algorithm is discussed first. A potential solution of the optimization problem is represented by a vector. The *dimension, D,* of the vector is equal to the number of parameters that need to be optimized. So, for the reflector shaping problem discussed here, the dimension of the vectors will be 4, representing τ_1, τ_2, ζ_1, and ζ_2. The algorithm starts with a set of random vectors, which are potential solutions of the problem. The set of vectors is known as a *generation*. Each vector of a generation is known as a member of the *population*. The number of population in a generation is known as *population size, N_p*. The optimization problem can be evaluated for each population. An objective function must be defined that quantifies the quality of the solution of each population. This objective function is known as the *fitness function* or *cost function*. The fitness/cost function relates the problem with the algorithm. If the objective of the optimization algorithm is to minimize the objective function, then it is referred to as the *cost function*. For maximization problem, it is known as *fitness function*. Minimization procedure is assumed in this thesis. Therefore, the term cost function will be used from now on. The cost function takes a population as an input and gives a single numerical value as output. Each member of a population in a generation is associated with its *cost value* evaluated from the cost function. The lower the cost value, the better the population is suitable as a solution. The DE algorithm starts with an initial generation, and produces a new generation at each iterative step based on the population of the previous generation and their cost values. So, each generation represents an iterative step. The number of iteration is often limited by *maximum generation number, G_{max}*. After a significant number of generations, all the population converges to a single value representing the solution of the problem.

The DE algorithm is characterized by a set of equations. Let the i^{th} population of the G^{th} generation be represented by the vector $\mathbf{x_{i,G}}$. It can be expressed as:

$$\mathbf{x_{i,G}} = \left[x_{i,G}^{1} \quad x_{i,G}^{2} \cdots \; x_{i,G}^{D} \right] . \tag{6.1}$$

Here, i = 1, 2, … N_p and G = 1, 2, … G_{max}. For, the reflector shaping problem, D = 4, representing the 4 distortion parameters. For, each vector, a mutant vector, $\mathbf{v_{i,G+1}}$, is generated using:

$$\mathbf{v_{i,G+1}} = \mathbf{x_{r1,G}} + F_m \cdot \left(\mathbf{x_{r2,G}} - \mathbf{x_{r3,G}} \right) \ . \tag{6.2}$$

Here, r1, r2 and r3 are random indexes satisfying:

$$\left. \begin{array}{l} r1,\ r2,\ r3 \in \left\{ 1, 2, 3, \cdots N_p \right\} \\ r1 \neq r2 \neq r3 \neq i \end{array} \right\} . \tag{6.3}$$

F_m is known as *mutation scale factor*. A common value of $F_m = 0.9$ is used here [29].

A *trial vector*, $\mathbf{u_{i,G+1}}$ has the same dimension as the population and can be written as:

$$\mathbf{u_{i,G+1}} = \left[u_{i,G+1}^{1} \ \ u_{i,G+1}^{2} \ \cdots \ u_{i,G+1}^{D} \right] \ . \tag{6.4}$$

The trial vector is defined as:

$$u_{i,G+1}^{j} = \begin{cases} v_{i,G+1}^{j}, & \text{if } \mathrm{rand}_j \leq C_r \text{ or } j \ = \ \mathrm{rand}_i \\ x_{i,G}^{j}, & \text{if } \mathrm{rand}_j > C_r \text{ and } j \ \neq \ \mathrm{rand}_i \end{cases} . \tag{6.5}$$

Here, j = 1, 2, … ,D. The terms $rand_j$ and $rand_i$ are random numbers taken from an uniform distribution in the range 0 to 1, and they are evaluated every time j and i is varied respectively. C_r is the *crossover constant*. It is limited within 0 to 1. The commonly used value C_r = 0.9 is used here.

A new generation is defined from the following equation:

$$\mathbf{x_{i,G+1}} = \begin{cases} \mathbf{u_{i,G+1}}, & \text{if} \quad f_{\text{cost}}(\mathbf{u_{i,G+1}}) \leq f_{\text{cost}}(\mathbf{x_{i,G}}) \\ \mathbf{x_{i,G}}, & \text{if} \quad f_{\text{cost}}(\mathbf{u_{i,G+1}}) > f_{\text{cost}}(\mathbf{x_{i,G}}) \end{cases} . \tag{6.6}$$

Here, f_{cost} is the cost function. The first generation is selected randomly using a uniform random number generator. The next generations are formulated using (6.6) and corresponding equations.

A *solution space* needs to be defined initially. It defines the region over which optimum the values of the parameters will be searched. A valid range of optimized parameters can usually be obtained from observation. These values are used to define the solution space. To ensure that the algorithm is bounded within the solution space, the trail vector defined (6.5) is checked. If it falls outside the range, the vector is re-evaluated.

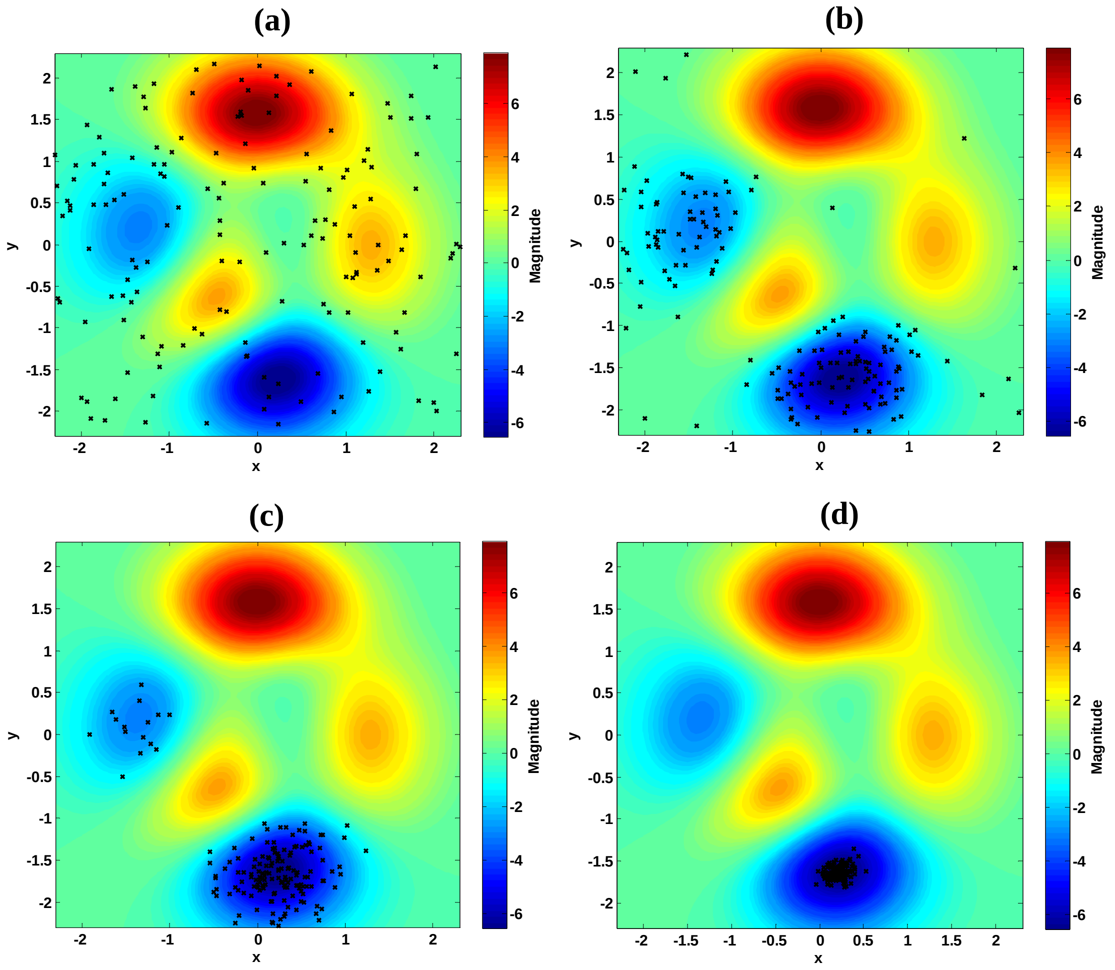
(a) (b) (c) (d)

Fig. 6.1: Positions of the population vectors at (a) initial stage, (b) 5th iteration, (c) 10th iteration, (d) 20th iteration.

The operation of the DE algorithm can be expressed using a numerical example. The two dimensional peaks function is used as the cost function. The function is given by:

$$\begin{aligned} f_{\cos t}(x,y) &= 3(1-x)^2 exp\left\{-x^2-(y+1)^2\right\} \\ &-10\left(\frac{x}{5}-x^3-y^5\right)exp(-x^2-y^2)-\frac{1}{3}exp\left\{-(x+1)^2-y^2\right\} \end{aligned} \qquad (6.7)$$

The solution space is defined with x = –2.3 to 2.3 and y = –2.3 to 2.3. The population size is taken to be 200. The position of the vectors at different iterative step is superimposed over the contour plot of the cost function over the solution space in Fig. 6.1. The positions of the vectors are denoted by black crosses. It can be seen that the initial random vectors move towards to minimum cost value regions (denoted by the blue region). Within 20 iterations, almost all the population vectors converge to the global minima.

A more detailed description of the DE algorithm along with its working principal can be found in [29].

6.3 Cost Function Formulation

The cost function depends on the objective of the optimization. For the optimizations performed in this thesis work, the main objective is to create a shaped dual reflector geometry with uniform field distribution over the main reflector and yet have a small spillover. Spillover is defined as the power that is scattered by the subreflector which is not intercepted by the main reflector. For numeric evaluation, spillover in terms of the maximum distance away from the main reflector edge where the reflected field component of the total scattered field exists. This region is defined as the *spill region*, x_{spill}.. The uniformity of the field distribution over the main reflector is numerically evaluated by computing the *edge taper* at main reflector. (level of the field at the edge of the main reflector compared to the maximum field on the main reflector). The cost function is defined as the weighted sum of the edge taper and the spill region. It is expressed as:

$$f_{\cos t}\left(\tau_1,\tau_2,\zeta_1,\zeta_2\right) = -T_{p,dB} + 10x_{spill} \quad . \tag{6.8}$$

Here, $T_{p,dB}$ is the edge taper on the main reflector expressed in dB. The parameter will have negative values. For uniform distribution, it will have zero value. So, low values of the cost function indicate a good solution of the optimization problem. To evaluate f_{cost}, the scattered field of the subreflector must be calculated for a set of distortion parameter (τ_1 , τ_2 , ζ_1 and ζ_2) values.

For each iterative step of the optimization, the cost function must be evaluated for every member of the population. Evaluation of the cost function should take as little computational time as possible for fast analysis. For this reason, only reflected field component is considered when evaluating the cost function. The computational time is reduced as the complex calculations of the diffracted fields are avoided. Once the optimum data is found, the total scattered field is taken into consideration for increasing accuracy.

6.4 Optimization of the Shaped Cassegrain Geometry

Using DE algorithm along with the defined cost function of (6.8), the shaped Cassegrain system can be optimized. Two separate optimization process is performed with two sets of different design goals. The optimization gives design of two distinct shaped Cassegrain reflector systems. The optimization processes are described in the following sections.

6.4.1 Optimization 1: uniform illumination over the aperture

The first optimization process is performed with the objective of creating a shaped dual reflector system (of Cassegrain geometry) to create a more uniform field distribution over the main reflector compared to the unshaped dual reflector system. Spillover is also required to be as less as possible. The cost function defined by (6.8) is used. The diameter of the main reflector is kept same for the unshaped and shaped system. The entire geometrical parameter set is given in Table 3.1. The parameters of the unshaped system are same as the shaped system except for the diameter of the subreflector.

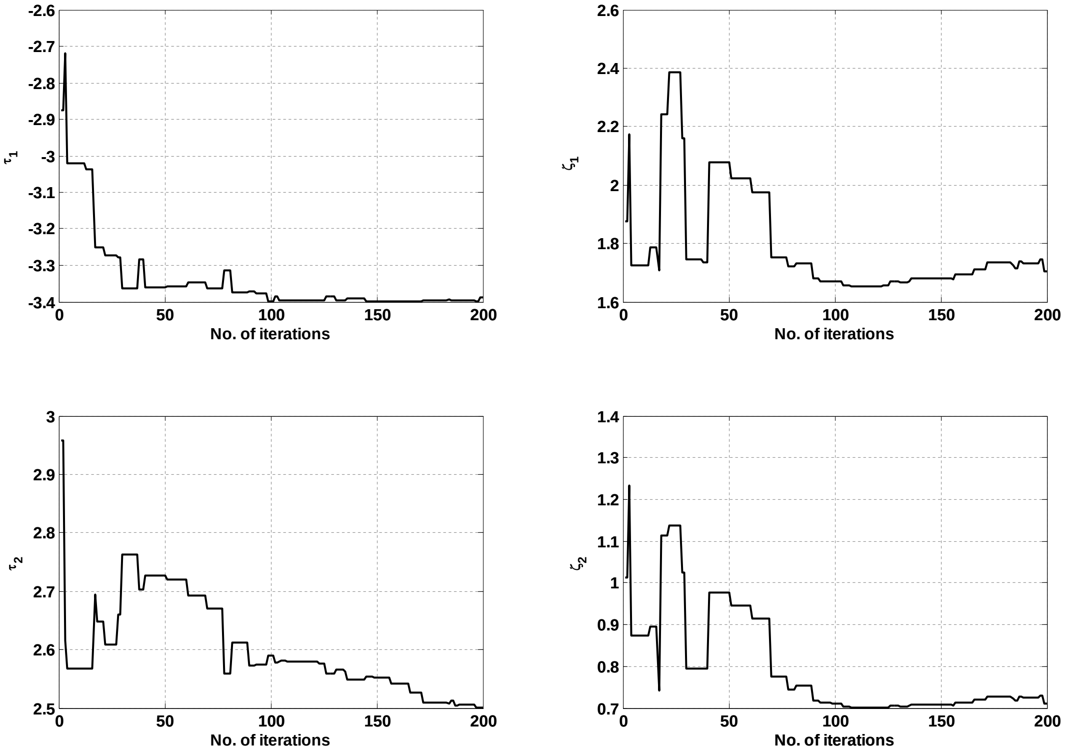

Fig. 6.2: Convergence of the distortion parameters during optimization 1 of the shaped Cassegrain system.

The diameter of the subreflector is increased to 1.7 m which was 1.25 m for the unshaped case. The additional length of the subreflector is expected to focus more energy towards the main reflector and decrease edge taper. The feed horn aperture diameter is decreased to 57 mm from 63 mm to provide similar edge taper on the extended subreflector. The other dimensions of the horn are the same as described in Table 4.1.

The DE algorithm is implemented with parameters N_p = 15, F_m = 0.9, C_r = 0.9, and G_{max} = 200. The solution space is defined by limiting τ_1 , τ_2 , ζ_1 and ζ_2 within (–3.4, –1), (2.5, 3.4), (1.5, 3.5), and (0.7, 1.3) respectively. The values are obtained from observation of multiple trial runs. The convergence of the distortion parameters with iteration is shown in Fig. 6.2. It can be seen that the 4 parameters becomes constant at iterations near 200, signifying convergence. The initial search of the solution space is depicted by the initial variations of the parameters during the first few iteration steps. The convergence can also be noted from the cost function values as shown in Fig. 6.3.

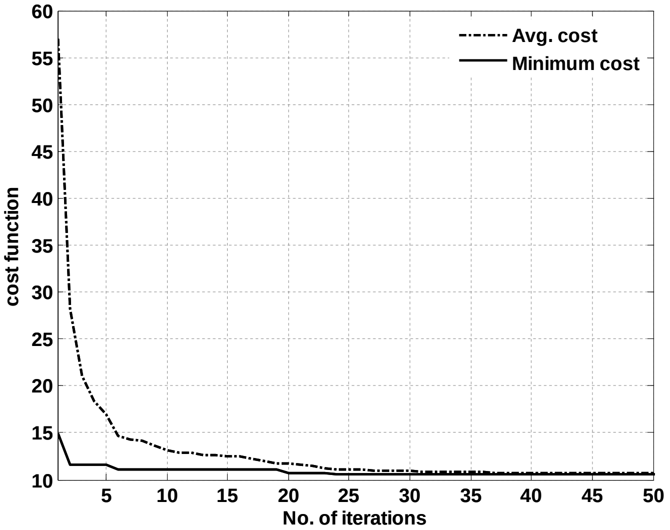

Fig. 6.3: Cost function value variation with iteration during optimization 1 of the shaped Cassegrain system.

The cost function value decreases with iteration, as the algorithm finds better solutions. Fig. 6.3 is truncated to 50 iterations, as the cost function becomes nearly flat after this region. This implies that the improvements in solution qualities after 50 iterations are not significantly high. The term average cost is defined as the average of the cost values of the entire population for a given generation (iteration). Minimum cost is defined as the lowest cost value found among the population for a given generation. The average cost coincides with the minimum cost as the algorithm converges.

The optimized value of distortion parameters is found to be: $\tau_1 = -3.3928$, $\tau_2 = 2.5015$, $\zeta_1 = 1.7212$ and $\zeta_2 = 0.7184$. The scattered field from the shaped hyperboloidal subreflector is shown in Fig. 6.4.

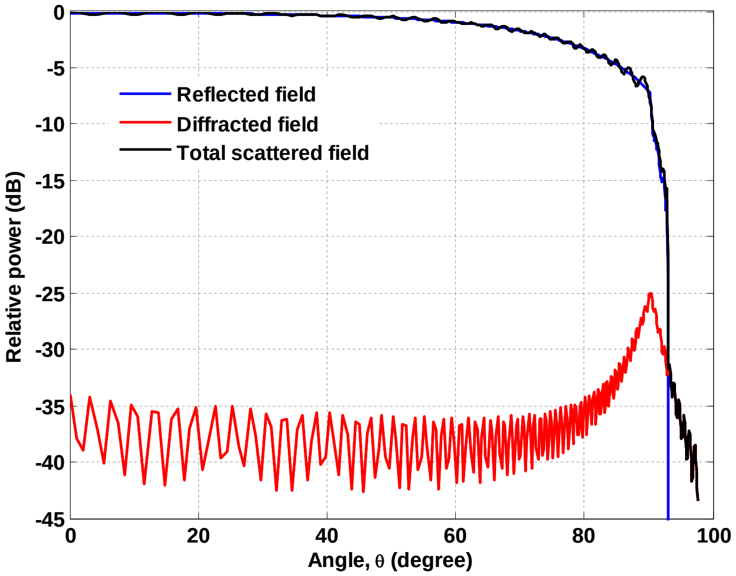

Fig. 6.4: Scattered field from the shaped hyperboloidal subreflector defined from optimization 1.

It can be seen that the total scattered field is very uniform and only tapers near the RSB (characterized by the zero value of the reflected field). The overall performance characteristics of the scattered field will be discussed in Section 6.6.

6.4.2 Optimization 2: reduction of main reflector size

The second optimization process concentrates on reducing the main reflector size. The goal is to reduce the antenna size without decreasing the gain of the antenna significantly. The gain of a reflector antenna is related to its size [21]. Decreasing main reflector diameter will decrease the gain, unless the distribution of the field over the main reflector has been made more uniform to compensate for the size reduction. The optimization process is performed with the objective of creating a shaped dual reflector system (of Cassegrain geometry) to create a significantly more uniform field distribution over the main reflector of a smaller size compared to the unshaped dual reflector system. Spillover is also required to be as less as possible. The cost function defined by (6.8) is again used.

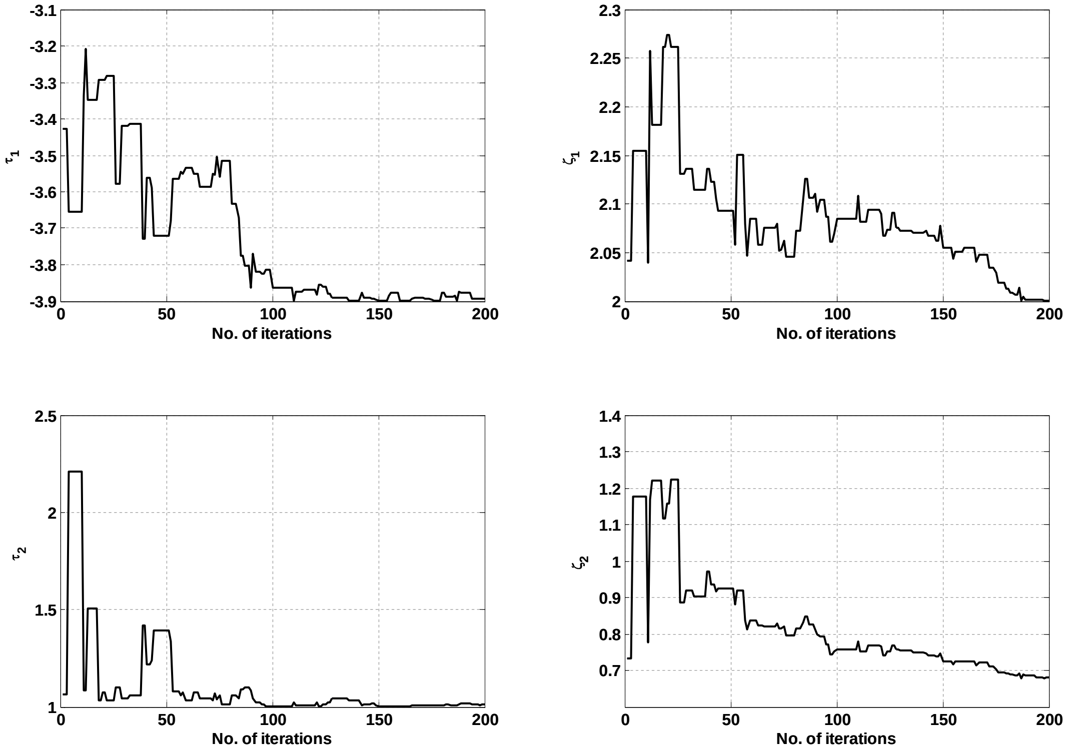

Fig. 6.5: Convergence of the distortion parameters during optimization 2 of the shaped Cassegrain system.

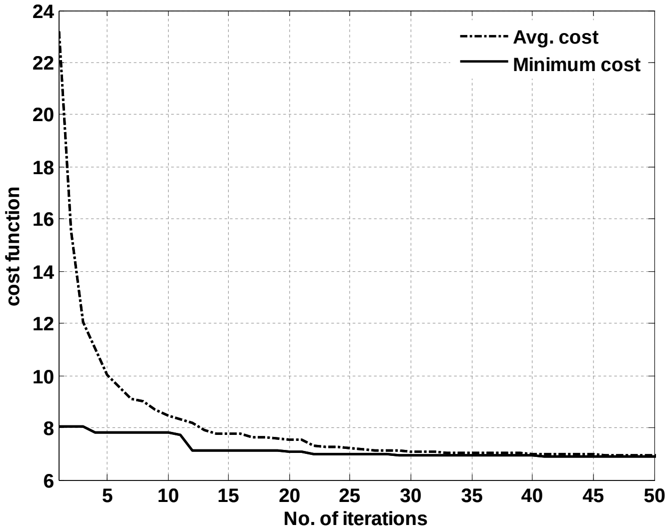

Fig. 6.6: Cost function value variation with iteration during optimization 2 of the shaped Cassegrain system.

The diameter of the subreflector is kept same for the unshaped and shaped system. The parameters of the unshaped system are same as the shaped system except for the diameter of the main reflector. The entire geometrical parameter set is given in Table 3.1. The main reflector diameter is decreased to 7.5 m from 10 m. The feed horn is kept identical. The geometry of the feed horn is defined in Table 4.1.

The DE algorithm is implemented with parameters N_p = 15, F_m = 0.9, C_r = 0.9, and G_{max} = 200. The solution space is defined by limiting τ_1 , τ_2 , ζ_1 and ζ_2 within (–3.9, –2.0), (1.0, 2.3), (2.0, 3.5), and (0.2, 1.3) respectively. The solution region is selected based on observation from multiple trial runs. The convergence of the distortion parameters with iteration is shown in Fig. 6.5. The cost function is shown in Fig. 6.6. The plots have typical shapes.

The optimized value of distortion parameters is found to be: τ_1 = – 3.8923, τ_2 = 1.0112, ζ_1 = 2.0005 and ζ_2 = 0.6803. The scattered field from the shaped hyperboloidal subreflector is shown in Fig. 6.7.

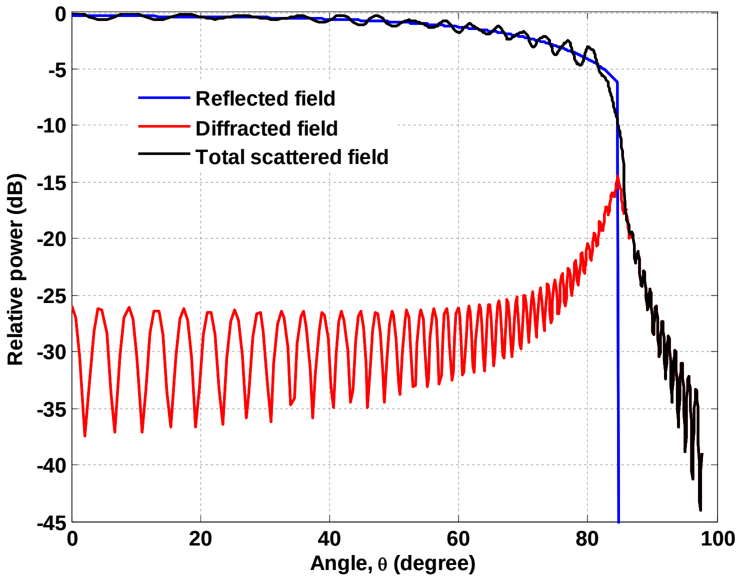

Fig. 6.7: Scattered field from the shaped hyperboloidal subreflector defined from optimization 2.

It can be observed from Fig. 6.7 that scattered field is very uniform and only tapers near the RSB (characterized by the zero value of the reflected field). The distribution is more uniform compared to results of optimization 1 as well. This is because of the fact that maintaining uniformity over a smaller aperture is relative easier. The overall performance characteristics of the scattered field will be discussed in Section 6.6.

6.5 Optimization of the Shaped Gregorian Geometry

The shaped Gregorian geometry can be optimized using the same procedure that was used for the shaped Cassegrain system. In this case, two separate optimization process is performed as well. They optimizations are characterized by two sets of different design goals. The optimization gives design of two distinct shaped Gregorian reflector systems. The optimization processes are described in the following sections.

6.5.1 Optimization 1: uniform illumination over the aperture

Like the first optimization process of the Cassegrain geometry, the first optimization here is performed with the objective of creating a shaped dual reflector system (of Gregorian geometry) to create a more uniform field distribution over the main reflector compared to the unshaped dual reflector system while maintaining low spillover. The cost function defined by (6.8) is used. The diameter of the main reflector is kept same

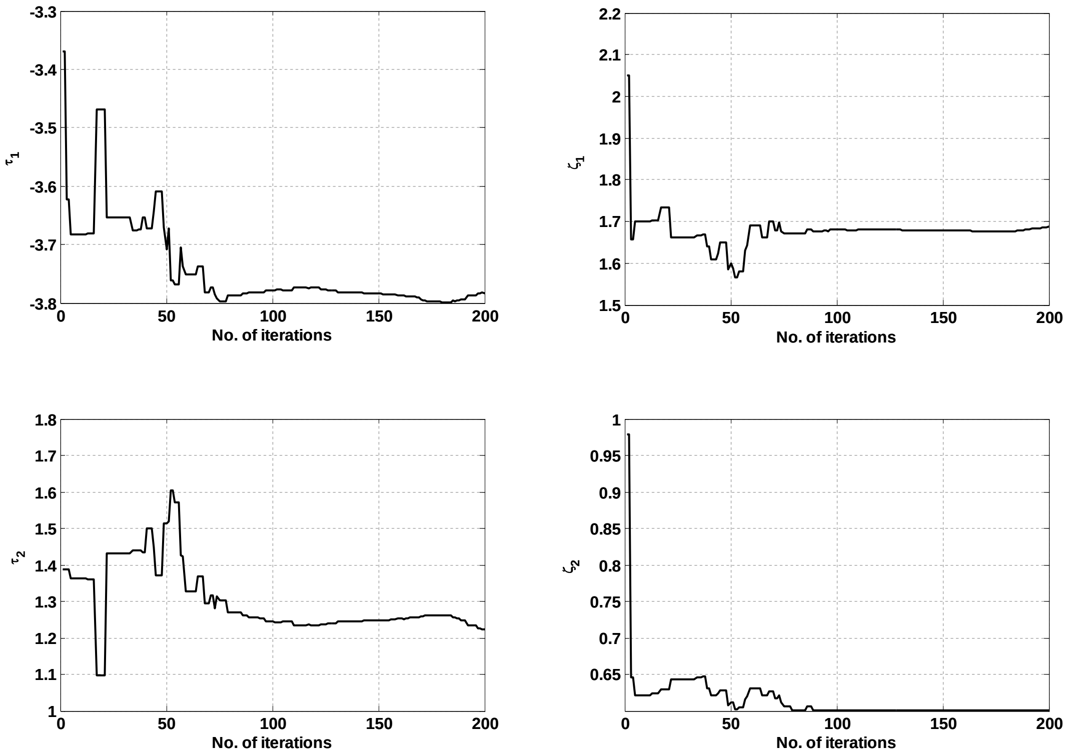

Fig. 6.8: Convergence of the distortion parameters during optimization 1 of the shaped Gregorian system.

for the unshaped and shaped system. The diameter of the shaped subreflector is taken to be 0.98 m whereas the subreflector diameter of the unshaped subreflector is 0.78 m. The rest of the geometrical parameters for both shaped and unshaped system are same and they are given in Table 3.1. The feed aperture diameter is taken to 65 mm for the shaped system and 69 mm for the unshaped system. The other parameters of the horn for both systems are identical and are shown in Table 4.1.

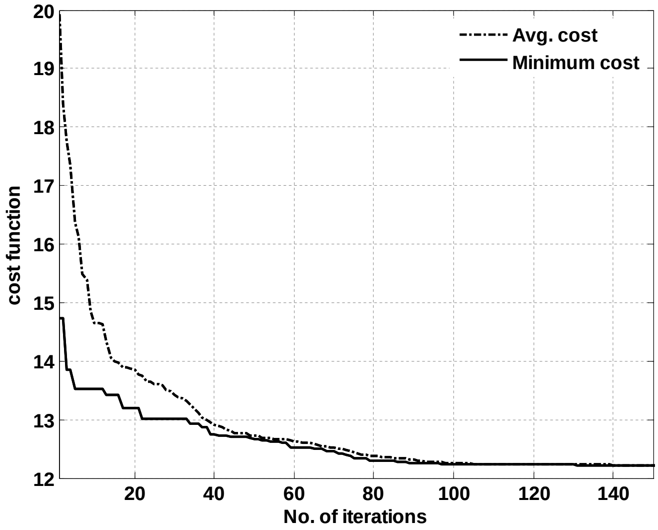

Fig. 6.9: Cost function value variation with iteration during optimization 1 of the shaped Gregorian system.

The DE algorithm is implemented with parameters N_p = 15, F_m = 0.9, C_r = 0.9, and G_{max} = 200. The solution space is defined by limiting τ_1 , τ_2 , ζ_1 and ζ_2 within (–3.8, –2.0), (1.0, 2.4), (1.5, 2.5), and (0.6, 1.1) respectively. The solution region is selected based on observation from multiple trial runs. The convergence of the distortion parameters with iteration is shown in Fig. 6.8. The cost function is shown in Fig. 6.9. The plots have typical shapes. It is noted that the cost function takes longer to converge for this optimization process compared to the optimization processes of the Cassegrain system.

The optimized value of distortion parameters is found to be: τ_1 = – 3.7836, τ_2 = 1.2241, ζ_1 = 1.6870 and ζ_2 = 0.6001. The scattered field from the shaped ellipsoidal subreflector is shown in Fig. 6.10. It can be observed from Fig. 6.10 that scattered field is uniform and tapers near the RSB (characterized by the zero value of the reflected field). The overall performance characteristics of the scattered field will be discussed in Section 6.6.

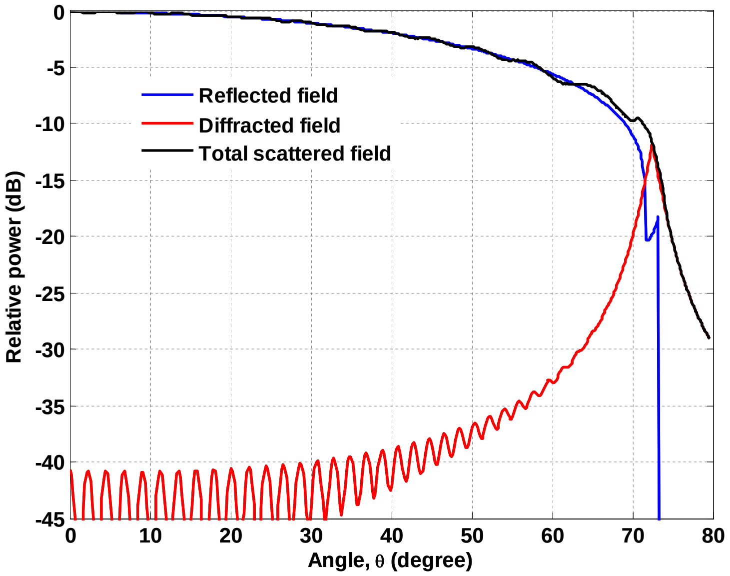

Fig. 6.10: Scattered field from the shaped ellipsoidal subreflector defined from optimization 1.

6.5.2 Optimization 2: reduction of main reflector size

The second optimization process of the Gregorian system is similar to the second optimization performed for the Cassegrain system. It concentrates on reducing the main reflector size. The goal is to reduce the antenna size without decreasing the gain of the antenna significantly. The optimization process is performed with the objective of creating a shaped dual reflector system (of Gregorian geometry) to create a significantly more uniform field distribution over the main reflector of a smaller size compared to the unshaped dual reflector system. Spillover is also required to be as less as possible. So, the cost function defined by (6.8) is again used.

The diameter of the subreflector is kept same for the unshaped and shaped system. The parameters of the unshaped system are same as the shaped system except for the diameter of the main reflector. The entire geometrical parameter set is given in Table 3.1. The main reflector diameter is decreased to 7.5 m from 10 m. The feed horn is kept identical. The geometry of the feed horn is defined in Table 4.1.

The DE algorithm is implemented with parameters N_p = 15, F_m = 0.9, C_r = 0.9, and G_{max} = 200. The solution space is defined by limiting τ_1 , τ_2 , ζ_1 and ζ_2 within (–4.2, –2.0), (1.0, 2.4), (1.5, 2.5), and (0.6, 1.1) respectively. Like previous cases, the solution region is selected based on observation from multiple trial runs. The convergence of the distortion parameters with iteration is shown in Fig. 6.11. The cost function is shown in

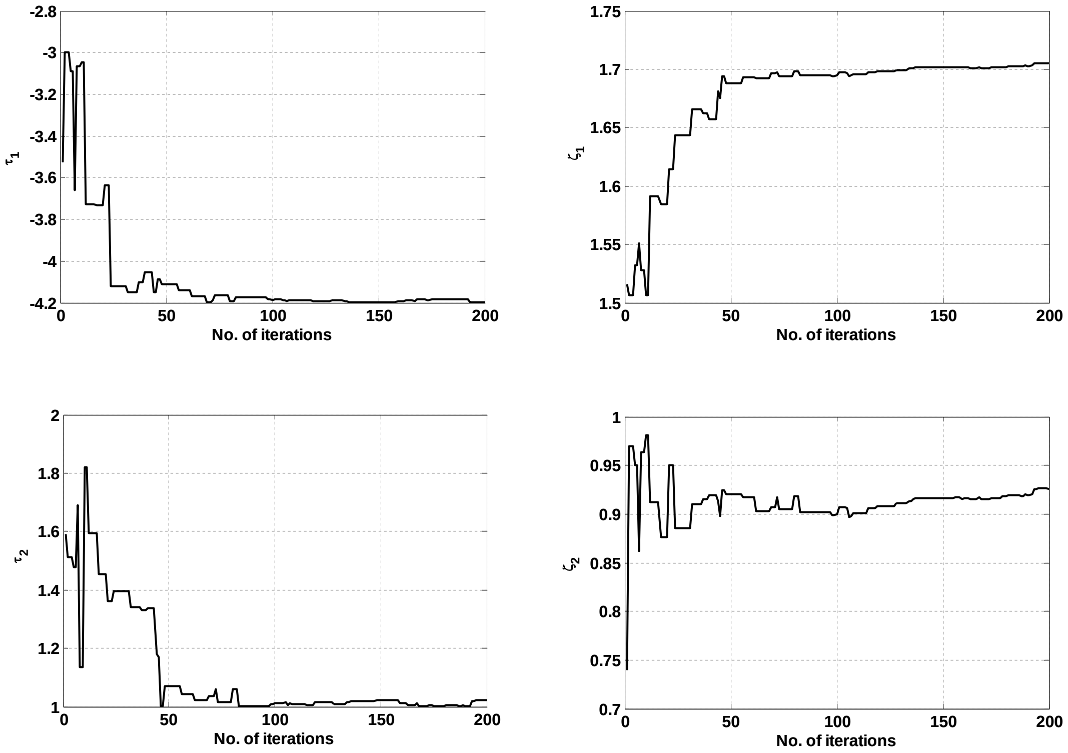

Fig. 6.11: Convergence of the distortion parameters during optimization 2 of the shaped Gregorian system.

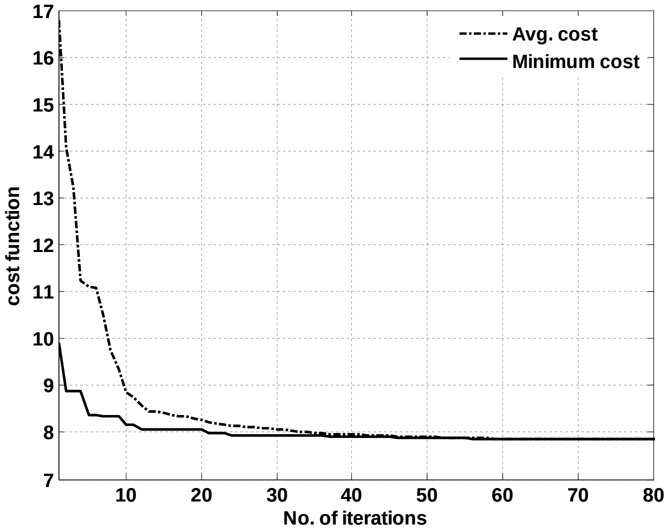

Fig. 6.12: Cost function value variation with iteration during optimization 2 of the shaped Gregorian system.

Fig. 6.12. The plots have typical shapes. The optimized value of distortion parameters is found to be: $\tau_1 = -4.1986$, $\tau_2 = 1.0213$, $\zeta_1 = 1.7049$ and $\zeta_2 = 0.9257$.

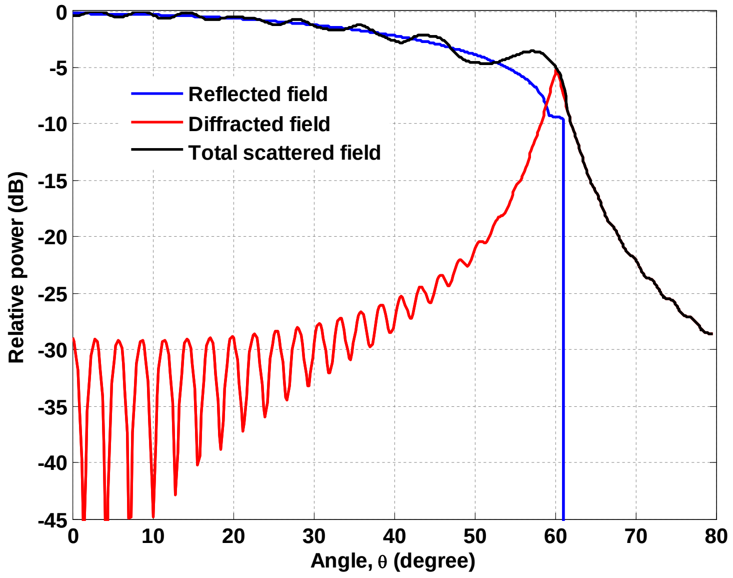

Fig. 6.13: Scattered field from the shaped ellipsoidal subreflector defined from optimization 2.

The scattered field from the shaped ellipsoidal subreflector is shown in Fig. 6.13. It can be observed from Fig. 6.10 that scattered field is uniform until the RSB (characterized by the zero value of the reflected field) in accordance with the design requirement. The overall performance characteristics of the scattered field will be discussed in Section 6.6.

6.6 Performance Evaluation of the Shaped Subreflectors

To evaluate the performance of the shaped reflectors, some performance parameters must be defined related to the scattered field characteristics. This scattered field from the main reflector will be discussed in Chapter 7. The scattered fields from the subreflectors have already been calculated and the results have been shown in Fig. 6.4, Fig. 6.7, Fig. 6.10 and Fig. 6.13. Performance parameters related to the scattered field from the subreflector is defined in this section.

The uniformity of the field distribution over the main reflector has been quantified using the edge taper parameter. Edge taper of the subreflector (T_s), and the edge taper of the main reflector (T_p) can be defined separately. The quantities are expressed as:

$$T_s = \frac{\text{Field intensity at the edge of the subreflector}}{\text{Maximum field intensity on the subreflector}} \ . \tag{6.9}$$

$$T_p = \frac{\text{Field intensity at the edge of the main reflector}}{\text{Maximum field intensity on the main reflector}} \ . \tag{6.10}$$

A more accurate estimation of uniformity can be described using the illumination efficiency parameter. It is defined by the following equation [3]:

$$\eta_{ill} = \frac{\left\{ \int\limits_{A_m} F_{dist}\left(r,\phi\right) dA_m \right\}^2}{\int\limits_{A_m} F_{dist}^2\left(r,\phi\right) dA_m} \ . \tag{6.11}$$

Here, $F_{dist}\left(r,\phi\right)$ field distribution over the aperture of the main reflector and A_m is the main reflector area. The integrations are performed over the entire surface of the main reflector. $F_{dist}\left(r,\phi\right)$ is calculated as the absolute value of the subreflector scattered field which is incident on the main reflector. So,

$$F_{dist}\left(r,\phi\right) = \left|\mathbf{E}_s\right| \ . \tag{6.12}$$

Another design requirement is low spillover. Spillover can occur when some of the feed field is not intercepted by the subreflector. It can also occur when some of the subreflector scattered field is not intercepted by the main reflector. The spillover efficiency can be defined for both these cases as:

$$\eta_{spill,f} = \frac{\text{Power incident on the subreflector surface}}{\text{Total power radiated by the feed}} \ . \tag{6.13}$$

$$\eta_{spill,s} = \frac{\text{Power incident on the main reflector surface}}{\text{Total power scattered by the subreflector}} \ . \tag{6.14}$$

For the optimized designs, these performance parameters are evaluated. The results are shown in Table 6.1 and Table 6.2. As the main reflector diameter and the subreflector diameter is different for each optimization, that information is also provided in the table. The rest of the geometrical parameters are constant and have already been shown in Table 3.1. They are not repeated here.

Table 6.1: Performance parameters of the optimized shaped hyperboloidal subreflectors.

Parameters	Cassegrain geometry		
	Unshaped	Opt. 1	Opt. 2
d_p	10 m	10 m	7.5 m
d_s	1.25 m	1.7 m	1.25 m
$T_{s,dB}$	–11.94 dB	–20.22 dB	–12.14 dB
$T_{m,dB}$	–14.76 dB	–17.41 dB	–12.75 dB
$\eta_{spill,f}$	97.05 %	99.40 %	97.10 %
$\eta_{spill,s}$	99.65 %	99.98 %	99.71 %
η_{ill}	85.87 %	87.92 %	92.82 %

Table 6.2: Performance parameters of the optimized shaped ellipsoidal subreflectors.

Parameters	Gregorian geometry		
	Unshaped	Opt. 1	Opt. 2
d_p	10 m	10 m	7.5 m
d_s	0.78 m	0.98 m	0.78 m
$T_{s,dB}$	–11.94 dB	–19.623 dB	–11.42 dB
$T_{m,dB}$	–13.19 dB	–10.40 dB	–4.45 dB
$\eta_{spill,f}$	97.06 %	99.38 %	96.44 %
$\eta_{spill,s}$	99.66 %	99.36 %	97.08 %
η_{ill}	85.68 %	90.44 %	97.37 %

From Table 6.1 and Table 6.2, it can be observed that the illumination efficiency has been significantly increased through optimization. Spillover efficiency related to subreflector scattered field have been kept at approximately same value. Feed spillover is also approximately unchanged. The uniform illumination is expected to decrease the beamwidth of the radiation pattern of the main reflector. This will be shown in the following chapters.

6.7 Conclusion

In this chapter, DE algorithm is used to optimize the shape of the dual reflector geometries. The optimization process has been implemented multiple times to create optimum shaped reflectors for different design goals. It has been shown that the DE algorithm performed well in terms of quick convergence. The performances of the shaped reflectors have been compared with that of unshaped reflectors. The performance parameters are defined for the subreflector scattered field. The main reflector scattered field will be calculated in the next chapter. It has been found that the optimization process produced shaped antennas that have more uniform field distribution over the main reflector without significantly affecting other parameters. This was one of the design criterions. So, the optimization process was successful.

CHAPTER 7

FORMULATION OF RADIATED FIELD FROM THE MAIN REFLECTOR

7.1 Introduction

The radiated field from the primary reflector (main reflector) is the output characteristics of a dual reflector antenna. The feed field and the subreflector scattered field are limited only within the dual reflector geometry. It is the primary reflector radiated field that connects the antenna to the outside. The feed design and the reflector shaping are performed to produce a desired radiated field. The far-field of the dual reflector antenna implies the radiated field from the main reflector. Most design requirements are enforced on the far-field characteristics of the antenna. So, formulation of the radiated field is essential.

In this chapter, the radiated field from the primary reflector is formulated. Physical optics (PO) method is used to formulate the field. The chapter starts with formulation of PO currents. The distribution of the PO currents on the main reflector surface due to the field scattered from the subreflector is calculated. Using the PO currents, the radiated field is formulated using the PO radiation integral.

7.2 PO Surface Currents

In PO method, the radiated field from a conducting body is determined using the surface current induced on the reflecting body due to an incident field [4]. The incident field on the main reflector is the subreflector scattered field, which have been calculated for the shaped and unshaped geometries in Chapter 5 and Chapter 6. In PO, it is assumed that the field incident on the reflecting body is a GO field [4]. As the GO field is zero in the shadow regions, the PO method assumes that current is zero in those regions. The PO surface current is approximated by the following equation [4], [16]:

$$\mathbf{J_{PO}} = \begin{cases} 2\hat{\mathbf{n}}_{\mathbf{p}} \times \mathbf{H_{inc}}, & \text{in the illuminated region} \\ 0, & \text{in the shadowed region} \end{cases} \quad . \tag{7.1}$$

Here, $\hat{\mathbf{n}}_{\mathbf{p}}$ is the unit normal vector pointed outwards from the reflecting surface, $\mathbf{H_{inc}}$ is the magnetic field incident on the reflecting surface and $\mathbf{J_{PO}}$ is the PO surface current density. The current density is referred to as *PO current density* because this is an approximation of the actual surface current density.

The incident magnetic field can be calculated from the electric field as:

$$\mathbf{H_{inc}} = Y\left(\hat{\mathbf{s}}_{\mathbf{ip}} \times \mathbf{E_{inc}}\right) = Y\left(\hat{\mathbf{s}}_{\mathbf{r}} \times \mathbf{E_{inc}}\right) \quad . \tag{7.2}$$

Here, $\hat{\mathbf{s}}_{\mathbf{ip}}$ is the unit vector representing the incident GO field direction on the main reflector surface. As, the incident GO field direction on the main reflector surface is the same as the reflected GO field direction from the subreflector, $\hat{\mathbf{s}}_{\mathbf{ip}}$ is the same as $\hat{\mathbf{s}}_{\mathbf{r}}$ (the unit vector representing the subreflector reflected field direction). *Y* is the characteristic admittance of the medium, which is the inverse of the characteristic impedance, η. It can be expressed as:

$$Y = \frac{1}{\eta} = \sqrt{\frac{\mu}{\varepsilon}} \quad . \tag{7.3}$$

Here, μ and ε are the permittivity and permeability of the medium respectively. In this thesis, the medium is taken to be air.

The incident field on the main reflector is the same as the scattered field from the subreflector. So,

$$\mathbf{E_{inc}} = \mathbf{E_s} \quad . \tag{7.4}$$

Using (7.1) – (7.4), the PO surface current density on the main reflector surface can be calculated. The magnitude of the PO surface currents for the shaped and unshaped dual reflector geometries are shown in Fig. 7.1. Contour plots are used to superimpose the PO currents on the surface geometry. The Cassegrain geometries are shown on the left column and the Gregorian geometries are shown on the right column. The color scales of the shaped and unshaped geometries are kept same for comparison. It can be observed that the PO currents become more uniform for the shaped geometries compared to the unshaped geometry. The currents are symmetric due to the geometry.

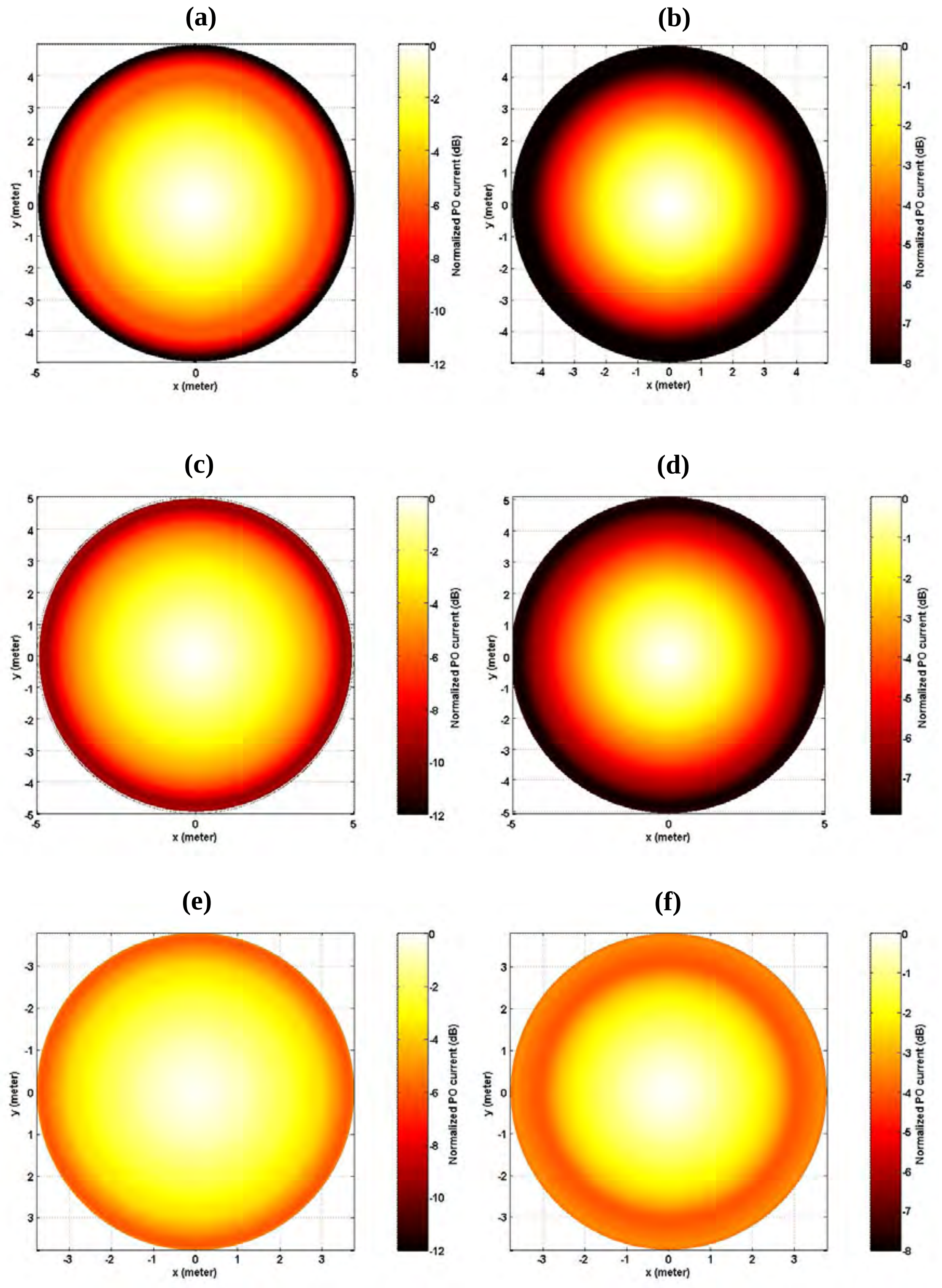

Fig. 7.1: PO surface current density on the main reflector for (a) unshaped Cassegrain geometry, (b) unshaped Gregorian geometry, (c) shaped Cassegrain geometry (opt. 1), (d) shaped Gregorian geometry (opt. 1), (e) shaped Cassegrain geometry (opt. 2) and (f) shaped Gregorian geometry (opt. 2).

7.3 Radiated Field Formulation

The radiated field from the main reflector can be formulated from the PO surface current density. The radiated field can be approximated from the vector magnetic potential **A**. The quantity is related to the PO surface currents through the following equation [4]:

$$\mathbf{A} = \iint_{S_m} \left\{ \frac{\mathbf{J_{po}} \exp(-jkR)}{R} \right\} dS_m \quad . \tag{7.5}$$

Here, R is the distance from a point on the main reflector surface to the observation point. The distance along with vectors required to calculate $\mathbf{J_{PO}}$ is shown in Fig. 7.2.

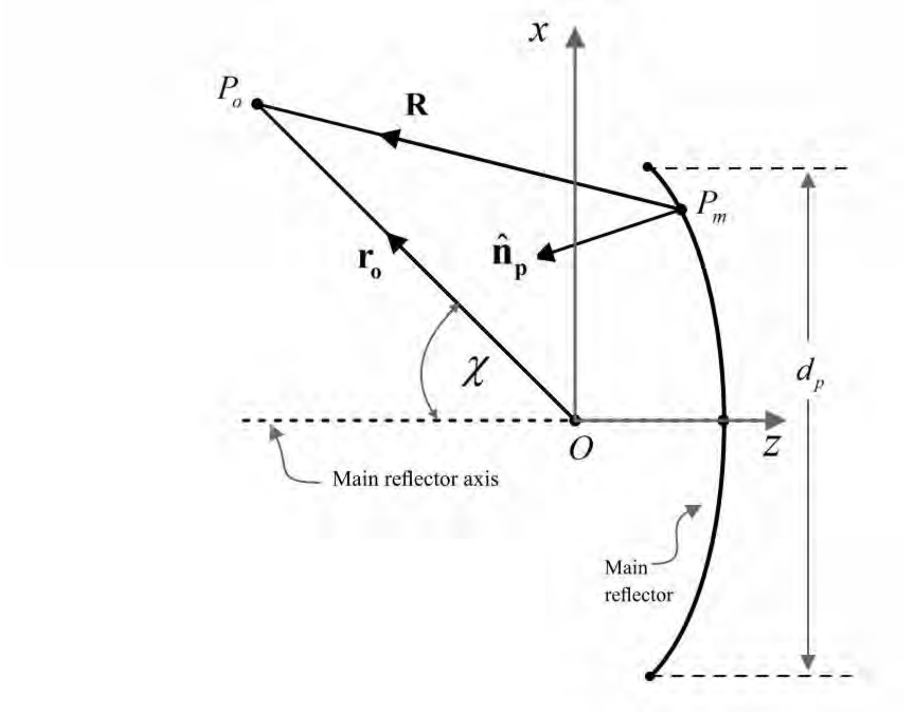

Fig. 7.2: Formulation of the main reflector radiated field.

Here, P_m is a point on the main reflector surface, P_o is the observation point in space and χ is the angle measured from the main reflector axis (–z axis) to the observation point. The radiation field from the main reflector is related to **A** as:

$$\mathbf{E_{rad}} = -j2\pi f \mu \mathbf{A} \quad . \tag{7.6}$$

Substituting **A** from (7.5) into (7.6):

$$\mathbf{E_{rad}} = -j2\pi f \mu \iint_{S_m} \left\{ \frac{\mathbf{J_{po}} \exp(-jkR)}{R} \right\} dS_m \quad . \tag{7.7}$$

The integration in (7.7) is performed over the entire surface of the main reflector, S_m. But the integration is dependent on R. So, every time R is changed, the integration must be repeated. This implies that the integration must be performed for every observation point.

The surface integration in (7.7) can be transformed using parameters ρ_m and ϕ_m. The parameters are shown in Fig. 7.3.

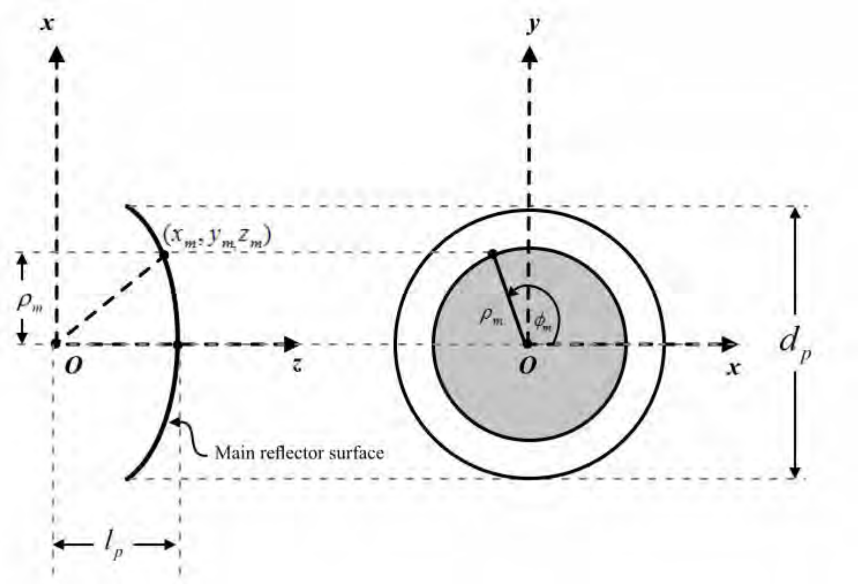

Fig. 7.3: Parameterization of the main reflector surface.

The parameters are related to the co-ordinates of the point on the main reflector surface (x_m, y_m, z_m). The relations can be easily seen from Fig. 7.3 as:

$$\left.\begin{aligned} x_m &= \rho_m \cos\phi_m \\ y_m &= \rho_m \sin\phi_m \end{aligned}\right\} . \tag{7.8}$$

The shaped main reflector varies very little from the unshaped main reflector (as shown in Section 3.7). So, it can be approximated as a paraboloid without any significant error. Therefore, the surface equation of the main reflector is:

$$z_m = -\frac{x_m^2 + y_m^2}{4 f_p} + l_p = -\frac{\rho_m^2}{4 f_p} + l_p \ . \tag{7.9}$$

In differential geometry form:

$$\mathbf{r} = \rho_m \cos\phi_m \,\hat{\mathbf{x}} + \rho_m \sin\phi_m \,\hat{\mathbf{y}} + \left(-\frac{\rho_m^2}{4 f_p} + l_p \right) \hat{\mathbf{z}} \ . \tag{7.10}$$

The differential surface area can be computed from [25]:

$$dS_m = \left| \frac{\partial \mathbf{r}}{\partial \rho_m} \times \frac{\partial \mathbf{r}}{\partial \phi_m} \right| \, d\rho_m \, d\phi_m \quad . \tag{7.11}$$

The partial derivatives can be easily calculated to give:

$$dS_m = \rho_m \sqrt{1 + \left(\frac{\rho_m}{2 f_p} \right)^2} \, d\rho_m \, d\phi_m \quad . \tag{7.12}$$

Substituting (7.12) in (7.7):

$$\mathbf{E_{rad}} = -j\omega\mu \int_{\rho_m=0}^{d_p/2} \int_{\phi_m=0}^{2\pi} \left\{ \frac{\mathbf{J_{po}} \exp(-jkR)}{R} \right\} \rho_m \sqrt{1 + \left(\frac{\rho_m}{2 f_p} \right)^2} \, d\rho_m \, d\phi_m \; . \tag{7.13}$$

The limits of the integrations in (7.13) are selected so that the integrations cover the entire main reflector surface. The main reflector radiated field can be calculated from (7.13) along with the derived equations in this section.

7.4 Conclusion

In this chapter, the field radiated from the main reflector is formulated using PO method. The PO surface currents on the main reflector surface are calculated using the value of the magnetic field incident on the main reflector surface due to scattering from the subreflector. The distribution of the PO currents on the reflector surface is shown graphically. The PO radiation integral is formulated which can be used to find the radiated field. Numerical results of the radiated fields are given in Chapter 8.

CHAPTER 8

RESULTS AND DISCUSSION

8.1 Introduction

The overall performance of a reflector antenna system is determined from its far-field radiation characteristics. The field radiated by the main reflector has been formulated in Chapter 7. Using the equations presented in Chapter 7, the far-field characteristics of the dual reflector antennas can be numerically evaluated. In this chapter, numerical results of the far-field pattern of the unshaped and shaped dual reflector antennas are provided. Performance parameters related to the far-field radiation characteristics are defined and evaluated. The chapter concludes with the performance comparison of the unshaped and shaped dual reflector antennas.

8.2 Numerical Results for the Far-field Region

The far-field radiation pattern of the unshaped and shaped dual reflector geometries are calculated using PO method. The operating frequency is assumed to be 14 GHz for all cases. The observation region is selected 2000 m away from the main reflector axis to make sure that it falls within far-field region. It has been checked that moderate variation of the observation distance does not affect the radiation pattern. This is a characteristic of far-field region. The far-fields of the Cassegrain and Gregorian geometries are discussed in the following sections.

8.2.1 Far-field of the Cassegrain geometries

The far-field radiation pattern of the unshaped Cassegrain geometry is shown in Fig. 8.1. The observation region is limited to 15° from the main reflector axis. Power levels for larger observation angle are negligible. The zoomed in view of the main lobe region is shown in Fig. 8.2. The far-field radiation pattern of the shaped Cassegrain geometry found from optimization 1, is shown in Fig. 8.3. The zoomed in view of the main lobe region is shown in Fig. 8.4. Similarly, the far-field pattern and the zoomed in view of the main lobe region of the shaped Cassegrain geometry found from optimization 2 are shown in Fig. 8.5 and 8.6 respectively.

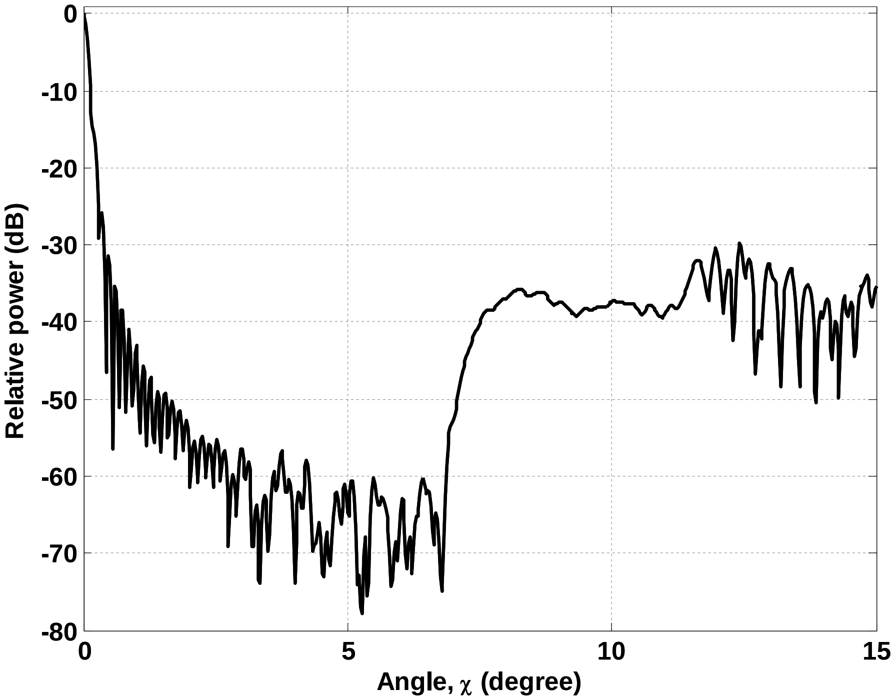

Fig. 8.1: Far-field radiation pattern of the unshaped Cassegrain geometry.

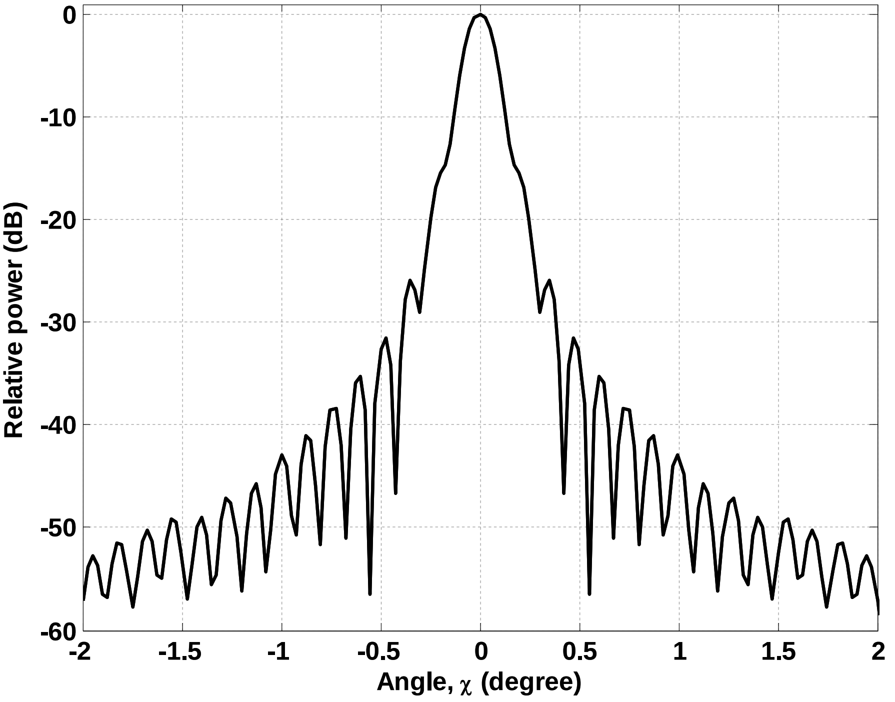

Fig. 8.2: Zoomed in view of the main lobe region of the radiation pattern of the unshaped Cassegrain geometry.

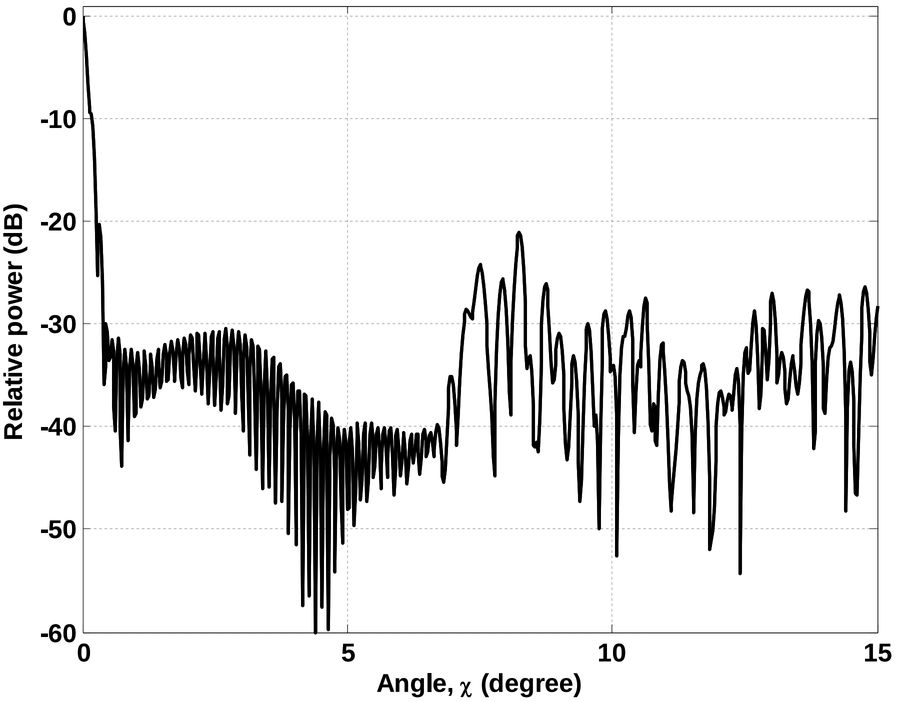

Fig. 8.3: Far-field radiation pattern of the shaped Cassegrain geometry obtained from optimization 1.

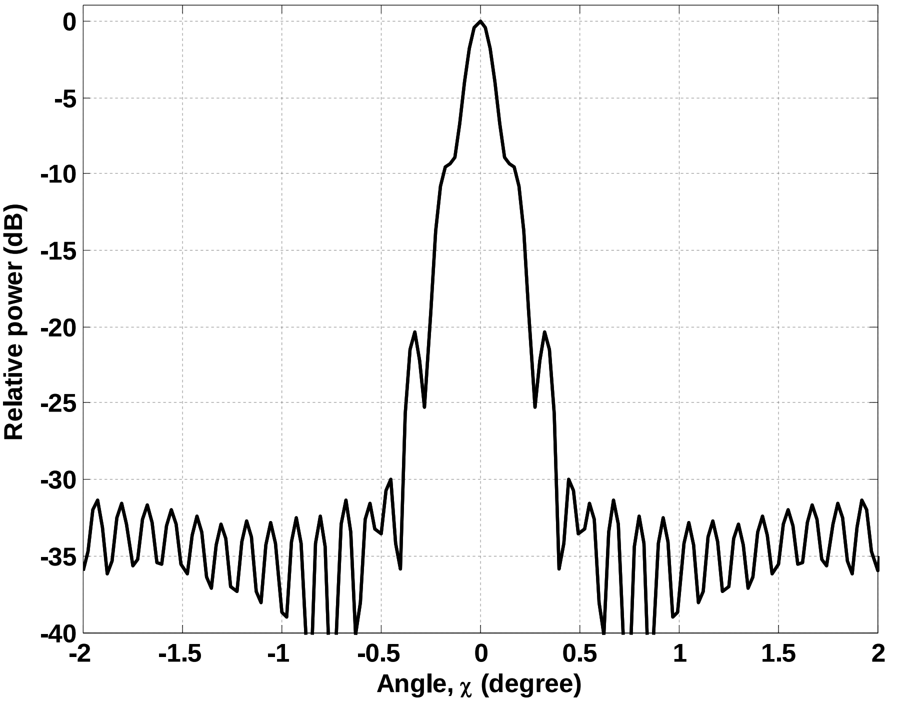

Fig. 8.4: Zoomed in view of the main lobe region of the radiation pattern of the shaped Cassegrain geometry obtained from optimization 1.

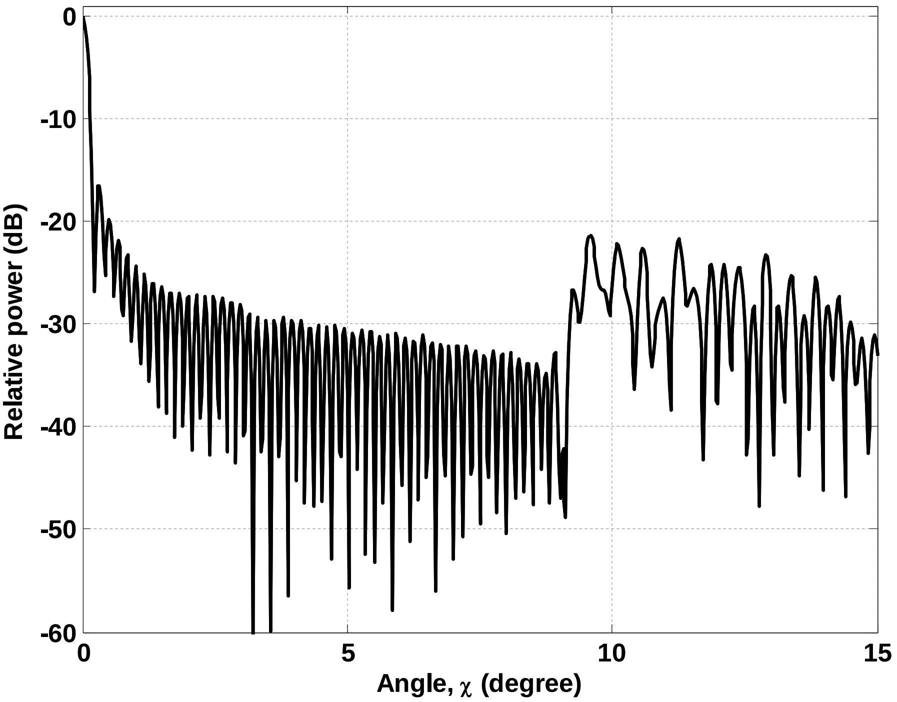

Fig. 8.5: Far-field radiation pattern of the shaped Cassegrain geometry obtained from optimization 2.

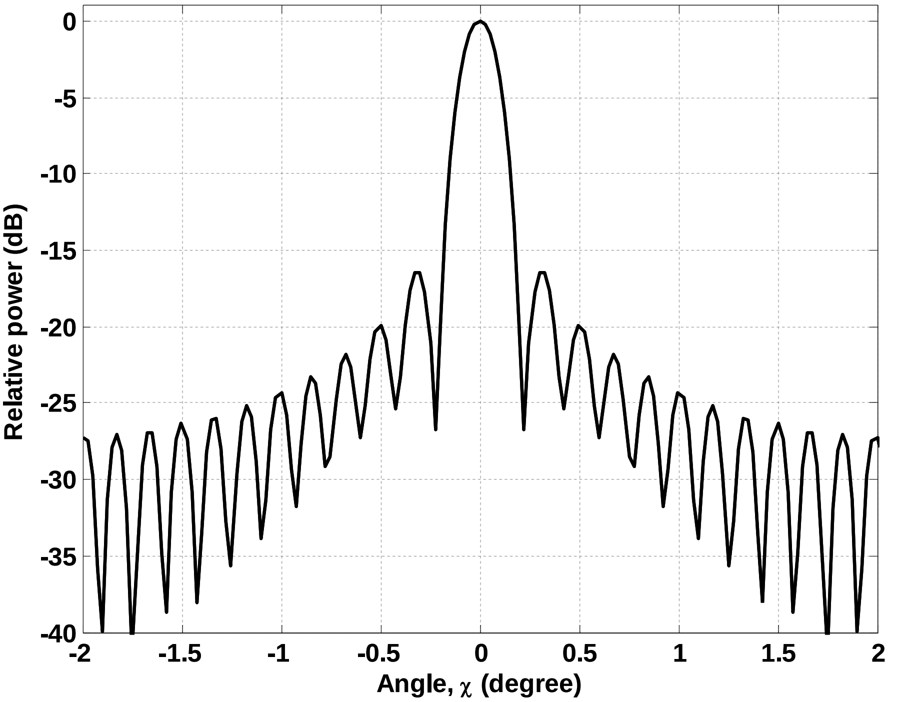

Fig. 8.6: Zoomed in view of the main lobe region of the radiation pattern of the shaped Cassegrain geometry obtained from optimization 2.

8.2.2 Far-field of the Gregorian geometries

The far-field radiation pattern of the unshaped Gregorian geometry is shown in Fig. 8.10. The zoomed in view of the main lobe region is shown in Fig. 8.11.

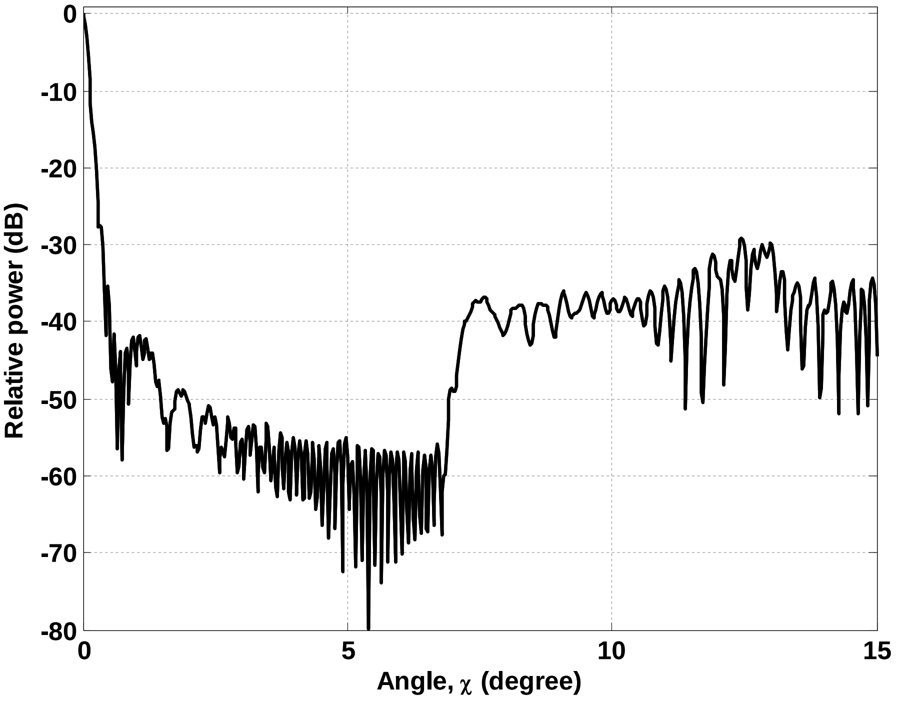

Fig. 8.7: Far-field radiation pattern of the unshaped Gregorian geometry.

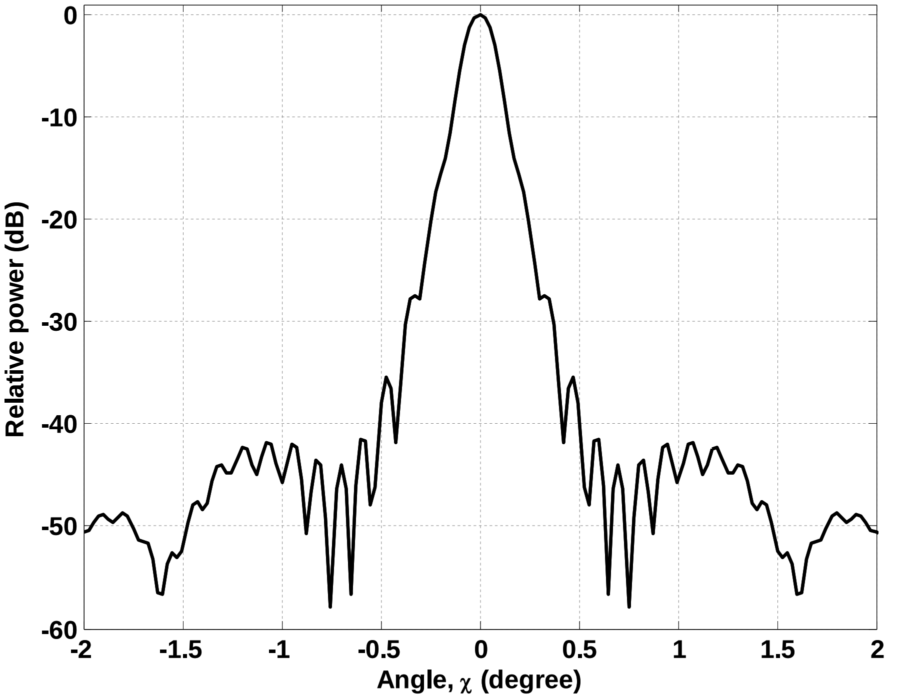

Fig. 8.8: Zoomed in view of the main lobe region of the radiation pattern of the unshaped Gregorian geometry.

The far-field radiation pattern of the shaped Gregorian geometry found from optimization 1 and optimization 2 and their corresponding zoomed in views are shown in Fig. 8.9, Fig. 8.10, Fig. 8.11 and Fig. 8.12 respectively.

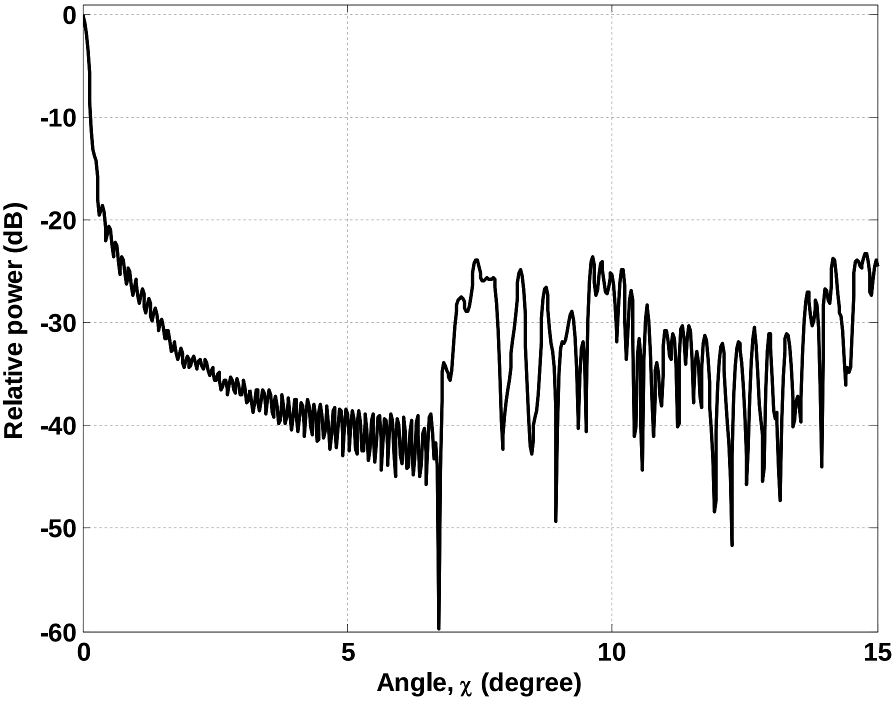

Fig. 8.9: Far-field radiation pattern of the shaped Gregorian geometry obtained from optimization 1.

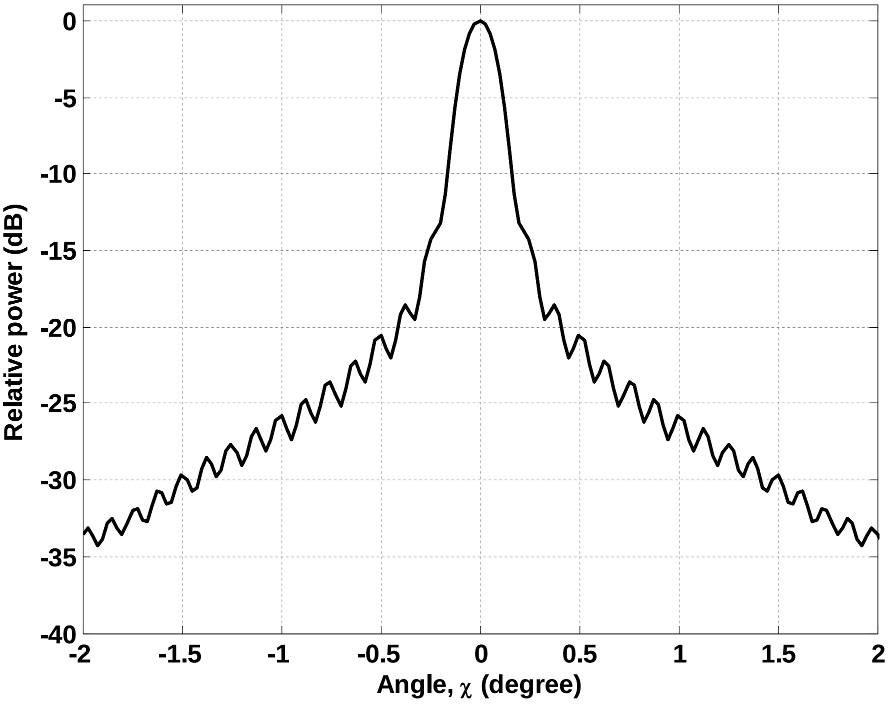

Fig. 8.10: Zoomed in view of the main lobe region of the radiation pattern of the shaped Gregorian geometry obtained from optimization 1.

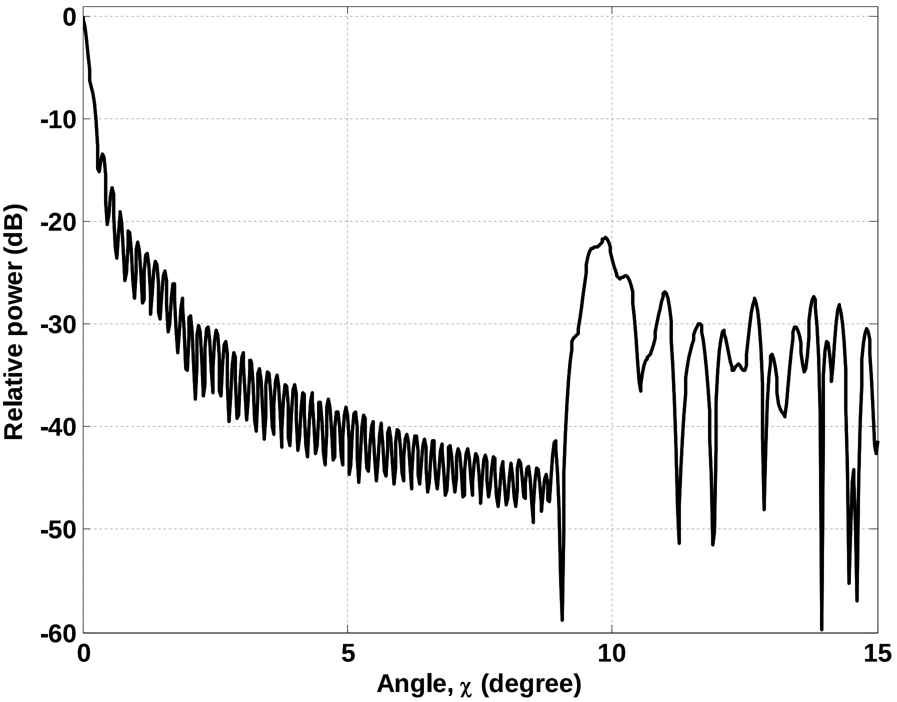

Fig. 8.11: Far-field radiation pattern of the shaped Gregorian geometry obtained from optimization 2.

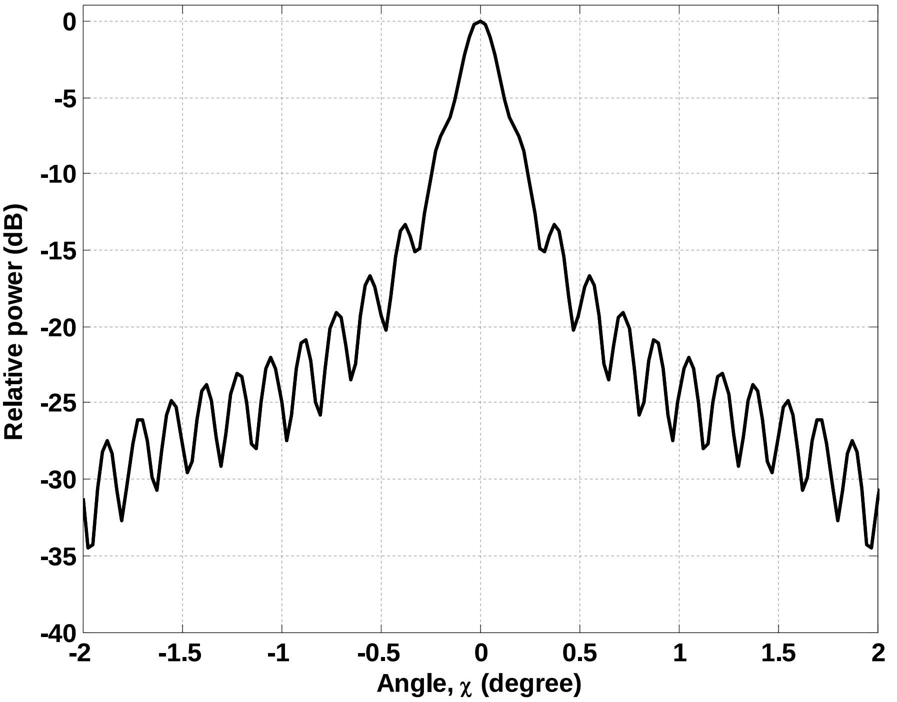

Fig. 8.12: Zoomed in view of the main lobe region of the radiation pattern of the shaped Gregorian geometry obtained from optimization 2.

8.3 Far-field Performance Evaluation

The far-field radiation pattern of the unshaped and shaped dual reflector geometries have been shown in Section 8.2. To evaluate the far-field performance of the antennas, some performance parameters must be defined. The performance of the shaped and unshaped geometries can be compared using these performance parameters.

8.3.1 Defining performance parameters

The objective of the optimizations performed in Chapter 6 was to provide uniform illuminated over the main reflector aperture. This was expected to create far-field radiation pattern with smaller beamwidth [3]. A larger the diameter of the main reflector results in a smaller beamwidth [3]. The optimizations performed concentrated on creating uniform illumination, which also can reduce beamwidth without increasing antenna size. A narrow beamwidth is necessary for satellite communications to avoid interference with neighboring satellites [1]. It is also necessary for deep space communication because a narrow beamwidth implies power is not wasted on unwanted directions [1]. Even a small angular covers a large area when the distance is large. For these reasons, beamwidth is one of the most important performance parameters. The half power beamwidth (*HPBW*) is defined as the angular region where half of total radiated power is concentrated.

Another important parameter is the *gain* or *directivity* of the antenna. Usually a smaller beamwidth implies a larger directivity. However, sidelobe levels also affect the directivity value. An antenna with smaller beamwidth may have a smaller gain compared to an antenna with larger beamwidth if the sidelobe levels are significantly larger. Usually, reducing beamwidth increases sidelobe levels. Therefore, antenna directivity does not change too much for a fixed antenna size. The maximum directivity, D_o, is defined as [21]:

$$D_o = 4\pi \frac{F_{rad}(\theta,\phi)\big|_{\max}}{\int_{\phi=0}^{2\pi}\int_{\theta=0}^{\pi} F_{rad}(\theta,\phi)\sin\theta\, d\theta\, d\phi} \; . \tag{8.1}$$

Here, $F_{rad}(\theta,\phi)$ is the radiation intensity and (θ,ϕ) are the spherical co-ordinates of the observation region. $F_{rad}(\theta,\phi)$ can be found from taking the magnitude of $\mathbf{E_{rad}}$ defined in (7.13). So,

$$F_{rad} = \left|\mathbf{E_{rad}}\right| \; . \tag{8.2}$$

Another performance parameter is the blockage efficiency, η_{block}. It is related to the area of the main reflector aperture that is blocked by some geometric structures of the antenna. The maximum blockage is created by the subreflector. The blockage due to feed and supporting mechanical structures are negligible. Assuming blockage created by the subreflector only, the blockage efficiency is defined as:

$$\eta_{block} = \left\{1 - \left(\frac{\text{Area of the subreflector}}{\text{Area of the main reflector}}\right)\right\}^2 = \left\{1 - \left(\frac{d_s}{d_p}\right)^2\right\}^2 \; . \tag{8.3}$$

Blockage efficiency should be kept high to increase effective area.

The performance parameters defined in this section can be used to compare the performance of the unshaped and shaped geometries.

8.3.2 Far-field performance comparison of the unshaped and shaped reflectors

The performance parameters of the unshaped Cassegrain geometry and the shaped Cassegrain geometries are shown in Table 8.1. The illumination efficiency, main reflector diameter and the subreflector diameter data are repeated from Table 6.1 for convenience.

Table 8.1: Far-field performance comparison of the Cassegrain geometries.

Parameters	Cassegrain geometry		
	Unshaped	Opt. 1	Opt. 2
d_p	10 m	10 m	7.5 m
d_s	1.25 m	1.7 m	1.25 m
$HPBW$	0.1436°	0.1278°	0.1800°
D_o	61.92 dB	58.94 dB	56.03 dB
η_{block}	96.9 %	94.3 %	94.5 %
η_{ill}	85.87 %	87.92 %	92.82 %

It can be observed from Table 8.1 that the shaped Cassegrain reflectors obtained from optimization 1, outperforms unshaped reflectors in terms of beamwidth. However, around 3 dB gain drop is also observed. This is dues to the increased sidelobe levels of shaped reflectors compared to the unshaped reflectors as seen in Fig. 8.1 and Fig. 8.3. It is also evident that the shaped antenna obtained from optimization 2 has beamwidth comparable to the unshaped antenna, even though it has a smaller main reflector.

The performance parameters of the unshaped Cassegrain geometry and the shaped Gregorian geometries are shown in Table 8.2. The illumination efficiency, main reflector diameter and the subreflector diameter data are repeated from Table 6.2 for convenience.

Table 8.2: Far-field performance comparison of the Gregorian geometries.

Parameters	Gregorian geometry		
	Unshaped	Opt. 1	Opt. 2
d_p	10 m	10 m	7.5 m
d_s	0.78 m	0.98 m	0.78 m
$HPBW$	0.1492°	0.1460°	0.1770°
D_o	61.66 dB	57.31 dB	55.12 dB
η_{block}	98.8 %	98.1 %	97.8 %
η_{ill}	85.68 %	90.44 %	97.37 %

It can be observed from Table 8.2 that, the shaped Gregorian antenna obtained from optimization 1 has a smaller half power beamwidth. The slight decrease in directivity is due to the increase sidelobe levels as can be seen by comparing Fig. 8.7 and Fig. 8.9. The shaped antenna with the smaller aperture are obtained from optimization 2, has beamwidth comparable to the unshaped antenna.

The obtained values are comparable with experimental and numerical values reported in literature [1], [2]. So, the results can be considered accurate. It can be concluded that the shaped reflectors have satisfactory far-field performance.

8.4 Summary

In this chapter, the radiated fields of the unshaped and shaped dual reflector antennas have been computed using PO method. Performance parameters have been defined to quantify the performance of the shaped and unshaped reflectors. It has been found that the shaped reflectors satisfy the design criterions. The shaped reflectors outperform the unshaped reflectors in terms of beamwidth. It has been shown that an optimized shaped dual reflector antenna with a smaller sized main reflector can have beamwidth comparable to a larger unshaped reflector. This implies that main reflector size reduction is possible without increasing beamwidth or decreasing antenna directivity significantly.

CHAPTER 9
CONCLUSION

9.1 Summary

The work presented in this thesis concentrates on the design of circularly symmetric shaped dual reflector antennas. The design procedure consists of a proposed method of defining shaped dual reflector surfaces and an optimization algorithm that determines the optimum shaped surfaces. The proposed method uses a small number of parameters to describe the shaped surfaces. It has been shown that, only four parameters are required to accurately describe practical shaped surfaces. So, only four parameters need to be optimized to find an optimum shaped surface. This number is less than the number of parameters required to represent a shaped surface using other methods found in literature. Due to small number of parameters that need to be optimized by the optimization algorithm, the computation complexities are significantly reduced. Differential evolution algorithm is selected to as the optimization algorithm for its fast convergence characteristics. Two separate sets of optimizations have been performed for each of the dual reflector geometries (Cassegrain and Gregorian). The design goal for the first optimization is to decrease beamwidth without changing antenna size. The design goal of the second optimization is to reduce the antenna size while keeping the beamwidth small. These can be implemented by creating a uniform illumination over the main reflector aperture. So, the objective of the optimization procedure is taken to be uniform illumination of the main reflector surface without significantly increasing spillover losses. The design requirements are integrated into the optimization algorithm through the definition of the cost function. The optimization requires evaluation of the radiation characteristics of the shaped dual reflectors. So, field analysis is inherent in the design procedure. Fields from the feed antenna, the subreflector and the main reflector must be analyzed separately. A corrugated horn is designed as the feed antenna. The geometry of the dual reflectors is taken into account when designing the horn. The fields of the horn are calculated using standard equations. UTD method is used for analysis of the field scattered from the subreflector on to the main reflector. The optimization algorithm checks the uniformity of the scattered field from the subreflector and optimizes the shape of the subreflector to create maximum uniformity without increasing the spillover losses significantly. The main reflector surface is synthesized based on the shape of the subreflector surface. The field radiated from the main reflector is calculated using PO method. The beamwidth is computed for the shaped and unshaped dual reflectors from corresponding far-field patterns. It has been found that the beamwidth requirements have been satisfied for the optimized shaped reflectors. Other performance characteristics of the designed shaped dual reflectors are also within satisfactory limits. The obtained values are found to be in agreement with numerical and experimental values reported in literature. Thus the obtained results can be considered accurate.

9.2 Scope for Future Work

The presented work gives satisfactory results. But it has some limitations. Only the design procedures of shaped circularly symmetric dual reflectors have been presented in this thesis. The analysis of single reflector antennas has not been presented. But the design method can be used for single shaped reflector antennas that are circularly symmetric. However, the proposed method can not be used to synthesize shaped offset single reflector or shaped offset dual reflector antennas. The method also fails if the subreflector or the main reflector has non circular cross sectional area. The method is limited to only circularly symmetric cases. This limitation arises due to the definition of the distortion function that determines the shape of the subreflector. The defined distortion function is inherently circularly symmetric. A more general expression of the shaped surfaces is necessary to design reflectors of offset geometries and un-symmetric shapes.

The accuracy of the proposed design method depends on the accuracy of the numerical methods used. The UTD and PO analysis is accurate for electrically large reflectors only. The design method can be made suitable for electrically small reflectors by applying different numerical methods that are accurate for small structure analysis.

REFERENCES

[1] Volakis, J. L. (Ed.), “Antenna Engineering Handbook,” 4th edition, McGraw-Hill, 2007.

[2] Balanis, C. A., (Ed.), “Modern Antenna Handbook,” John-Wiley & Sons, 2008.

[3] Baars, J. W. M., “The Paraboloidal Reflector Antenna in Radio Astronomy and Communications: Theory and Practice,” Springer, 2007.

[4] Stutzman, W. L., Thiele, G. A., “Antenna Theory and Design,” John-Wiley & Sons, 1981.

[5] Silver, S. (Ed.), “Microwave Antenna Theory and Design”, 1st edition, McGraw-Hill, New York, 1949.

[6] Galindo, V., "Design of dual-reflector antennas with arbitrary phase and amplitude distributions," *IEEE Transactions on Antennas and Propagation*, vol. 12, pp. 403-408, 1964.

[7] Kim, Y., and Lee, T.H., "Shaped Circularly Symmetric Dual Reflector Antennas by Combining Local Conventional Dual Reflector Systems," *IEEE Transactions on Antennas and Propagation*, vol. 57, no. 1, pp. 47-56, 2009.

[8] Moreira, F. J. S., and Bergmann, J. R., "Shaping Axis-Symmetric Dual-Reflector Antennas by Combining Conic Sections," *IEEE Transactions on Antennas and Propagation*, vol. 59, no. 7, pp. 1042-1046, 2011.

[9] Xu, S., Rahmat-Samii, Y., and Gies, D., "Shaped-Reflector Antenna Designs Using Particle Swarm Optimization: An Example of a Direct-Broadcast Satellite Antenna," *Microwave and Optical Technology Letters*, vol. 48, pp. 1341-1347, 2006.

[10] Duan, D. W., and Rahmat-Samii, Y., "A Generalized Diffraction Synthesis Technique for High Performance Reflector Antennas," *IEEE Transactions on Antennas and Propagation*, vol. 43, no. 1, pp. 27-40, 1995.

[11] Narasimhan, M. S., Ramanujam, P., and Raghavan, K., "GTD Analysis of the Radiation Patterns of a Shaped Subreflector," *IEEE Transactions on Antennas and Propagation*, vol. 29, no. 5, pp. 792-795, 1981.

[12] Lee, C. S., "A Simple Method of Dual-Reflector Geometrical Optics Synthesis," *Microwave and Optical Technology Letters*, vol. 1, no. 10, pp. 367-371, 1988.

[13] Rahmat-Samii, Y., and Mumford, J., "Reflector Diffraction Synthesis Using Global Coefficients Optimization Techniques," in Antennas and Propagation Society International Symposium, vol. 3, 1989, pp. 1166-1169.

[14] Rahmat-Samii, Y., and Galindo-Israel, V., “Shaped Reflector Antenna Analysis using the Jacob-Bessel Series,” vol. 28, no. 4, pp. 425-435, 1980.

[15] Storn, R., and Price, K., "Differential Evolution - A Simple and Efficient Heuristic for Global Optimization over Continuous Spaces," *Journal of Global Optimization*, vol. 11, pp. 341-359, 1997.

[16] McNamara, D. A., Pistorius, C. W. I., Malherbe, J. A. G., “Introduction to the Uniform Geometrical Theory of Diffraction,”

[17] Lim, K., Ryu, H., Lee, S., and Choi, J., "UTD Analysis of a Shaped Subreflector in a Dual Offset-Reflector Antenna System," *IEEE Transactions on Antennas and Propagation*, vol. 46, no. 10, pp. 1555-1559, 1998.

[18] Pathak, P. H., "High frequency techniques for antenna analysis," *Proceedings of the IEEE*, vol. 80, no. 1, pp. 44-65, 1992.

[19] Hofered, R. A., and Rahmat-Samii, Y., “Subreflector Shaping for Antenna Distortion Compensation: An Efficient Fourier-Jacobi Expansion With GO/PO Analysis,” *IEEE Transaction on Antennas and Propagation*, vol. 50, no. 12, pp. 1676-1687, 2002.

[20] Polyanin, A. D., Manzhirov, A. V., “Handbook of Mathematics for Engineers and Scientists,” Chapman & Hall/CRC, Taylor & Francis Group, 2007.

[21] Balanis, C. A., “Antenna Theory Analysis and Design,” 3rd edition, Wiley & Sons, 2005.

[22] Granet, C. "Designing Axially Symmetric Cassegrain or Gregorian Dual-Reflector Antennas from Combinations of Prescribed Geometric Parameters," *IEEE Antennas and Propagation Magazine*, vol. 40, no. 2, pp. 76-82, 1998.

[23] Bergmann, J. R., and Hasselmann, F. J. V., "Interpolation of Reflector Surfaces by Pseudosplines," *IEE Proceedings on Microwaves, Antennas and Propagation*, vol. 144, no. 1, pp. 42-46, 1997.

[24] O’Niell, B., “Elementary Differential Geometry,” 2nd edition, Academic Press, Elsevier, 2006.

[25] Widder, D. V., “Advanced Calculus,” 2nd edition, Prentice-Hall, New Delhi, 2004.

[26] Jung, Y. B., and Park, S. O., "Ka-Band Shaped Reflector Hybrid Antenna Illuminated by Microstrip-Fed Horn Array," *IEEE Transactions on Antennas and Propagation*, vol. 56, no. 12, pp. 3863-3867, 2008.

[27] Ludwig, A. C., “The Definition of Cross Polarization,” *IEEE Transactions on Antennas and Propagation*, vol. 21, no. 1, pp. 116-119, 1973.

[28] Rusch, W. V. T., and Sorense, O., “The Geometrical Theory of Diffraction for Axially Symmetric Reflectors,” *IEEE Transactions on Antennas and Propagation*, vol. 23, no. 3, pp. 414-419, 1975.

[29] Price, K. V., Storn, R. M., and Lampinen, J. A. “Differential Evolution: A Practical Approach to Global Optimization,” Springer, 2005.

[30] Qing, A., Lee, C. K., “Differential Evolution in Electromagnetics,” Springer, 2010.